A general algorithm for the linear and quadratic gradients of physical quantities based on 10 or more point measurements

Chao Shen[1], Yufei Zhou[2], Yonghui Ma[3], Xiaogang Wang[4], Zuyin Pu[5], and Malcolm W Dunlop[6]

[1]School of Science
[2]School of Science, Harbin Institute of Technology
[3]Harbin Institute of Technology, Shenzhen
[4]Department of Physics, and Laboratory for Space Environment and Physical Sciences, Harbin Institute of Technology
[5]Peking University
[6]Beihang University

November 24, 2022

Abstract

In this study, a novel algorithm for jointly estimating the linear and quadratic gradients of physical quantities with multiple spacecraft observations based on the least square method has been put forward for the first time. With 10 or more spacecraft constellation measurements as the input, this new algorithm can yield both the linear and quadratic gradients at the barycenter of the constellation. Iterations have been used in the algorithm. The tests on cylindrical flux ropes, dipole magnetic field and modeled geo-magnetospheric field have been carried out. The tests indicate that the linear gradient gained has the second order accuracy, while the quadratic gradient is of the first order accuracy. The test on the modeled geo-magnetospheric field shows that, the more the number of the spacecraft in the constellation, the high the accuracy of the quadratic gradient calculated. However, the accuracy of the linear gradient yielded is independent of the number of the spacecraft. The feasibility, reliability and accuracy of this algorithm have been verified successfully. This algorithm can find wide applications in the design of the future multiple S/C missions as well as in the analysis of multiple point measurement data.

Hosted file

`supplementary information-2.docx` available at https://authorea.com/users/524929/articles/604971-a-general-algorithm-for-the-linear-and-quadratic-gradients-of-physical-quantities-based-on-10-or-more-point-measurements

Hosted file

`supplementary information-1.docx` available at https://authorea.com/users/524929/articles/604971-a-general-algorithm-for-the-linear-and-quadratic-gradients-of-physical-quantities-based-on-10-or-more-point-measurements

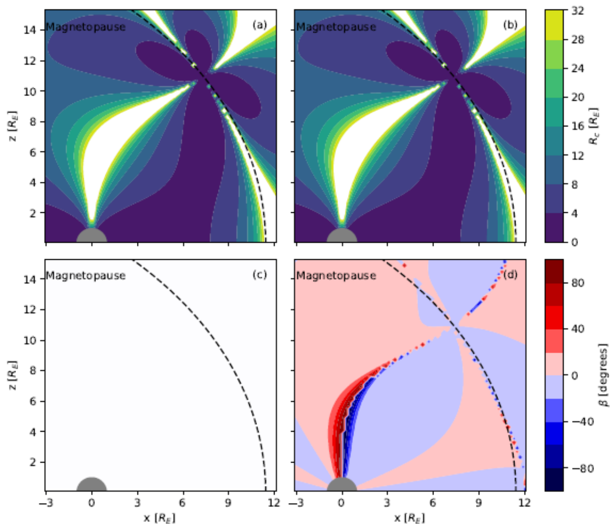

Figure 12: Distributions of the radius of curvature (top) and helix angle (bottom) of MFLs in the coordinate plane y=0 in modeled magnetosphere based on theoretical (left) and new algorithm (right) calculations. The dashed line indicates the magnetopause when $B_z = 27nT, D_p = 3nPa$ [Shue et al., 1998].

A general algorithm for the linear and quadratic gradients of physical quantities based on 10 or more point measurements

Chao Shen[1], Yufei Zhou[1], Yonghui Ma[1], Xiaogang Wang[2], Zuyin Pu[3], M. Dunlop[4, 5]

[1]School of Science, Harbin Institute of Technology, Shenzhen, 518055, China

[2]School of Physics, Harbin Institute of Technology, Harbin, 150001, China

[3]School of Earth and Space Sciences, Peking University, Beijing, China

[4]School of Space and Environment, Beihang University, Beijing, China

[5]Rutherford Appleton Laboratory, Chilton, DIDCOT, Oxfordshire OX11 0QX, United Kingdom

Key Points:

A general algorithm for the linear and quadratic gradients based on 10 or more spacecraft measurements is presented for the first time

The characteristic matrix of the constellation affecting the determination of the quadratic gradient has been found and its features shown

The algorithm has been tested on the magnetic field, indicating the obtained linear magnetic gradient is of second order accuracy

Abstract

In this study, a novel algorithm for jointly estimating the linear and quadratic gradients of physical quantities with multiple spacecraft observations based on the least square method has been put forward for the first time. With 10 or more spacecraft constellation measurements as the input, this new algorithm can yield both the linear and quadratic gradients at the barycenter of the constellation. Iterations have been used in the algorithm. The tests on cylindrical flux ropes, dipole magnetic field and modeled geo-magnetospheric field have been carried out. The tests indicate that the linear gradient gained has the second order accuracy, while the quadratic gradient is of the first order accuracy. The test on the modeled geo-magnetospheric field shows that, the more the number of the spacecraft in the constellation, the high the accuracy of the quadratic gradient calculated. However, the accuracy of the linear gradient yielded is independent of the number of the spacecraft. The feasibility, reliability and accuracy of this algorithm have been verified successfully. This algorithm can find wide applications in the design of the future multiple S/C missions as well as in the analysis of multiple point measurement data.

Plain Language Summary

With the development of space explorations, the constellations with 10 or more spacecraft may become true in the near future. However, there is still no general algorithm available for calculating the quadratic gradient of various physical quantities with 10 or more point measurements. In this article, we present a universal approach that can estimate both the linear and quadratic gradients of physical quantities based on 10 or more point measurements. This algorithm has been tested and its reliability has been verified. The tests show that the linear gradient obtained is of the second order accuracy, while the quadratic gradient the first order accuracy. This algorithm developed will be beneficial for the design of the future multiple S/C constellation missions and have wide applications in analyzing multiple point measurement data.

Key Words:

Multiple Spacecraft Measurements, Iteration, Linear gradient, Quadratic Gradient, Geometry of Magnetic Field Lines

1. Introduction

The gradients of physical quantities play important roles in the dynamic evolution of space plasmas. For example, the first-order gradient of electromagnetic fields balance their temporal variations as well as the sources (charge density and current density); the linear gradient of physical quantities (magnetic field, thermal pressure, etc.) can also drive the drift motions of the charged particles in electromagnetic fields. The linear gradient of physical quantities can be estimated from the 4 points in situ measurements with a first-order accuracy, and a lot of estimators have been developed already (Dunlop et al., 1988; Harvey, 1998; Chanteur, 1998; De Keyser, et al., 2007; Vogt et al., 2008; Vogt et al., 2009).

On the other hand, the quadratic gradient of physical quantities can lead to the diffusion and dissipation processes in plasmas. The quadratic gradients of electromagnetic potentials can balance the sources as shown by the Poisson equation. The geometry of the magnetic field depends on both the first order and the second-order magnetic gradients (Shen et al., 2020).

Recently some investigations have been made to fit the magnetic field to the second order based on the four spacecraft magnetic and current density observations (Torbert et al., 2020). Shen et al. (2020) have put forward an explicit algorithm to calculate the quadratic magnetic gradient as well as the complete geometry of magnetic field lines with 4 point magnetic field and particle/current density measurements under the constraints of electromagnetic laws. This approach, however, can not be applied to estimate the quadratic gradient of other physical fields, such as those of the density, temperature, and electric potential, etc. Generally, at least 10 point measurements of a physical quantity are required to calculate its second-order gradient (Chanteur, 1998).

With the development of space exploration, the constellation mission with 10 or more spacecraft has become possible (e.g., Cross-Scale mission). However, we still have no applicable universal algorithm for estimating the quadratic gradient of physical quantities with 10 and more point measurements.

In this paper, we present a universal algorithm that can estimate both the linear and quadratic gradients of physical quantities based on 10 or more point measurements. This algorithm has been tested and its reliability has been verified. The accuracy of this algorithm has been investigated. The algorithm is presented in the Section 2, the tests on the method have been made in Section 3, and the summary and discussions are given in Section 4.

2. Algorithm

Consider that a constellation, which is composed of $\mathrm{N} \geq 10$ spacecraft, performs in situ observations on a certain physical field f (density, magnetic field, or electric potential, etc.). In the Earth center frame of reference (or other inertial frames of the investigator), the Cartesian coordinates are (x^1, x^2, x^3) (corresponding to (x, y, z), respectively) with their bases ($\hat{\mathbf{x}}_1, \hat{\mathbf{x}}_2, \hat{\mathbf{x}}_3$). The position of the αth spacecraft is at

$x^i_{(\alpha)} = \left(x^1_{(\alpha)}, x^2_{(\alpha)}, x^3_{(\alpha)}\right)\left(\alpha = 1, 2, \cdots, N\right)$, and its velocity in the Earth center reference frame is $\mathbf{u}_{(\alpha)}$. The coordinates $x^{\mathrm{i}}_{\mathrm{c}}$ of the barycenter of the constellation satisfy

$$\sum_{\alpha=1}^{\mathrm{N}} \Delta x^{\mathrm{i}}_{(\alpha)} = \sum_{\alpha=1}^{\mathrm{N}} \left(x^{\mathrm{i}}_{(\alpha)} - x^{\mathrm{i}}_{\mathrm{c}}\right) = 0 . \tag{1}$$

So that

$$x^{\mathrm{i}}_{\mathrm{c}} = \frac{1}{\mathrm{N}} \sum_{\alpha=1}^{\mathrm{N}} x^{\mathrm{i}}_{(\alpha)} . \tag{2}$$

The physical quantity observed is $f'\left(x^i_\alpha\right) = f'_{(\alpha)}$ in the spacecraft reference frame and $f\left(x^i_\alpha\right) = f_{(\alpha)}$ in the Earth center reference frame (a static frame of reference), respectively. There is a certain transformation relationship between $f'_{(\alpha)}$ and $f_{(\alpha)}$. For the magnetic field, $\mathbf{B}'_{(\alpha)} = \mathbf{B}_{(\alpha)}$. For the electric field, $\mathbf{E}'_{(\alpha)} = \mathbf{E}_{(\alpha)} + \mathbf{u}_{(\alpha)} \times \mathbf{B}_{(\alpha)}$. For the electric and magnetic potentials, $\mathbf{A}'_{(\alpha)} = \mathbf{A}_{(\alpha)}$, $\phi'_{(\alpha)} = \phi_{(\alpha)} - \mathbf{u}_{(\alpha)} \cdot \mathbf{A}_{(\alpha)}$. For the charge density and current density, $\rho'_{(\alpha)} = \rho_{(\alpha)}$ and $\mathbf{j}'_{(\alpha)} = \mathbf{j}_{(\alpha)} - \mathbf{u}_{(\alpha)}\rho_{(\alpha)}$.

In the Earth center reference frame, the linear gradient of the physical quantity f is $\frac{\partial f}{\partial x^i} = \nabla_i f$, and its quadratic gradient is $\frac{\partial^2 f}{\partial x^i \partial x^j} = \nabla_i \nabla_j f$. Based on Taylor expansion, the physical quantity observed, $f_{(\alpha)}$, can be expressed as

$$f_{(\alpha)} = f_c + \Delta x^i_{(\alpha)} \nabla_i f_c + \frac{1}{2} \Delta x^i_{(\alpha)} \Delta x^j_{(\alpha)} \nabla_i \nabla_j f_c , \tag{3}$$

where all the gradients with orders higher than 2 are neglected under the assumption that $\Delta x^{\mathrm{i}}_{(\alpha)}$ are much less than the characteristic scale of the magnetic structures investigated. So that there are 10 parameters ($f_{\mathrm{c}}, (\nabla_i f)_c, (\nabla_i \nabla_j f)_c$) to be determined. The formula (3) can also be written as

$$f_{(\alpha)} = f_{\mathrm{c}} + \Delta x^i_{(\alpha)} \mathrm{g}_i + \frac{1}{2} \Delta x^i_{(\alpha)} \Delta x^j_{(\alpha)} \mathrm{G}_{ij} , \tag{3'}$$

where, the linear and quadratic gradients of the physical quantity at the barycenter are

$g_i = (\nabla_i f)_c$ and $G_{ij} = (\nabla_i \nabla_j f)_c$, respectively. It is noted that $G_{ij} = G_{ji}$. Therefore, to obtain the 10 parameters (f_c, g_i, G_{ij}), observations by the constellation with at least 10 spacecraft are required.

In order to obtain the estimator for the 10 parameters (f_c, g_i, G_{ij}) with the desired accuracy from the $N \geq 10$ spacecraft in situ observations, we make use of the least square method (Harvey, 1998; Shen et al., 2003). Assume the action to be

$$S = \frac{1}{N}\sum_{\alpha}\left[f_c + \Delta x^i_{(\alpha)} g_i + \frac{1}{2}\Delta x^i_{(\alpha)}\Delta x^j_{(\alpha)} G_{ij} - f_{(\alpha)} \right]^2 . \tag{4}$$

Minimize it by

$$\delta S = 0 , \tag{5}$$

so as to find the formulas for f_c, $g_i = (\nabla_i f)_c$ and $G_{ij} = (\nabla_i \nabla_j f)_c$.

Equation (5) leads to

Due to

$$\begin{aligned} \frac{\partial S}{\partial f_c} &= \frac{1}{N}\sum_{\alpha=1}^{N} 2\left[f_c + \Delta x^i_{(\alpha)} g_i + \frac{1}{2}\Delta x^i_{(\alpha)}\Delta x^j_{(\alpha)} G_{ij} - f_{(\alpha)} \right] \\ &= 2\cdot\frac{1}{N}\sum_{\alpha=1}^{N}\left[f_c - f_{(\alpha)} \right] + 2\cdot\frac{1}{N}\sum_{\alpha=1}^{N}\Delta x^i_{(\alpha)} g_i + \frac{1}{N}\sum_{\alpha=1}^{N}\Delta x^i_{(\alpha)}\Delta x^j_{(\alpha)} G_{ij} = 0 \end{aligned} , \tag{7}$$

we get

$$f_c = \frac{1}{N}\sum_{\alpha} f_{(\alpha)} - \frac{1}{2N}\sum_{\alpha}^{N}\Delta x^i_{(\alpha)}\Delta x^j_{(\alpha)} G_{ij} , \tag{8}$$

where the equation (1) is used. The above equation can also be written as

$$f_c = \frac{1}{N}\sum_{\alpha} f_{(\alpha)} - \frac{1}{2} R^{ij} G_{ij} . \tag{8'}$$

Here R^{ij} is the volumetric tensor (or 3×3 matrix) (Harvey, 1998; Shen et al., 2003), which is defined as

$$R^{ij} \equiv \frac{1}{N}\sum_{\alpha=1}^{N}\Delta x_{(\alpha)}^{i}\Delta x_{(\alpha)}^{j} = \frac{1}{N}\sum_{\alpha=1}^{N}\left(x_{(\alpha)}^{i}-x_{c}^{i}\right)\left(x_{(\alpha)}^{j}-x_{c}^{j}\right). \tag{9}$$

Therefore, the physical quantity at the barycenter is the average of all the measurements plus the correction term by the quadratic gradient.

From $\partial S/\partial g_i = 0$, we get

$$\frac{\delta S}{\delta g_i} = \frac{1}{N}\sum_{\alpha=1}^{N}2\left[f_c - f_{(\alpha)} + \Delta x_{(\alpha)}^{k}g_k + \frac{1}{2}\Delta x_{(\alpha)}^{k}\Delta x_{(\alpha)}^{m}G_{km}\right]\Delta x_{(\alpha)}^{i}$$

$$= -2\cdot\frac{1}{N}\sum_{\alpha=1}^{N}f_{(\alpha)}\Delta x_{(\alpha)}^{i} + 2R^{ik}g_k + R^{ikm}G_{km} = 0, \tag{10}$$

where the 3 order tensor is defined as

$$R^{ikm} \equiv \frac{1}{N}\sum_{\alpha=1}^{N}\Delta x_{(\alpha)}^{i}\Delta x_{(\alpha)}^{k}\Delta x_{(\alpha)}^{m}. \tag{11}$$

R^{ikm} is symmetrical, i.e., $R^{ikm} = R^{kim} = R^{imk}$. Eq. (10) reduces to

$$R^{ik}g_k = \frac{1}{N}\sum_{\alpha}^{N}\left(x_{(\alpha)}^{i}-x_{c}^{i}\right)f_{\alpha} - \frac{1}{2}R^{ikm}G_{km}. \tag{12}$$

Let R^{-1} be the inverse of the volumetric tensor, which satisfies $\left(R^{-1}\right)_{ik}R^{kj} = R^{jk}\left(R^{-1}\right)_{ki} = \delta_{i}^{j}$. Hence the linear gradient at the barycenter is obtained from Eq. (12) as follows

$$g_i = \left(R^{-1}\right)_{ij}\cdot\frac{1}{N}\sum_{\alpha}^{N}\left(x_{(\alpha)}^{j}-x_{c}^{j}\right)f_{\alpha} - \frac{1}{2}\left(R^{-1}\right)_{ij}R^{jkm}G_{km}. \tag{13}$$

The second term at the right-hand side of the above formula is the correction arising from the quadratic gradient.

From $\partial S/\partial G_{ij} = 0$, we get

$$\frac{\partial \mathrm{S}}{\partial \mathrm{G}_{\mathrm{ij}}}=\frac{1}{\mathrm{N}}\sum_{\alpha=1}^{\mathrm{N}}\left[f_{\mathrm{c}}-f_{(\alpha)}+\Delta x_{(\alpha)}^{\mathrm{k}}\mathrm{g}_{\mathrm{k}}+\frac{1}{2}\Delta x_{(\alpha)}^{\mathrm{k}}\Delta x_{(\alpha)}^{\mathrm{m}}\mathrm{G}_{\mathrm{km}}\right]\Delta x_{(\alpha)}^{\mathrm{i}}\Delta x_{(\alpha)}^{\mathrm{j}}=0. \tag{14}$$

Thus

$$f_{\mathrm{c}}\mathrm{R}^{\mathrm{ij}}-\frac{1}{\mathrm{N}}\sum_{\alpha=1}^{\mathrm{N}}f_{(\alpha)}\Delta x_{(\alpha)}^{\mathrm{i}}\,\Delta x_{(\alpha)}^{\mathrm{j}}+\mathrm{R}^{\mathrm{ijk}}\mathrm{g}_{\mathrm{k}}+\frac{1}{2}\mathrm{R}^{\mathrm{ijkm}}\mathrm{G}_{\mathrm{km}}=0, \tag{15}$$

where the 4-order tensor

$$\mathrm{R}^{\mathrm{ijkm}}\equiv\frac{1}{\mathrm{N}}\sum_{\alpha=1}^{\mathrm{N}}\Delta x_{(\alpha)}^{\mathrm{i}}\Delta x_{(\alpha)}^{\mathrm{j}}\Delta x_{(\alpha)}^{\mathrm{k}}\Delta x_{(\alpha)}^{\mathrm{m}}. \tag{16}$$

Note that $\mathrm{R}^{\mathrm{ijkm}}$ is symmetric with $\mathrm{R}^{\mathrm{ijkm}}=\mathrm{R}^{\mathrm{jikm}}=\mathrm{R}^{\mathrm{ijmk}}=\mathrm{R}^{\mathrm{kmij}}$. Obviously, f_c, $\mathrm{g}_i=(\nabla_i f)_c$ and $\mathrm{G}_{ij}=(\nabla_i\nabla_j f)_c$ can be obtained by solving the equations (8’)，(12) and (15).

In order to ensure the calculation accuracy, we perform iterations to solve these equations, which can be conveniently realized by computation. At first, the linear approximation is made with $\mathrm{G}_{ij}=0$. Therefore, from the formulas (8’) and (13)，we obtain the physical quantity and its linear gradient at the barycenter as

$$f_{\mathrm{c}}=\frac{1}{\mathrm{N}}\sum_{\alpha}f_{(\alpha)}, \tag{17}$$

and

$$\mathrm{G}_{\mathrm{i}}=(\nabla_{\mathrm{i}}f)_c=\left(\mathrm{R}^{-1}\right)_{\mathrm{ik}}\cdot\frac{1}{\mathrm{N}}\sum_{\varepsilon}^{\mathrm{N}}\left(x_{(\alpha)}^{\mathrm{k}}-x_c^{\mathrm{k}}\right)f_{\alpha}, \tag{18}$$

respectively. Secondly, by substituting the above two equations into (15)，we can get

$$\frac{1}{2}\mathrm{R}^{\mathrm{ijkm}}\mathrm{G}_{\mathrm{km}}=\frac{1}{\mathrm{N}}\sum_{\alpha=1}^{\mathrm{N}}f_{(\alpha)}\Delta x_{(\alpha)}^{\mathrm{i}}\,\Delta x_{(\alpha)}^{\mathrm{j}}-f_{\mathrm{c}}\mathrm{R}^{\mathrm{ij}}-\mathrm{R}^{\mathrm{ijk}}\mathrm{g}_{\mathrm{k}}, \tag{19}$$

with which the quadratic gradient G_{km} at the zero-order can be attained. the zero-order quadratic gradient G_{km} into (8') and (13) to yield the physical quantity f_c at the second order and its linear gradient $g_i = (\nabla_i f)_c$ at the first order; and again by using Eq. (19) to get the corrected quadratic gradient G_{km} at the first order. Repeat the above processes, so as to yield the solutions of Eqs. (8'), (12) and (15), i.e., the estimations of the 10 parameters (f_c, $g_i = (\nabla_i f)_c$, $G_{ij} = (\nabla_i \nabla_j f)_c$) of the plasma structure investigated.

Equation (19) is a tensor equation, which concrete solution we need to find. Rewrite it as the following expression

$$\sum_{l=1}^{3}\sum_{k=1}^{3} R^{ijkl} G_{kl} = c^{ij}, \quad i, j = 1, 2, 3. \tag{20}$$

The tensor at the right-hand side of the above equation is defined as

$$c^{ij} \equiv \frac{2}{N}\sum_{\alpha=1}^{N} f_{(\alpha)} \Delta x^{i}_{(\alpha)} \Delta x^{j}_{(\alpha)} - 2 f_c R^{ij} - 2R^{ijk} G_k . \tag{21}$$

We will transform the tensor equation (20) into a matrix equation so as to obtain its solution concisely. The second-order tensor c^{ij} is symmetric, i.e., $c^{ij} = c^{ji}$. c^{ij} contains 6 independent components, which can be expressed as $c^{(ij)} = \left(c^{11}, c^{12}, c^{13}, c^{22}, c^{23}, c^{33}\right)$. Similarly, the symmetric underdetermined tensor G_{ij} also contains 6 independent components, which can be written as $G_{(ij)} = \left(G_{11}, G_{12}, G_{13}, G_{22}, G_{23}, G_{33}\right)$. The fouth-order tensor R^{ijkl} is symmetric, and $R^{ijkl} = R^{(ij)(kl)}$, where both ij and kl have six independent compositions. Therefore, the tensor equation (20) can be rewritten as

$$\sum_{l=k}^{3}\sum_{k=1}^{3} (2-\delta_{kl}) R^{ijkl} G_{kl} = c^{ij}, \quad (i = 1, 2, 3,\ j = i, \cdots, 3) \tag{22}$$

To facilitate the calculation, the coefficient at the left-hand side of the above equation should be index symmetric. Multiplying the two side of Eq. (22) by $(2-\delta_{ij})$ to yield

$$\sum_{l=k}^{3}\sum_{k=1}^{3}(2-\delta_{ij})(2-\delta_{kl})R^{ijkl}G_{kl}=(2-\delta_{ij})c^{ij},\quad (i=1,2,3,\ j=i,\cdots,3.) \tag{23}$$

Note that in the above formula the sum over the indices i and j are not made even if i and j are repeated. The formula (23) can be regarded as a matrix equation in a 6-dimensional space. The bases of this 6-dimensional space are ($\hat{\mathbf{X}}_1\hat{\mathbf{X}}_1,\hat{\mathbf{X}}_1\hat{\mathbf{X}}_2,\hat{\mathbf{X}}_1\hat{\mathbf{X}}_3,\hat{\mathbf{X}}_2\hat{\mathbf{X}}_2,\hat{\mathbf{X}}_2\hat{\mathbf{X}}_3,\hat{\mathbf{X}}_3\hat{\mathbf{X}}_3$), which can also be marked as $\left(\hat{\boldsymbol{k}}_1,\hat{\boldsymbol{k}}_2,\cdots,\hat{\boldsymbol{k}}_6\right)$, or $\hat{\boldsymbol{k}}_M$, M=1, 2, … , 6, satisfying $\hat{\boldsymbol{k}}_M\cdot\hat{\boldsymbol{k}}_N=\delta_{MN}$. The underdetermined tensor G_{ij}, which is composed of 6 independent components, can be treated as a vector in the 6-dimensional space and written as $\boldsymbol{G}=\left(X^1,X^2,\cdots,X^6\right)$ with its components

$$\boldsymbol{X}^M=\boldsymbol{G}_{(kl)}\,. \tag{24}$$

It can be expressed in vector format as

$$\boldsymbol{G}=\sum_{M=1}^{6}X^M\hat{\boldsymbol{k}}_M \tag{24'}$$

The term $(2-\delta_{ij})c^{ij}$ at the right-hand side of equation (23) is composed of 6 components, can also be regarded as a vector in the 6-dimensional space and expressed as $\boldsymbol{C}=\left(C^1,C^2,\cdots,C^6\right)$, with the components

$$C^M=(2-\delta_{ij})c^{(ij)}. \tag{25}$$

Thus the vector $\boldsymbol{C}$ in the 6-dimensional space is written as

$$\boldsymbol{C}=\sum_{M=1}^{6}C^M\hat{\boldsymbol{k}}_M\,. \tag{26}$$

At the same time, the coefficient tensor $(2-\delta_{ij})(2-\delta_{kl})R^{ijkl}$ can be treated as a 6×6 matrix：

$$\Re^{MN} \equiv (2-\delta_{ij})(2-\delta_{kl})R^{(ij)(kl)} \tag{27}$$

The index M corresponds to (ij), and N to (kl). The matrix $\Re^{MN}$ is symmetric and $\Re^{MN} = \Re^{NM}$. It can be expressed in vector format as

$$\Re = \Re^{MN} \hat{\boldsymbol{k}}_M \hat{\boldsymbol{k}}_N . \tag{28}$$

Just like the 3×3 volumetric matrix R^{ij}, the 6×6 matrix $\Re^{MN}$ respects the characteristic geometric features of the constellation.

Therefore, the tensor equation (20) has been transformed into a matrix equation as follows:

$$\Re^{MN} \cdot X^N = C^M , \tag{29}$$

which vector form is

$$\Re \cdot \mathbf{G} = \mathbf{C} . \tag{29'}$$

The symmetric matrix $\Re^{MN}$ can be diagonalized. Suppose that its eigenvectors are $(\hat{\boldsymbol{e}}_1, \hat{\boldsymbol{e}}_2, \cdots, \hat{\boldsymbol{e}}_6)$ with $\hat{\boldsymbol{e}}_M \cdot \hat{\boldsymbol{e}}_N = \delta_{MN}$, and its eigenvalues $(\Lambda_1, \Lambda_2, \cdots\cdots, \Lambda_6)$ with $\Lambda_1 \geq \Lambda_2 \geq \cdots \geq \Lambda_6 \geq 0$. The relationship between the eigenvectors $(\hat{\boldsymbol{e}}_1, \hat{\boldsymbol{e}}_2, \cdots, \hat{\boldsymbol{e}}_6)$ and the bases $(\hat{\boldsymbol{k}}_1, \hat{\boldsymbol{k}}_2, \cdots, \hat{\boldsymbol{k}}_6)$ is

$$\hat{\boldsymbol{e}}_M = \xi_{MN} \hat{\boldsymbol{k}}_N . \tag{30}$$

Then $\Re$ can be written as

$$\Re = \sum_{M=1}^{6} \Lambda_M \hat{\boldsymbol{e}}_M \hat{\boldsymbol{e}}_M . \tag{31}$$

In the eigenspace $(\hat{\boldsymbol{e}}_1, \hat{\boldsymbol{e}}_2, \cdots, \hat{\boldsymbol{e}}_6)$ of $\Re^{MN}$, $\boldsymbol{G}$ and $\boldsymbol{C}$ can be expressed as

$$\boldsymbol{G} = \sum_{M=1}^{6} \tilde{X}^M \hat{\boldsymbol{e}}_M , \tag{32}$$

and

$$\boldsymbol{C} = \sum_{M=1}^{6} \tilde{C}^M \hat{\boldsymbol{e}}_M \,, \tag{33}$$

Respectively.

Substituting (31), (32) and (33) into (29’), we get

$$\Lambda_M \tilde{X}^M \hat{\boldsymbol{e}}_M = \tilde{C}^M \hat{\boldsymbol{e}}_M \,. \tag{34}$$

Then

$$\Lambda_M \tilde{X}^M = \tilde{C}^M \,. \tag{35}$$

Thus

$$\tilde{X}^M = \frac{1}{\Lambda_M} \tilde{C}^M \,. \tag{36}$$

In the above formula, it is required that $\Lambda_L > 0$. If the eigenvalue $\Lambda_L = 0$, $\tilde{X}^L$ can not be determined.

Therefore,

$$\boldsymbol{G} = \sum_{M=1}^{6} \tilde{X}^M \hat{\boldsymbol{e}}_M = \sum_{M=1}^{6} \frac{1}{\Lambda_M} \tilde{C}^M \hat{\boldsymbol{e}}_M = \sum_{M,N=1}^{6} \frac{1}{\Lambda_M} \tilde{C}^M \xi_{MN} \hat{\boldsymbol{k}}_N \tag{37}$$

Comparing (32) and (37) leads to

$$X^N = \sum_{M,N=1}^{6} \frac{1}{\Lambda_M} \tilde{C}^M \xi_{MN} \,. \tag{38}$$

From (26), (30) and (33), we can get

$$\tilde{C}^M = \sum_{L}^{6} \xi_{ML} C^L \,. \tag{39}$$

Finally, the formula (38) becomes

$$X^N = \sum_{M,N,L}^{6} \frac{1}{\Lambda_M} \xi_{MN} \xi_{ML} C^L \,, \tag{40}$$

which is the solution for the 6 independent components of the quadratic gradient at the barycenter of the constellation in the Earth center reference frame.

In order to obtain a more accurate quadratic gradient, an iterative method is used. Correct the physical quantity f_c and its linear gradient $g_i = (\nabla_i f)_c$ at the barycenter by substituting the quadratic gradient G_{ij} attained from (40) into (8') and (13); Calculate the corrected tensor $\mathbf{C}^{\mathrm{ij}}$ by the expression (21); Further calculate the components of the 6-dimensional vector $\boldsymbol{C}$, $C^M = (2-\delta_{ij})c^{(ij)}$; Then get the components of the quadratic gradient at the barycenter, $\boldsymbol{X}^N = \boldsymbol{G}_{(kl)}$ from the formula (40), which have been corrected by the first iteration. Repeating the above cycle till satisfactory accuracy is achieved. This iteration method will be tested and its reliability verified in the next section.

The estimation of the quadratic gradient of a physical quantity relies on the configuration of the constellation. We can get the complete quadratic gradient if all the 6 eigenvalues of the characteristic matrix $\Re^{MN}$ are non-zero. However, as shown in the expression (40), the quadratic gradient can not be completely determined if one or more eigenvalues of the characteristic matrix $\Re^{MN}$ are zero. For example, if the constellation is linearly distributed, it can be seen from the definitions (16) and (27) that only the eigenvalue of the characteristic matrix $\Re^{MN}$ along the spacecraft array is larger than zero, while all the other 5 eigenvalues of the characteristic matrix $\Re^{MN}$ are equal to zero. Therefore, only the quadratic gradient along the spacecraft array can be attained in this situation. For the situation when the constellation is planar, the 3 eigenvalues of the characteristic matrix $\Re^{MN}$ along the directions in the spacecraft plane are larger than zero, while all the other 3 eigenvalues are zero. So that only the three components of the quadratic gradient in the constellation plane can be found.

For example, we can obtain the linear and quadratic gradients of the electric potential with this approach based on the $N \geq 10$ spacecraft potential measurements, and further get the electric field and charge density at the barycenter of the constellation. Suppose the electric potential observed at the position $\mathbf{r}_\alpha$ of the spacecraft α is $\phi_{(\alpha)} = \phi(\mathbf{r}_\alpha), \alpha = 1, 2, \cdots, \mathrm{N}$. By using the above algorithm, we can yield the electric potential ϕ_c and its linear and quadratic gradients, $(\nabla\phi)_c$ and $(\nabla^2\phi)_c$, at the barycenter of the constellation. Therefore, the electric field at the barycenter is

$$\mathbf{E} = -(\nabla\phi)_c . \tag{40}$$

With Gauss' law, we get the charge density at the barycenter as follows.

$$\rho = \varepsilon_0 (\nabla \cdot \mathbf{E})_\mathbf{c} = -\varepsilon_0 (\nabla^2\phi)_c . \tag{41}$$

As for the multiple spacecraft magnetic field measurements, thereby we can obtain the magnetic linear and quadratic gradients at the barycenter of the constellation, and further attain the complete geometry of the magnetic field lines (MFLs), including the Frenet frame, the curvature and torsion of the MFLs. Suppose that the magnetic field at the position $\mathbf{r}_\alpha$ of the spacecraft α is $\mathbf{B}_\alpha = \mathbf{B}(\mathbf{r}_\alpha), \alpha = 1,\ 2,\ \cdots,\ \mathrm{N}$. Utilizing the above algorithm, the magnetic field and its linear gradient $(\nabla \mathbf{B})_{\mathrm{c}} = \nabla \mathbf{B}(\mathbf{r}_{\mathrm{c}})$ and quadratic gradient $(\nabla\nabla \mathbf{B})_{\mathrm{c}} = \nabla\nabla \mathbf{B}(\mathbf{r}_{\mathrm{c}})$ at the barycenter of the constellation can be calculated. The tangential vector or the unit magnetic vector of the MFLs is $\hat{\mathbf{b}} = \mathbf{B}/B$. The curvature of the MFLs at the barycenter of the constellation can be estimated by the following formula [Shen et al., 2003；2020]

$$\kappa_{\mathrm{cj}} = \mathrm{B_c}^{-1} \mathrm{b_{ci}} \left(\nabla_{\mathrm{i}} \mathrm{B_j}\right)_{\mathrm{c}} - \mathrm{B_c}^{-1} \mathrm{b_{ci}} \mathrm{b_{cj}} \mathrm{b_{cm}} \left(\nabla_{\mathrm{i}} \mathrm{B_m}\right)_{\mathrm{c}}. \tag{42}$$

The principal normal vector of the MFLs is $\hat{\mathbf{K}} = \boldsymbol{\kappa}/|\boldsymbol{\kappa}|$, and the binormal vector of the MFLs is $\hat{\mathbf{N}} = \mathbf{b} \times \hat{\mathbf{K}}$. From its definition, $\tau \equiv \frac{1}{\kappa} \frac{\mathrm{d}^2 \hat{\mathbf{b}}}{\mathrm{ds}^2} \cdot \hat{\mathbf{N}}$, we can get the torsion of the MFLs at the barycenter of the constellation as the expression [Shen et al., 2020]

$$\tau_{\mathrm{c}} = \kappa_{\mathrm{c}}^{-1} \mathrm{B_c}^{-3} \mathrm{N_{cj}} \mathrm{B_{ci}} \left(\nabla_{\mathrm{i}} \mathrm{B_k}\right)_{\mathrm{c}} \left(\nabla_{\mathrm{k}} \mathrm{B_j}\right)_{\mathrm{c}} + \kappa_{\mathrm{c}}^{-1} \mathrm{B_c}^{-3} \mathrm{N_{cj}} \mathrm{B_{ck}} \mathrm{B_{ci}} \left(\nabla_{\mathrm{k}} \nabla_{\mathrm{i}} \mathrm{B_j}\right)_{\mathrm{c}}. \tag{43}$$

3. Tests

In this section, we will investigate the applicability of the algorithm to the vector field, and check its ability to yield the linear and quadratic magnetic gradients and the complete geometry of the magnetic field lines (MFLs) based on the multiple-points magnetic measurements.

The algorithm has been tested for the cylindrical force-free flux rope, dipole magnetic field and modeled geo-magnetospheric field, so as to evaluate its capability. 15-points measurements have been assumed. The tests are focused on how well the algorithm behaves as iterations are performed and how the truncation errors vary with the increase of relative measurement scale. Assuming L is the size of the constellation and D the local characteristic scale of the magnetic structure, the relative measurement scale is L/D. The influence of the number of spacecraft of the constellation on the truncation errors has also been analyzed.

3.1 Configuration of the constellation

The positions of the 15 spacecraft of the constellation in the barycenter coordinates are generated randomly, which are demonstrated in Figure 1. The three characteristic lengths of the constellation (Harvey, 1998) are $a = 0.75R_E, b = 0.61R_E,\ c = 0.24R_E$, respectively, and hence the size of the constellation is $L \equiv 2a = 1.5R_E$.

The elements of the 6×6 characteristic matrix $\mathfrak{R}^{MN}$ can be calculated by the definition (27), and its six eigenvalues are shown in Table 1. All of them are non-zero, thus the algorithm can be applied to calculate the linear and quadratic gradients with the measurements by this constellation. In the following tests, the configuration of the constellation will be kept unchanged, while its size adjusted by scaling up and down the distances between the spacecraft.

3.2 Flux ropes

The axially symmetric force-free flux rope will be used to test the algorethm developed in Section 2, the magnetic field in which in cylindrical coordinates can be expressed as (Lundquist, 1950)

$$\boldsymbol{B} = B_0[0, J_1(\alpha r), J_0(\alpha r)], \qquad (44)$$

where r is the axial-centric distance, $1/\alpha$ the characteristic scale of the flux rope, J_n the first kind Bessel function of order n, and B_0 is the characteristic magnetic strength in the flux rope. We can set that $\alpha = 1/R_E$ and $B_0 = 60nT$. The overall spatial chracteristic scale of the flux rope is $D = 1/\alpha = 1R_E$. However, when $r < 1/\alpha = 1R_E$, it is proper to set the local characteristic scale as the axial-centric distance r, i.e., $D = r$. The helix angle β of the MFLs in the cylindrical flux rope obeys $\tan\beta = J_0(\alpha r)/J_1(\alpha r)$. The curvature and torsion of the MFLs are expressed as

$$\kappa = \mathrm{r}^{-1}\cos^2\beta \quad (45)$$

and

$$\tau = \kappa \tan\beta , \quad (46)$$

respectively [Shen, et al., 2020].

The linear and quadratic gradients ofthe magnetic field, $\nabla_\mathrm{i}\mathrm{B}_\mathrm{k}$ and $\nabla_\mathrm{i}\nabla_\mathrm{j}\mathrm{B}_\mathrm{k}$, are usually composed of 3*3=9 and 6*3=18 independent components, respectively. Axially symmetric flux rope has two symmetries: the three components of the magnetic field in the cylindrical coordinates are invariants along both the axial and azimuthal directions. So that some components of the quadratic magnetic gradient are zero. It is easy to find that, the 13 independent components of $\nabla_\mathrm{i}\nabla_\mathrm{j}\mathrm{B}_\mathrm{k}$ in Cartesian coordinates at one point of the x-axis are zero, i.e., $\partial_z\partial_i B_j = 0$, and $\partial_x\partial_x B_x = \partial_y\partial_y B_x = \partial_x\partial_y B_y = \partial_x\partial_y B_z = 0$; while the remaining 5 independent components, $\partial_x\partial_y B_x$, $\partial_x\partial_x B_y$, $\partial_y\partial_y B_y$, $\partial_x\partial_x B_z$ and $\partial_y\partial_y B_z$ are non-zero. Similarly, for the linear magnetic gradient, $\nabla_\mathrm{i}\mathrm{B}_\mathrm{j}$, its three components, $\partial_y B_x$, $\partial_x B_y$ and $\partial_x B_z$, are non-vanishing, and all the other 6 components are zero analytically. Without loss of generality, putting the barycenter of the constellation composed of 15 spacecraft at the x-axis, we can focus on checking the calculations of the algorithm on the 5 non-zero independent components of the quadratic magnetic gradient and 3 non-vanishing components of the linear magnetic gradient.

We first investigate the resultant's behavior during iterations. Assume that the barycenter of the constellation is at $[1,0,0]R_E$, and reduce the separations between the spacecraft of the constellation proportionally so that the relative measurement scale L/D$= 0.013$. We have performed the iterative calculation and tracked the errors of the linear and quadratic gradients of the magnetic field, which are plotted in Fig. 2. The relative error (vertical axis), $X_{algorithm}/X_{real} - 1$, before the first iteration is 1 since we assume these quantities vanished at the beginning (not shown in Fig.2). After the first iteration (horizontal axis), some of the relative errors have dropped under 0.3 while others remain high. With more iterations, the errors are decreasing and finally converge to certain fixed values as given by the exact solutions of the original equations. The number of iterations for the solutions to converge is varying and mostly less than 100. This has confirmed the convergence of the iteration method.

Secondly, we investigate the dependence of the truncation errors of the non-zero components of the linear and quadratic magnetic gradients on the relative measurement scale L/D.

We have tested three situations when the barycenter of the 15 spacecraft constellation are located at three representative points, [1,0,0] R_E, [0.5,0,0] R_E and

[0.1,0,0] R_E in Cartesian coordinates, respectively. We scale up and down the original 15-S/C constellation to adjust its characteristic size L. It is shown that, the algorithm yields reliable results for most relative measurement scale L/D.

The evaluation of calculations on the linear magnetic gradient and also the curvature of the magnetic field lines are made, which are illustrated in Figure 3(a),(c), and (e). The calculated linear magnetic gradient and curvature of the MFLs have sound accuracies and their relative errors are all less than 5%. As shown in Figure 3(a),(c), and (e), the relative errors of the three non-vanishing components of the linear magnetic gradient and the curvature of the magnetic field lines are varying at the second-order of L/D.

As shown in Figure 3(b),(d), and (f), the relative error (vertical axis) of the quadratic gradients (solid lines) increases about linearly with L/D (horizontal axis) and are generally less than 5 percent, so do that of the resultant torsion of the magnetic field lines (dashed and dotted lines) with slightly greater errors. Note that all errors shown in Fig.3 are converged. Such small errors imply that the algorithm runs well for the flux rope 15-point measurements.

Due to the magnetic field in the flux rope is generally varying rather slowly in space, the application of the algorithm on it is very effective and good accuracies can be reached as illustrated above. However, the magnetic field in space can have severe spatial variations, e.g., the dipole magnetic field. The strength of the dipolar magnetic field is decreasing by the third power of the distance from the dipole, and the magnetic gradients at every order are comparable. The actual calculations on the linear magnetic gradient and current density of the near-Earth magnetic field based on multiple spacecraft measurements are occasionally not accurate [Yang et al., 2016]. Here, we would like to apply the new algorithm to estimate the linear and quadratic magnetic gradients and check its accuracy and capability.

3.3 Dipole magnetic field

In this subsection, we will analyze the capability of the algorithm for the dipole magnetic field. The dipole field in Cartesian coordinates is assumed as

$$\boldsymbol{B} = \frac{M_z}{r^5}[3xy, 3yz, 3z^2 - r^2], \tag{47}$$

where M_z is the magnetic dipole moment and $r = \sqrt{x^2 + y^2 + z^2}$. It is supposed that the magnetic dipole moment points to the positive z-direction. the magnetic dipole moment is set as $M_z = -30438nT \cdot R_E^3$, which is approximately that of the Earth. It is easy to obtain the analytical expression of the curvature of the MFLs as

$$\kappa = \frac{3}{\mathrm{r}} \frac{\left(1+\cos^2\theta\right)\left|\sin\theta\right|}{\left(1+3\cos^2\theta\right)^{3/2}}, \tag{48}$$

where θ is the polar angle. The MFLs in the dipole magnetic field are plane curves, whose torsion is zero, i.e., $\tau = 0$.

The local characteristic scale D of the magnetic field measured can be chosen to be the distance of the constellation from the dipole, i.e., $\mathrm{D} = \mathrm{r}$.

The configuration of the constellation is the same as that in Subsection 3.1, which is shown in Figure 1. We scale up and down the original 15-S/C constellation to alter the characteristic size L of the constellation.

Firstly, we investigate the convergence behavior of the components of the linear and quadratic magnetic gradients calculated with the algorithm by iterations. The constellation is put at the equatorial plane of the dipole with its coordinates being [3,0,0] R_E, where only 5 independent components of the magnetic quadratic gradient are non-zero. The separations between the spacecraft of the constellation are reduced proportionally so that the relative measurement scale $L/D = 0.013$. The convergence behaviors of the non-vanishing independent components of the linear and quadratic magnetic gradients estimated by the algorithm are illustrated in Figure 4 (a) and (b), respectively, which indicates that the linear and quadratic magnetic gradients attain convergence within about 50 iterations.

Then the algorithm has been utilized to calculate the magnetic linear and quadratic gradients as well as the curvature and torsion of the MFLs in the dipole field as expressed by equation (47) for various characteristic scales of the constellation. The constellation is located at $[3,0,0], [2,0,3], [0,0,3]$ R_E, respectively, which are corresponding to low, middle and high latitudes, respectively. Figure 5 (a,c,e) presents the relative errors of the calculated linear magnetic gradient and curvature of the magnetic field lines by the characteristic scale of the constellation. As shown in Figure 5 (a,c,e), the relative errors of the non-vanishing components of the linear magnetic gradient and the curvature of the magnetic field lines are of the second order of L/D.

As L/D< 0.01, the relative errors of the linear magnetic gradient are less than 5%. Therefore the linear magnetic gradient calculated has higher accuracy than the quadratic magnetic gradient. The variations of the relative errors of the magnetic quadratic gradient calculated with the algorithm by L/D are shown in Figure 5 (b,d,f). It can be seen that the relative errors of the magnetic quadratic gradient are at the first order in L/D. However, the errors in estimating the magnetic gradients are higher than those in the case of flux ropes. This is because that the dipolar magnetic strength is decreasing rather rapidly with the distance from the dipole. It is also shown in Figure 4 (b,d,f) that, as $L/D < 0.01$, the relative errors of the quadratic magnetic gradient are less than 10%.

3.4 Modeled Geomagnetosphere

By including one more dipole, the mirrored dipole, in the Earth's dipole field,

$$\boldsymbol{B} = \frac{M_{z1}}{r_1^5}[3xy, 3yz, 3z^2 - r_1^2] + \frac{M_{z2}}{r_2^5}[3(x - 40R_E)y, 3yz, 3z^2 - r_2^2], \quad (49)$$

the modeled geo-magnetospheric field is strongly inhomogeneous and continuously asymmetric, therefore serves as a scenario whereby the algorithm is tested more strictly and realistically. In Eq. (49), M_{z1} is the Earth's dipole moment, and $r_1 = \sqrt{x^2 + y^2 + z^2}$ the distance of the measurement point from the Earth's dipole. The mirror magnetic dipole, $M_{z2} = 28M_{z1}$, is located at $x = 40R_E$, and $r_2 = \sqrt{(x - 40R_E)^2 + y^2 + z^2}$ is the distance from the mirror dipole. In general, the modeled magnetospheric field is approximately equal to the Earth's dipole field in the inner region, $r_1 \leq 6R_E$. Since the dipole field has been tested in the last subsection, we would focus on the outer region, $r_1 > 6R_E$. Three points, [5, 15, 5] R_E, [5, 10, 10] R_E and [-5, 15, 10] R_E , corresponding to the far flank and high latitude at dayside and high latitude far flank at nightside, respectively, are chosen as the locations of the barycenter. Here we define the relative errors of the components $\partial_j B_i$ and $\partial_k \partial_j B_i$ as

$$e_{ij} = \frac{(\partial_j B_i)_{algorithm} - (\partial_j B_i)_{real}}{\langle \partial B \rangle}, \tag{50}$$

and

$$e_{ijk} = \frac{(\partial_k \partial_j B_i)_{algorithm} - (\partial_k \partial_j B_i)_{real}}{\langle \partial\partial B \rangle}, \tag{51}$$

respectively, where $\langle \partial B \rangle = \sum_{i,j}^{3} |\partial_j B_i| /9$ and $\langle \partial\partial B \rangle = \sum_{i,j,k}^{3} |\partial_k \partial_j B_i| /27$ are the average values of the components of linear and quadratic magnetic gradients, respectively. Figure 6 shows the convergent trend of the linear and quadratic gradients within 50 iterations when the separation between the spacecraft in the constellation is adjusted to make $L/D = 0.026$. Again the algorithm is confirmed to be reliable and suitable for analyzing fields severely varying in space.

Figure 7 illustrates the relative errors of all components of the linear and quadratic gradient calculated at different S/C scales. Due to the inhomogeneity and asymmetry of the geo-magnetospheric field, all components are non-vanishing. It is found that the linear gradients increase quadratically with L/D and quadratic gradients linearly with L/D. As $L/D < 0.01$, the relative errors of the quadratic gradient are below 10% , and those of the linear gradient below 5%. The accuracy of the algorithm for the modeled magnetospheric field is close to that for the dipole field.

The global geometry of the magnetospheric magnetic field can also serve as an elaborate scenario for testing. The geometrical features of the MFLs can be depicted by the curvature κ and torsion τ commonly. On the other hand, they can also be represented by another set of parameters, the radius of curvature and spiral angle, (R_c, β) [Apendix E in Shen, et al., 2020]. We have compared the analytical distributions of the radius of curvature and spiral angle of MFLs in $x = 0$ plane and those calculated based on the algorithm, and the results are as shown in figure 8 . Note that we have only modeled the region with （$y > 0, z > 0$）, one quarter of the magnetosphere, on considering the north-south and dawn-dusk symmetries of the modeled magnetosphere. Analytically, the modeled geomagnetic field has mirror symmetry about the z=0 coordinate plane (or the equatorial plane), so that the torsion of the MFLs is negated through the mirror and will be zero at the equatorial plane with z=0, as indicated in the panel (c) of Figure 8. The separation between the spacecraft is fixed to $L = 28km$. With the ever-changing D when we move the constellation around, the largest relative scale is$L/D = 0.0545$ at left-bottom corner (near the Earth), while the least scale $L/D = 0.00400$ at right-top corner. The raduis of curvature given by the algorithm is almost identical to its real value, as shown in the top panels of Figure (8).The MFLs tend to be more straight at the polar region and more bending at the low latitude region. The distribution of the spiral angle of the MFLs as attained by the algorithm is shown in Panel (d) of Figure (8), which is in good consistency with that analytically calculated as demonstrated in Panel (c). Both of them show the strong twist of the MFLs in the duskside cusp region. It is noted that at the low attitude polar region, the algorithm yields negative spiral angles of the MFLs, as shown in the deep blue area in Panel (d). This abnormal deviation from the accurate calculation mainly results from the extremely small curvature of the MFLs in this region.

In this test, 15 points measurements are applied and have verified the feasibility and accuracy of the algorithm. The algorithm needs at least 10 point measurements as input to estimate the quadratic gradient reliably. The more points the algorithm builds on, the more accurate the estimated quadratic gradients are.

To investigate this relationship, we need to exclude the effect of the spatial distribution of the constellation. For n points modeling, we have generated 1000 constellations spontanously, each of which consisting of n S/C, and then choose one constellation with minimum error of the calculation as the representative one. Figure 9 shows the mean relative errors of the linear and quadratic magnetic gradients at $[1,1,2]R_E$ in the modeled magnetospheric field derived from virtual measurements by constellations with different numbers of spacecraft, n, and two fixed characteristic spatial scales, L. As indicated by the dashed magenta lines, the mean error of the quadratic gradient is nearly proportional to $1/n$. The mean error of the linear-gradient, however, appears to be a constant plus a weak variation by the S/C number of the constellation. The averaged mean error of the linear magnetic gradient is about 2.07×10^{-1} as $L/D = 0.05$ and 8.28×10^{-3} as $L/D = 0.01$. As indicated from Figure 9, the results obtained here also confirm the previous arguments that the errors of the linear-gradient components decrease quadratically with L/D, and that of quadratic-gradient components linearly with L/D (see Fig. 9).

4 Summary and Conclusion

The algorithms for calculating the linear gradients of physical quantities based on the measurements by constellations composed of ≥4 spacecraft have been well established and found wide applications in Cluster, THEMIS and MMS data analyses. Recently a special algorithm for estimating the quadratic magnetic gradient utilizing the 4-point magnetic and particle observations has been developed and successfully applied in MMS data analysis [Shen et al. 2020]. With the evolution of space explorations, 10 or more S/C constellations can possibly be realized in the near future. Therefore it is meaningful to develop the method to draw the high order gradients of the physical quantities based on ≥10 point measurements so as to make well preparations for the future multiple point data analysis.

In this investigation, we have established the joint algorithm to deduce the linear and quadratic gradients of an arbitrary physical quantity by using the least square method. This approach can yield the linear and quadratic gradients at the barycenter of the constellation with the input of ≥10 point measurements. With the least square method, the equations for determining the physical quantity and its linear and quadratic gradients at the barycenter have been found. To solve these equations, iterations are made to find the approximation solutions. Firstly, under the linear approximation, the linear gradient is obtained from the multiple point measurements. Secondly, the quadratic gradient is calculated on these bases. Thirdly, the first iteration is made and the quantity and its linear gradient at the barycenter are modified with the obtained quadratic gradient. Then, the quadratic gradient is recalculated with the corrected values of the physical quantity and its linear gradient. The iterations are performed until the linear and quadratic gradients with satisfactory accuracies have been attained.

Generally, the determination of the 3 components of a physical quantity is dependent of the 3×3 volume matrix that reflects the configuration of the constellation. This exploration indicates that the calculations of the 6 independent components of the quadratic gradient rely on the 6×6 symmetric characteristic matrix $\Re^{MN}$ of the constellation. If the 6 eigenvalues of the characteristic matrix $\Re^{MN}$ are all nonzero, the 6 components of the quadratic gradient can be determined completely.

With the 10 point electric potential observations, the linear and quadratic gradients at the barycenter can be found, as well as the electric field and charge density. With the 10 point magnetic field measurements, the linear and quadratic magnetic gradients at the barycenter can be obtained, as well as the complete geometry of the magnetic field lines.

The tests on the algorithm have been made with the cylindrical flux ropes, dipole magnetic field and modeled geo-magnetospheric field, and the reliability and accuracy have been confirmed. In the test, the spatial distribution of the geometrical parameters (radius of the curvature and spiral angle) of the MFLs in the modeled geo-magnetospheric field has also been yielded, which are in well consistence with the analytic results. All the three tests show that, the calculations converge within 50 iterations. The attained linear gradient is at the second order accuracy, while the quadratic gradient at the first order accuracy. The test on the modeled geo-magnetospheric field indicates that increasing the number of the spacecraft in the constellation can enhance the accuracy of the quadratic gradient calculated and its relative errors are anti-proportional to the number of the S/C. However, the accuracy of the linear gradient yielded can not be further improved by increasing the number of the S/C, and its relative errors are almost independent of the number of the S/C. So that it is a very effective, reliable and accurate algorithm for jointly calculating the linear and quadratic gradients of various physical quantities with ≥10 point constellation measurements.

This approach can be used to calculate the complete geometrical parameters of the magnetic field (e.g., the curvature and torsion of the MFLs) in the magnetosphere (e.g., with T models) numerically. This algorithm is also very meaningful for the design of the future multiple S/C missions. For a constellation with 10 or more spacecraft, its characteristic matrix $\Re^{MN}$ needs to have six non-zero eigenvalues thus to make the complete determination of the quadratic gradients of the physical quantities possible. This algorithm will obviously find wide applications in the analysis of multiple point observation data.

Acknowledgments. This work was supported by National Natural Science Foundation (NSFC) of China Grant (No. 41874190, 41704168) and Shenzhen Technology Project (JCYJ20190806144013077). No observation data has been used in this investigation.

References

Chanteur, G. (1998), Spatial Interpolation for four spacecraft: Theory, in *Analysis Methods for Multi-Spacecraft Data*, edited by G. Paschmann and P. W.Daly, p. 349, ESA Publ. Div., Noordwijk, Netherlands.

De Keyser, J., Dunlop, M. W., Darrouzet, F., and D´ecr´eau, P. M. E.: Least-squares gradient calculation from multi-point observations of scalar and vector fields: Methodology and applications with Cluster in the plasmasphere, Ann. Geophys., 25, 971–987, 2007, http://www.ann-geophys.net/25/971/2007/.

Dunlop, M. W., D. J. Southwood, K.-H. Glassmeier, and F. M. Neubauer, Analysis of multipoint magnetometer data, Adv. Space Res., 8, 273, 1988.

Escoubet, C. P., Fehringer, M., & Goldstein, M. (2001), Introduction: The Cluster mission,*AnnalesGeophysicae*, *19*, 1197-1200,https://doi.org/10.5194/angeo-19-197-2001.

Harvey, C. C. (1998), Spatial gradients and the volumetric tensor, in *Analysis Methods for Multi-Spacecraft Data*, edited by G. Paschmann and P. W. Daly, p. 307, ESA Publications Division, Noordwijk, The Netherlands.

Lundquist, S. (1950). Magnetohydrostatic fields. Ark. Fys., 2, 361–365.

Russell, C. T., Anderson, B. J., Baumjohann, W., Bromund, K. R., Dearborn, D., Fischer, D., et al. (2016), The MagnetosphericMultiscale magnetometers,*Space Science Reviews, 199*(1-4), 189-256, https://doi.org/10.1007/s11214‐014‐0057‐3.

Shen, C., X. Li, M. Dunlop, Z. X. Liu, A. Balogh, D. N. Baker, M. Hapgood, and X.

Wang (2003), Analyses on the geometrical structure of magnetic field in the current sheet based on cluster measurements, *J. Geophys. Res.*, *108*(A5), 1168, doi:10.1029/2002JA009612.

Shen, C., C. Zhang, Z. J. Rong, Z. Y. Pu, M. Dunlop, C. P. Escoubet, C. T. Russell, G. Zeng, N. Ren, J. L. Burch, Y. F. Zhou (2020), The quadratic magnetic gradient and complete geometry of magnetic field lines deduced from multiple spacecraft measurements, *J. Geophys. Res.*, in submission.

Shue, J.-H., et al. (1998), Magnetopause location under extreme solar wind conditions, *J. Geophys. Res.*, *103*, 17,691, DOI: 10.1029/98JA01103.

Torbert, R. B., Dors, I., Argall, M. R., Genestreti, K. J., Burch, J. L., Farrugia, C. J., et al. (2020). A new method of 3-D magnetic field reconstruction. Geophysical Research Letters, 47, e2019GL085542. https://doi.org/ 10.1029/2019GL085542.

Vogt, J., G. Paschmann, and G. Chanteur (2008), Reciprocal Vectors, in Multi-Spacecraft Analysis Methods Revisited, ISSI Sci. Rep., SR-008, edited by G. Paschmann and P. W. Daly, pp. 33–46, Kluwer Academic Pub., Dordrecht, Netherlands.

Vogt, J., A. Albert, and O. Marghitu (2009), Analysis of three-spacecraft data using planar reciprocal vectors: Methodological framework and spatial gradient estimation, Ann. Geophys., 27, 3249–3273, doi:10.5194/angeo-27-3249-2009.

Yang, Y. Y., C. Shen, M. Dunlop, Z. J. Rong, X. Li, V. Angelopoulos, Z. Q. Chen, G. Q. Yan, and Y. Ji (2016), Storm time current distribution in the inner equatorial magnetosphere: THEMIS observations, J. Geophys. Res. Space Physics, 121, doi:10.1002/ 2015JA022145.

Table 1: Eigenvalues (in R_E^4) of the characteristic matrix $\Re^{MN}$

Λ_1	Λ_2	Λ_3	Λ_4	Λ_5	Λ_6
0.03512	0.02385	0.002728	0.008468	0.01130	0.01080

Figure Captions

Figure 1: Schematic view of the distribution of the constellation.

Figure 2: The relative errors of the non-vanishing components of the linear (a) and quadratic (b) magnetic gradients in the flux rope calculated by different numbers of iterations. It is noted that $B_{i,k} = \partial B_i / \partial x_k$, $B_{i,j,k} = \partial^2 B_i / \partial x_j \partial x_k$, where a comma denotes partial differentiation.

Figure 3: Left panels (a),(c), and (e) show the relative errors of three non-vanishing components of the linear magnetic gradient and curvature (κ) of the magnetic field lines in flux rope by L/D calculated for three different locations of the constellation, [1,0,0] R_E, [0.5,0,0] R_E and [0.1,0,0] R_E in Cartesian coordinates, respectively. Right panels (b),(d), and (f) illustrate the relative errors of non-vanishing components of the quadratic magnetic gradient and torsion (τ) of the magnetic field lines in flux rope by L/D calculated for the three different locations of the constellation, [1,0,0] R_E, [0.5,0,0] R_E and [0.1,0,0] R_E in Cartesian coordinates, respectively.

Figure 4: The relative errors of the non-vanishing components of the linear (left panel (a)) and quadratic (right panel (b)) magnetic gradient in the dipole field at the equatorial plane as calculated by different numbers of iterations.

Figure 5: Left panels (a), (c) and (e) show the relative errors of the three non-vanishing components of the linear magnetic gradient and curvature (κ) of the MFLs in the dipole field by L/D calculated for three different locations of the constellation, [3, 0, 0] R_E, [2, 0, 3] R_E and [0, 0, 3] R_E in Cartesian coordinates, respectively. Right panels (b),(d), and (f) illustrate the relative errors of the non-vanishing components of the quadratic magnetic gradient in dipole field by L/D calculated for the three different locations of the constellation, [3, 0, 0] R_E, [2, 0, 3] R_E and [0, 0, 3] R_E in Cartesian coordinates, respectively.

Figure 6: The relative errors of the components of the linear (left panel (a)) and quadratic (right panel (b)) magnetic gradients in the modeled geomagnetic field at the position [-5, 15, 10] R_E as calculated by different numbers of iterations, the scale of the constellation is set as $L/D = 0.026$. In panel (b), dashed, dotted and solid lines with colors are for derivatives of B_1, B_2 and B_3, respectively.

Figure 7: Left panels (a), (c) and (e) demonstrate the relative errors of the components of the linear magnetic gradient and curvature (κ) of the MFLs in the geomagnetic field by L/D calculated for three different locations of the constellation, [-5, 15, 10] R_E, [5, 10, 10] R_E and [5, 15, 5] R_E in Cartesian coordinates, respectively. The black dash-dotted line is for the curvature. Right panels (b), (d) and (f) illustrate the relative errors of the components of the quadratic magnetic gradient and torsion (τ) of the

MFLs in dipole field by L/D calculated for the three different locations of the constellation, [-5, 15, 10] R_E, [5, 10, 10] R_E and [5, 15, 5] R_E in Cartesian coordinates, respectively. The black dotted line is for the torsion.

Figure 8: Distributions of the radius of curvature (top) and helix angle (bottom) of MFLs in the coordinate plane x=0 in modeled magnetosphere based on theoretical (left) and new algorithm (right) calculations. The dashed line indicates the magnetopause when $B_z = 27nT, D_p = 3nPa$ [Shue et al., 1998].

Figure 9: Mean truncation errors of linear (red) and quadratic (blue) gradients for different numbers of measurement points. The modeling is for $L/D = 0.05$ (left) and $L/D = 0.01$ (right) at $[1,1,2]R_E$ in the modeled magnetosphere. The dashed magenta line is a fitted curve.

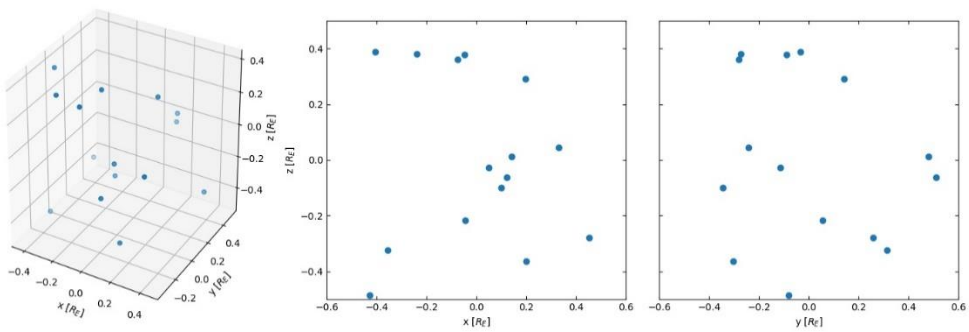

Figure 1: Schematic view of the distribution of the constellation.

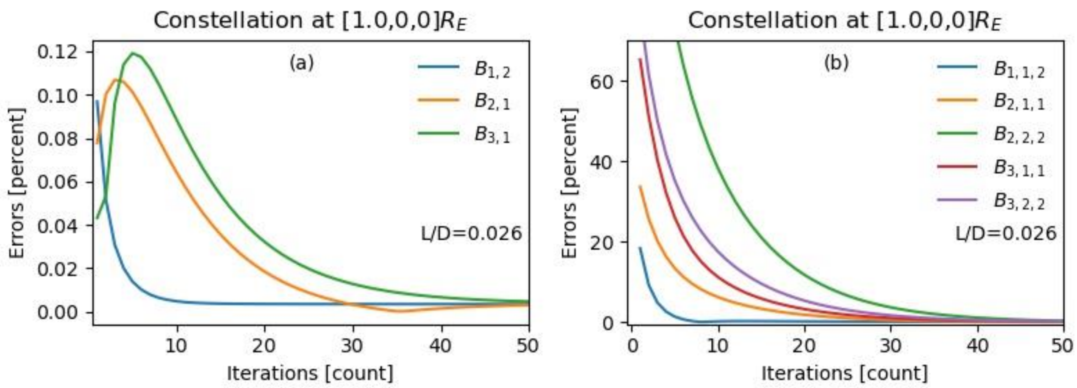

Figure 2: The relative errors of the non-vanishing components of the linear (a) and quadratic (b) magnetic gradients in the flux rope calculated by different numbers of iterations. It is noted that $B_{i,k} = \partial B_i / \partial x_k$, $B_{i,j,k} = \partial^2 B_i / \partial x_j \partial x_k$, where a comma denotes partial differentiation.

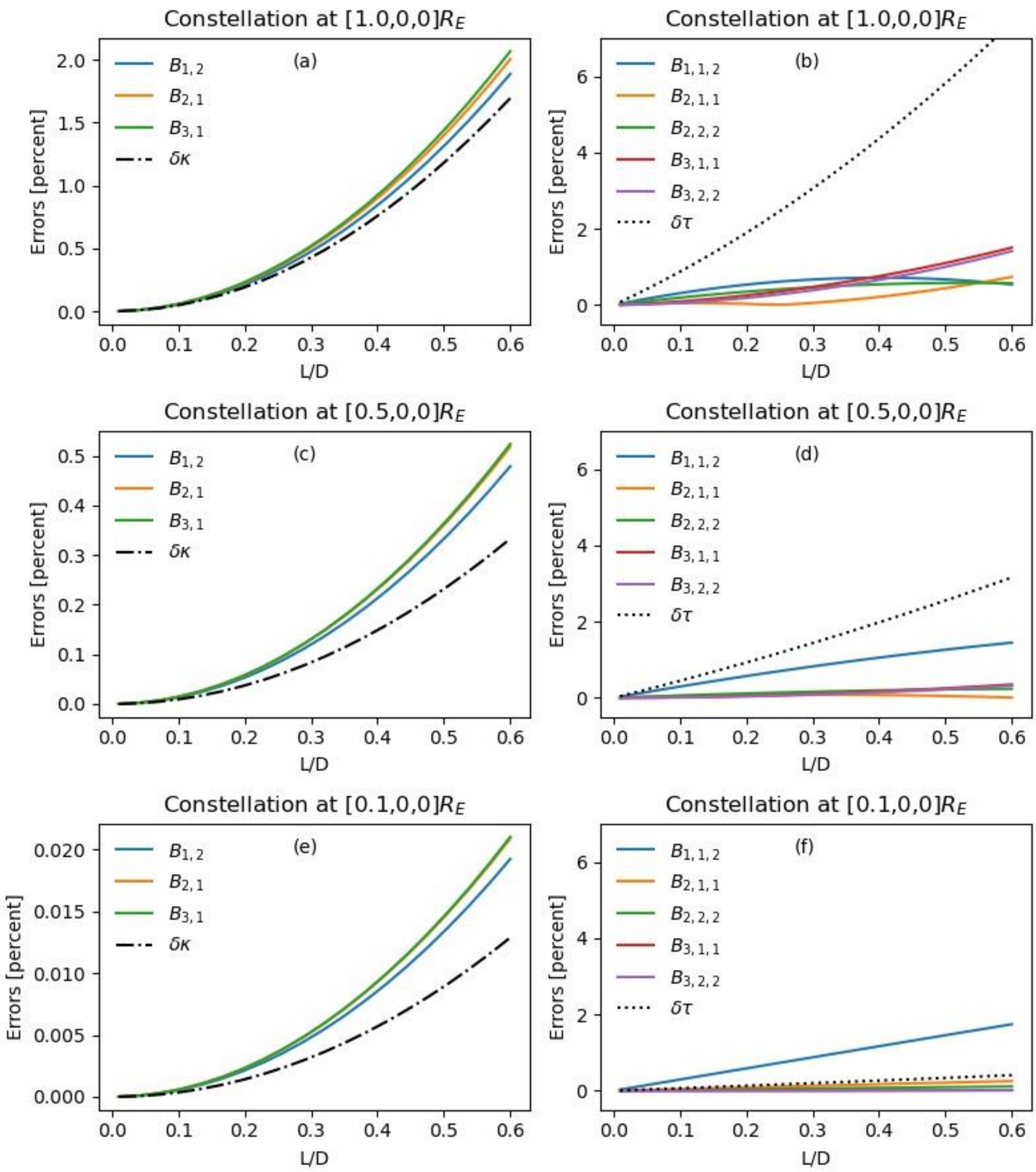

Figure 3: Left panels (a),(c), and (e) show the relative errors of three non-vanishing components of the linear magnetic gradient and curvature (κ) of the magnetic field lines in flux rope by L/D calculated for three different locations of the constellation, [1,0,0] R_E, [0.5,0,0] R_E and [0.1,0,0] R_E in Cartesian coordinates, respectively. Right panels (b),(d), and (f) illustrate the relative errors of non-vanishing components of the quadratic magnetic gradient and torsion (τ) of the magnetic field lines in flux rope by L/D calculated for the three different locations of the constellation, [1,0,0] R_E, [0.5,0,0] R_E and [0.1,0,0] R_E in Cartesian coordinates, respectively.

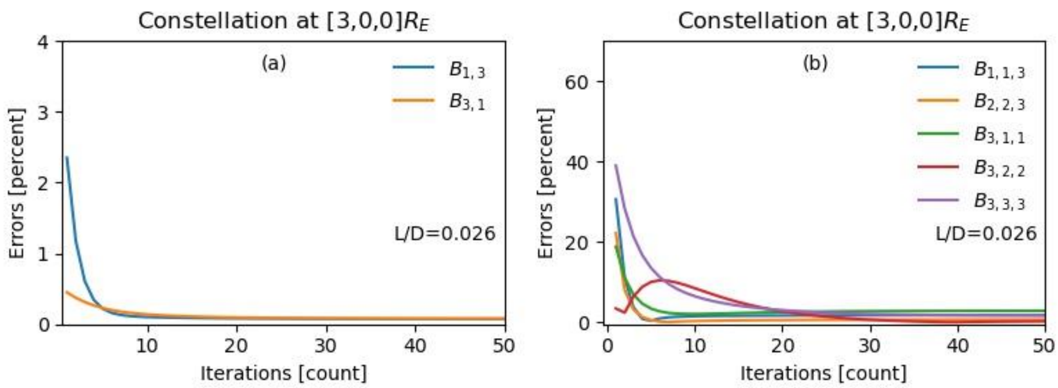

Figure 4: The relative errors of the non-vanishing components of the linear (left panel (a)) and quadratic (right panel (b)) magnetic gradient in the dipole field at the equatorial plane as calculated by different numbers of iterations.

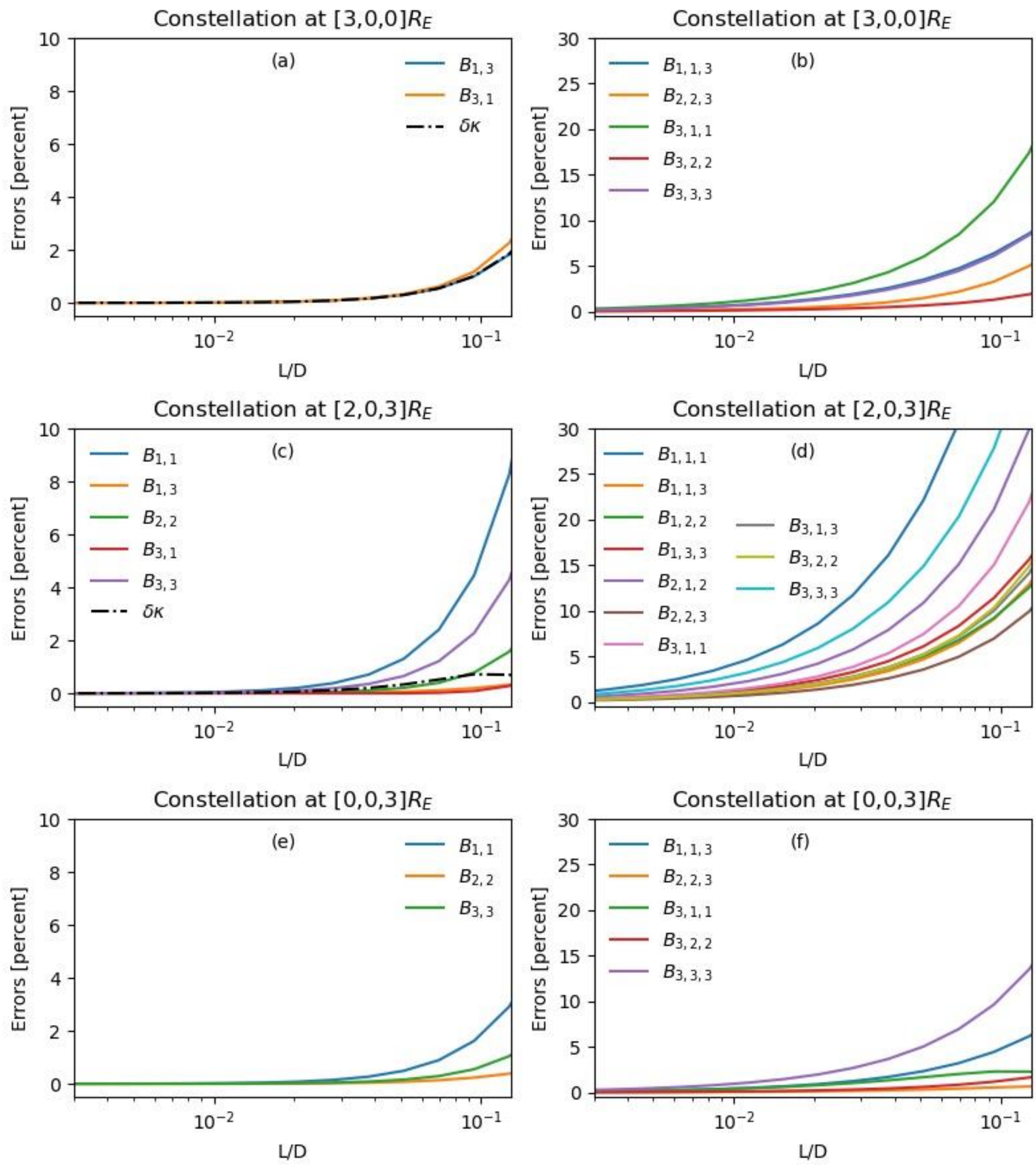

Figure 5: Left panels (a), (c) and (e) show the relative errors of the three non-vanishing components of the linear magnetic gradient and curvature (κ) of the MFLs in the dipole field by L/D calculated for three different locations of the constellation, [3, 0, 0] R_E, [2, 0, 3] R_E and [0, 0, 3] R_E in Cartesian coordinates, respectively. Right panels (b),(d), and (f) illustrate the relative errors of the non-vanishing components of the quadratic magnetic gradient in dipole field by L/D calculated for the three different locations of the constellation, [3, 0, 0] R_E, [2, 0, 3] R_E and [0, 0, 3] R_E in Cartesian coordinates, respectively.

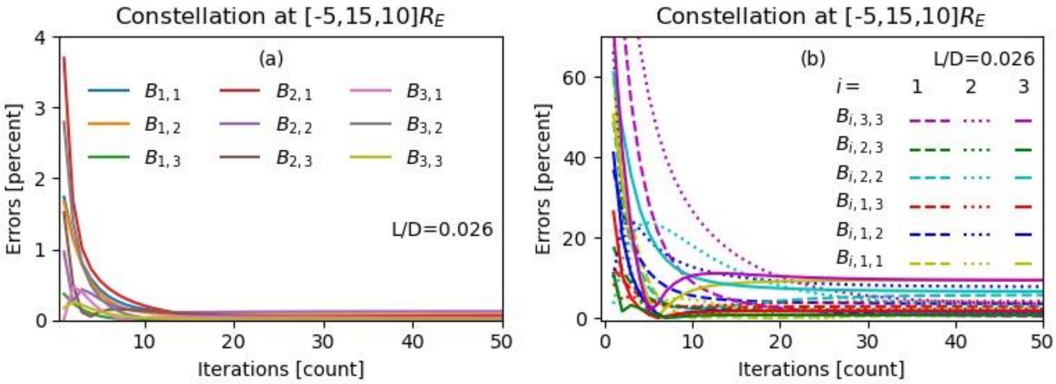

Figure 6: The relative errors of the components of the linear (left panel (a)) and quadratic (right panel (b)) magnetic gradients in the modeled geomagnetic field at the position [-5, 15, 10] R_E as calculated by different numbers of iterations, the scale of the constellation is set as $L/D = 0.026$. In panel (b), dashed, dotted and solid lines with colors are for derivatives of B_1, $\boldsymbol{B_2}$ and B_3, respectively.

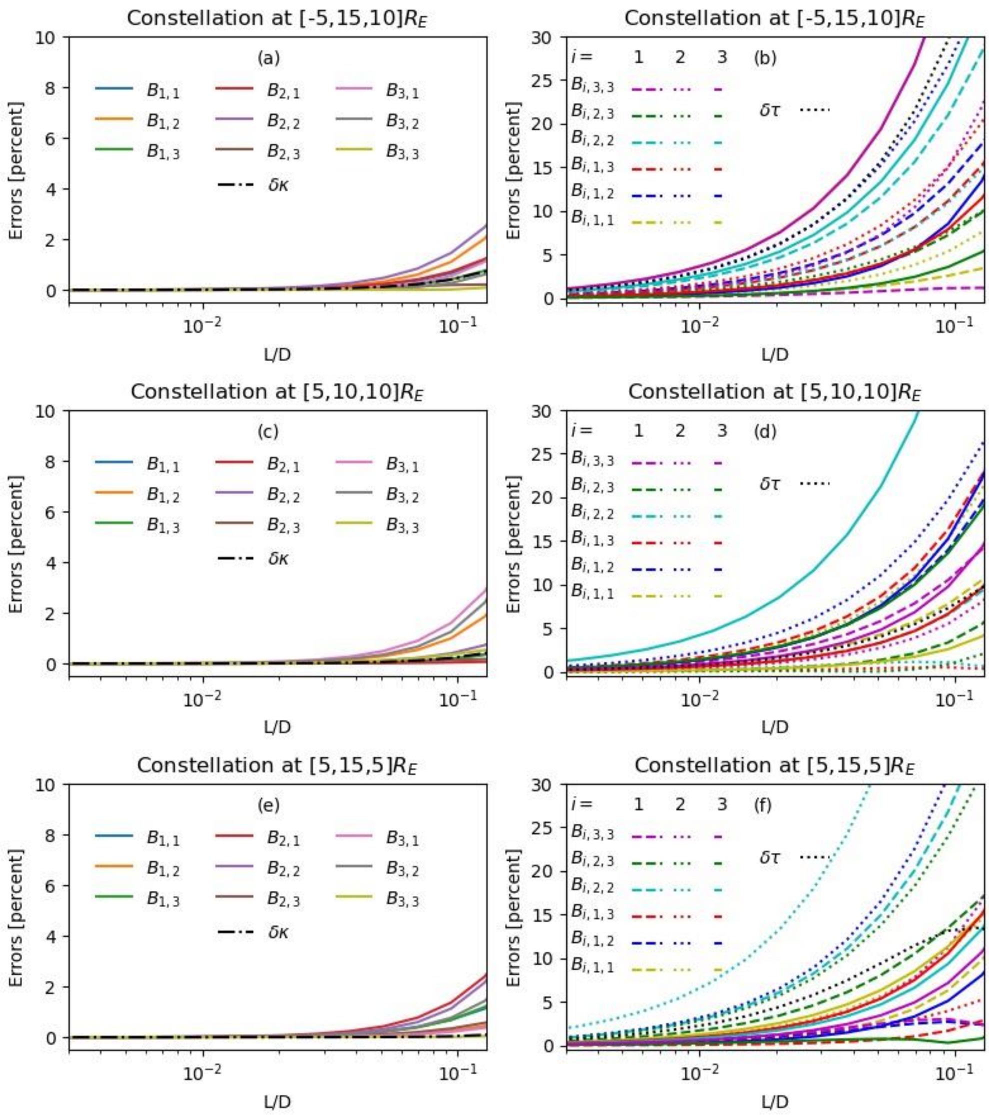

Figure 7: Left panels (a), (c) and (e) demonstrate the relative errors of the components of the linear magnetic gradient and curvature (κ) of the MFLs in the geomagnetic field by L/D calculated for three different locations of the constellation, [-5, 15, 10] R_E, [5, 10, 10] R_E and [5, 15, 5] R_E in Cartesian coordinates, respectively. The black dash-dotted line is for the curvature. Right panels (b), (d) and (f) illustrate the relative errors of the components of the quadratic magnetic gradient and torsion (τ) of the MFLs in dipole field by L/D calculated for the three different locations of the constellation, [-5, 15, 10] R_E, [5, 10, 10] R_E and [5, 15, 5] R_E in Cartesian coordinates, respectively. The black dotted line is for the torsion.

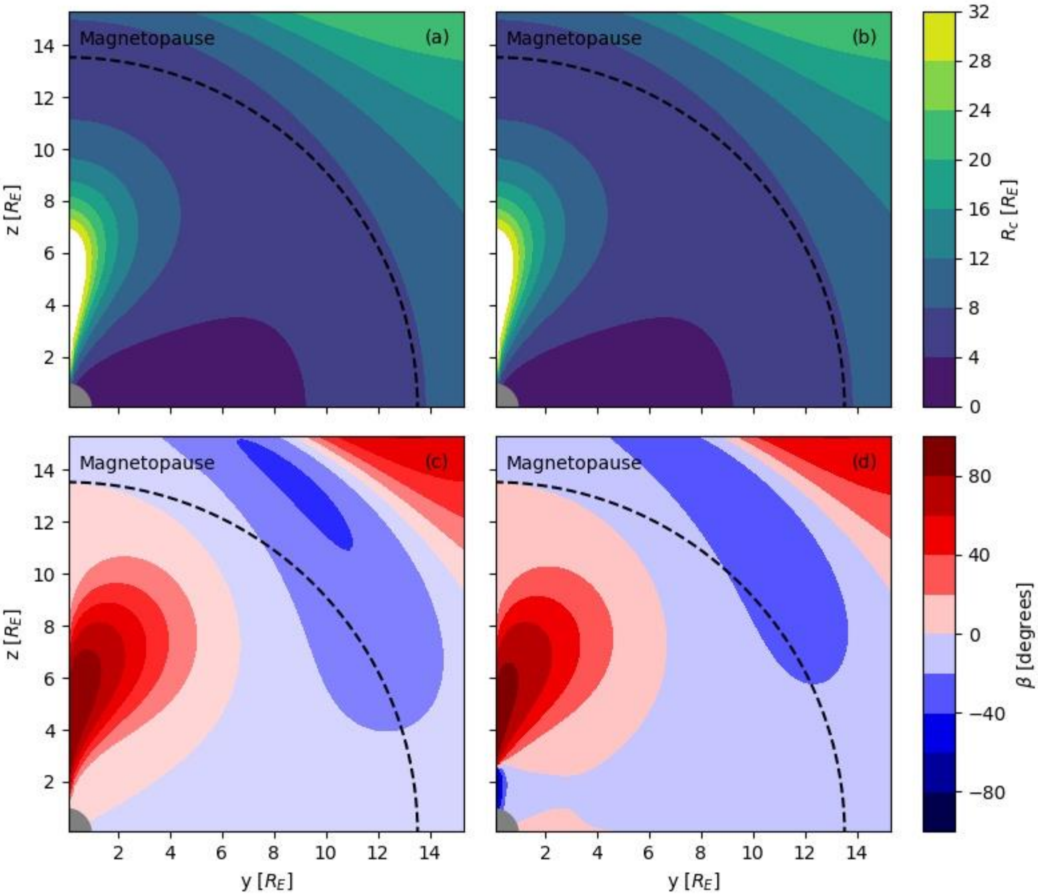

Figure 8: Distributions of the radius of curvature (top) and helix angle (bottom) of MFLs in the coordinate plane x=0 in modeled magnetosphere based on theoretical (left) and new algorithm (right) calculations. The dashed line indicates the magnetopause when $B_z = 27nT, D_p = 3nPa$ [Shue et al., 1998].

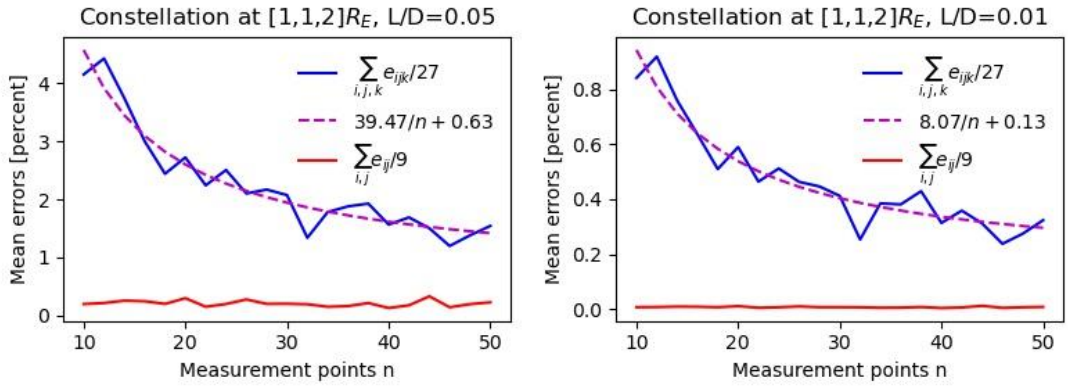

Figure 9: Mean truncation errors of linear (red) and quadratic (blue) gradients for different numbers of measurement points. The modeling is for $L/D = 0.05$ (left) and $L/D = 0.01$ (right) at $[1,1,2]R_E$ in the modeled magnetosphere. The dashed magenta line is a fitted curve.

The Quadratic Magnetic Gradient and Complete Geometry of Magnetic Field Lines Deduced from Multiple Spacecraft Measurements

Chao Shen[1], Chi Zhang[2,3], Zhaojin Rong[2,3], Zuyin Pu[4], M. Dunlop[5, 6], C. Philippe Escoubet[7], C. T. Russell[8], Gang Zeng[9], Nian Ren[1], J. L. Burch[10], Yufei Zhou[1]

[1]School of Science, Harbin Institute of Technology, Shenzhen, 518055, China

[2]Institute of Geology and Geophysics, Chinese Academy of Sciences, Beijing 100029, China

[3]College of Earth Science, University of Chinese Academy of Sciences, Beijing, China

[4]School of Earth and Space Sciences, Peking University, Beijing, China

[5]School of Space and Environment, Beihang University, Beijing, China

[6]Rutherford Appleton Laboratory, Chilton, DIDCOT, Oxfordshire OX11 0QX, United Kingdom

[7]ESA/ESTEC (SCI-SC), Postbus 299, Keplerlaan, 1, 2200 AG Noordwijk, The Netherlands

[8]University of California, Los Angeles, 603 Charles Young Drive, Los Angeles, CA 90095-1567, USA

[9]School of Mathematics and Physics, Jingchu University of Technology, Jingmen, China

[10]Southwest Research Institute, San Antonio, TX, USA

Corresponding author: Chao Shen (shenchao@hit.edu.cn)

Key Points:

An explicit algorithm for the quadratic magnetic gradient based on multi-point measurements with iterations is presented for the first time

The algorithm is applicable for both steady and unsteady structures, and the obtained linear magnetic gradient has second order accuracy

The complete geometry of the magnetic field lines has been obtained, for the first time, based on multi-point measurements

Key Words:

Multiple Spacecraft Measurements, Iteration, Quadratic Magnetic Gradient, Geometry of Magnetic Field Lines, Curvature, Torsion, Current Density, Magnetic Flux Ropes

Abstract

Topological configurations of the magnetic field play key roles in the evolution of space plasmas. This paper presents a novel algorithm that can estimate the quadratic magnetic gradient as well as the complete geometrical features of magnetic field lines, based on magnetic field and current density measurements by a multiple spacecraft constellation at 4 or more points. The explicit estimators for the linear and quadratic gradients, the apparent velocity of the magnetic structure and the curvature and torsion of the magnetic field lines can be obtained with well predicted accuracies. The feasibility and accuracy of the method have been verified with thorough tests. The algorithm has been successfully applied to exhibit the geometrical structure of a flux rope. This algorithm has wide applications for uncovering a variety of magnetic configurations in space plasmas.

Plain Language Summary

The magnetic field plays a key role in the dynamical evolution of space plasmas; it traps and stores plasma particles, and controls the transfer, conversion and release of the energies. The Magnetic field can form various structures, where the magnetic field lines can be bending and twisting. At the present time full imaging of the magnetic field has not been achieved. Therefore, it is very important to estimate the magnetic gradients at every order, as well as the geometrical features (curvature and torsion) of the magnetic field lines (MFLs), from the in situ observations. Although we have successfully deduced the first order magnetic gradient and the curvature from multiple S/C magnetic measurements, it is still not solved how to estimate the high order magnetic gradients and the torsion of MFLs. The research reported here has, for the first time, put forward a novel explicit algorithm, which can acquire the quadratic magnetic gradient and the torsion of MFLs with the 4-point magnetic field and current density measurements as the input. This algorithm has stable accuracies and can be applied effectively to analyze the observations of MMS. This method can find a plenty of applications in space exploration and research.

1. Introduction

A magnetic field can trap plasma populations; control the transfer, conversion and release of energy in planetary magnetospheres; play a key role in the spatial distribution of the plasmas and development of instabilities, as well as controlling the evolution of substorms and storms. The measurement of the magnetic field in space has been carried out by a limited number of sometime collocated spacecraft placed in various locations. It is therefore important and possible to establish the continuous distribution of the magnetic field, based on multi-point magnetic observations. With two point measurements the gradient of the magnetic field along the spacecraft (S/C) separation line can be obtained; With three point magnetic measurements, the magnetic gradient within the S/C constellation plane can be yielded; while with four or more point magnetic measurements, the three dimensional linear magnetic gradient can be estimated (McComas et al.,1986; Harvey, 1998; Chanteur, 1998; Vogt et al., 2008; Shen et al., 2012a, b; Dunlop et al., 2015; Dunlop et al., 2016; Dunlop et al., 2018; Dunlop et al., 2020). In order to get the quadratic magnetic gradient, 10 S/C magnetic measurements are needed (Chanteur, 1998).

In the past, magnetic measurements have been performed with two S/C (ISEE-1/2, DSP, RBSP, ARTEMIS, etc.) [Ogilvie et al., 1977; Liu et al., 2005; Shen et al., 2005; Angelopoulos, 2008], three S/C constellations (THEMIS, Swarm) [Angelopoulos, 2008; Friis-Christensen et al., 2006], and four S/C constellations

(Cluster and MMS) [Escoubet et al., 2001; Balogh et al., 2001; Burch et al., 2016; Russell et al., 2016]. However, presently 10 S/C magnetic field observations in space are on the drawing boards. Deducing the various orders of magnetic gradients fully with a limited number of S/C observations remains an important question.

Attempts to partially solve this problem, have used physical constraints to assist the complete determination of the magnetic gradients [Vogt et al., 2009]. The symmetries in plasma structures and the electromagnetic field laws can also be useful. It has been found by Shen et al., [2012a] that, for a force-free magnetic structure in which the current is field-aligned, the 3 dimensional (3-D) magnetic gradient can be completely obtained with 3 spacecraft magnetic measurements. In their derivation, Ampere's law $\nabla\times\mathbf{B}=\mu_0\mathbf{j}$ and the solenoidal condition of the magnetic field $\nabla\cdot\mathbf{B}=0$ are used to reduce the equations. Furthermore, if the force-free magnetic structure is steady and moving with a known relative velocity, only two S/C magnetic observations are needed to gain the complete 9 components of the linear magnetic gradient [Shen et al., 2012b]. Liu et al. (2019) have suggested a method to get the nonlinear distribution of the magnetic field in a stable plasma structure by fitting the second-order Taylor expansion based on 4 S/C magnetic measurements and one S/C current density observations. Torbert et al. (2020) have successfully obtained the 3 D distribution of the magnetic field by using the 4 point magnetic and particle/current density measurements of MMS. In their exploration, they have applied a fitting method to the magnetic field to the third order in magnetic gradient, named the

“25-parameter fit”. However, there still exists no explicit solution to the determination of the quadratic magnetic gradient based on multiple spacecraft measurements.

With multiple S/C magnetic observations, geometrical features of the magnetic field lines can be obtained [Shen et al., 2003, 2008a, b, 2011, 2014; Rong et al., 2011; Lavraud et al., 2016; Xiao et al., 2018]. The geometry of the magnetic field lines (MFLs) so obtained includes the tangential direction (just the direction of the magnetic vector), principal direction (along the curvature vector), binormal vector (the normal of the osculation plane of one MFL), curvature and torsion. However, the torsion of the MFLs has not been obtained in these previous methods. The reason for this is that the torsion of the MFLs depends on the quadratic magnetic gradient, which needs 10 point S/C magnetic measurements [Chanteur, 1998] to be deduced. Therefore, it is necessary to explore the calculation of the torsion of MFLs based on observations of a limited number of S/C, in order to learn this more complete of MFLs in space.

This problem is addressed herein, where an explicit algorithm has been derived to estimate the quadratic magnetic gradient as well as the complete geometrical parameters of the MFLs based on measurements with a limited number of spacecraft. This approach has a wide range of applications for analyzing the magnetic structure in space plasmas.

2. The estimators for the linear and quadratic gradients of magnetic field

It is very important to obtain the quadratic gradient of the magnetic field. With it, we can grasp more accurately the structure of the magnetic field and, uncover the complete geometrical structure of the MFLs, including the Frenet coordinates and curvature, as well as the torsion. In this section, we obtain the explicit estimator of the quadratic magnetic gradient based on magnetic field and current density measurements from a multi-S/C constellation.

We present the derivations of this algorithm as follows.

The configuration of the four-spacecraft constellation (Cluster or MMS) is illustrated in Figure 1.

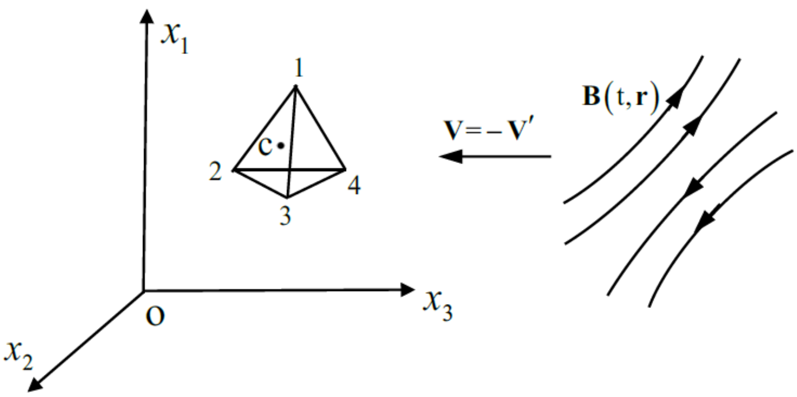

Figure 1. The exploration on the magnetic field in space in the S/C constellation frame of reference. （x_1, x_2, x_3）are the Cartesian coordinates in the S/C constellation reference frame. The S/C constellation is composed of four spacecraft (the number of spacecraft can be more 4), whose barycenter is at the point C. The apparent motional velocity of the magnetic field structure relative to the S/C constellation reference is

$\mathbf{V}$. Conversely, the velocity of the S/C constellation relative to the proper reference of the magnetic field structure is $\mathbf{V}'=-\mathbf{V}$.

In the S/C constellation frame of reference, the simultaneous position vectors of the four spacecraft are $\mathbf{r}_\alpha\left(\alpha=1,2,3,4\right)$ and the position vector of the barycenter of the four S/C is

$$\mathbf{r}_{\mathrm{c}}=\frac{1}{4}\sum_{\alpha=1}^{4}\mathbf{r}_\alpha\,. \tag{1}$$

In this study, the Greek subscripts or superscripts apply to spacecraft, and $\alpha,\ \beta,\ \gamma,\ \cdots=1,2,3,4$; while the Latin subscript c indicates the barycenter.

The apparent motional velocity of the magnetic field structure relative to the S/C constellation reference frame is denoted as $\mathbf{V}$, which may vary from point to point [Hamrin, et al.(2008)]. The velocity of the S/C constellation relative to the proper reference frame of the magnetic field structure is $\mathbf{V}'=-\mathbf{V}$. We establish the Cartesian coordinates （x_1,x_2,x_3）in the S/C constellation reference, and choose the x_3 axis along the direction of $\mathbf{V}'=-\mathbf{V}$ with its basis $\hat{\mathbf{x}}_3=-\mathbf{V}/\mathrm{V}$. The configuration of the S/C constellation is characterized by the volume tensor, which is defined [Harvey, 1998; Shen et al., 2003] as

$$\mathrm{R}_{\mathrm{kj}}=\frac{1}{4}\sum_{\alpha=1}^{4}\left(\mathrm{r}_{\alpha\mathrm{k}}-\mathrm{r}_{\mathrm{ck}}\right)\left(\mathrm{r}_{\alpha\mathrm{j}}-\mathrm{r}_{\mathrm{cj}}\right). \tag{2}$$

We have applied some Latin subscripts or superscripts (other than c) to denote Cartesian coordinates with $\mathrm{i,\ j,\ k,\ e,\ m,\ n}=1,2,3$ and $\mathrm{p,\ q,\ s,\ r}=1,2$.

(i) The linear gradients of the magnetic field and current density at the barycenter

As the MMS S/C cross a magnetic structure, the four S/C measure the magnetic field with high accuracy and time resolution [Russell et al. 2014; Burch et al. 2015]. The magnetic field observed by the αth S/C at position $\mathbf{r}_\alpha$ is

$$\mathbf{B}_\alpha(\mathrm{t}) = \mathbf{B}(\mathrm{t}, \mathbf{r}_\alpha), \alpha = 1,\ 2,\ 3,\ 4. \tag{3}$$

The MMS S/C can measure the distributions of ions and electrons with efficient accuracy to yield the local current density [Torbert et al., 2015, 2020] as

$$\mathbf{j}_\alpha(\mathrm{t}) = \mathbf{j}(\mathrm{t}, \mathbf{r}_\alpha), \alpha = 1,\ 2,\ 3,\ 4. \tag{4}$$

To obtain the magnetic field and its first order gradient at the barycenter of the MMS constellation, we first neglect the second order magnetic gradient under the linear approximation. With four S/C, simultaneous magnetic observations, the magnetic field and its linear gradient at the barycenter of the S/C constellation can be obtained with the previous methods established by Harvey (1998) and Chanteur (1998). In order to suppress the fluctuating components in the magnetic field and obtain the magnetic gradient at higher accuracy, we make use of the time series of the magnetic observations by the four S/C to get the magnetic gradient with the method first put forward by De Keyser, et al. (2007). In their approach, the time series data of the four S/C do not need to be synchronized. Appendix A gives the explicit estimator of the linear gradient of magnetic field in space and time from this approach.

Based on equations (A14) and (A15) in Appendix A, the magnetic field and its first order derivatives at the barycenter of the MMS constellation under the linear approximation are as follows.

$$\mathrm{B_i}(\mathrm{t_c},\mathbf{r}_\mathrm{c}) = \frac{1}{4\mathrm{n}}\sum_{\mathrm{a}=1}^{4\mathrm{n}} \mathrm{B_i}\left(\mathrm{t_a},\mathbf{r}_\mathrm{a}\right), \tag{5}$$

$$\nabla_\nu B_i(\mathrm{t_c},\mathbf{r}_\mathrm{c}) = \mathrm{R}_{\nu\mu}^{-1} \cdot \frac{1}{4\mathrm{n}}\sum_{a=1}^{4\mathrm{n}} \left(x_{(a)}^{\mu} - x_0^{\mu}\right) B_i\left(\mathrm{t_a},\mathbf{r}_\mathrm{a}\right). \tag{6}$$

And the above formulas in the vector format are

$$\mathbf{B}(\mathrm{t_c},\mathbf{r}_\mathrm{c}) = \frac{1}{4\mathrm{n}}\sum_{\mathrm{a}=1}^{4\mathrm{n}} \mathbf{B}\left(\mathrm{t_a},\mathbf{r}_\mathrm{a}\right), \tag{7}$$

$$\nabla_\nu \mathbf{B}(\mathrm{t_c},\mathbf{r}_\mathrm{c}) = \mathrm{R}_{\nu\mu}^{-1} \cdot \frac{1}{4\mathrm{n}}\sum_{a=1}^{4\mathrm{n}} \left(x_{(a)}^{\mu} - x_0^{\mu}\right) \mathbf{B}\left(\mathrm{t_a},\mathbf{r}_\mathrm{a}\right). \tag{8}$$

In the above formulas (5)-(8), the general volume tensor $\mathrm{R}^{\mu\nu}$ in spacetime is defined by (A9). These equations will yield the time series of magnetic field $\mathbf{B}(\mathrm{t_c},\mathbf{r}_\mathrm{c})$, its time derivative $\partial_\mathrm{t}\mathbf{B}(\mathrm{t_c},\mathbf{r}_\mathrm{c})$ and first order gradient $\nabla\mathbf{B}\left(\mathrm{t_c},\mathbf{r}_\mathrm{c}\right)$ at the barycenter of the S/C constellation.

In the above formulas (5)-(8), the accuracy is found to first order due to omission of the second order gradients. We will correct the magnetic field and its first order derivatives at the barycenter with the second order derivatives of the magnetic field according to Appendix A and will further obtain the corrected quadratic magnetic gradient by iteration (see (vii) later). The corrected magnetic field and its first order gradient at the barycenter will then have second order accuracy.

In this investigation, we have neglected the magnetic gradients with orders higher than two, so that the current density can be regarded as linearly varying.

According to the Equations (A14) and (A15) in Appendix A, the current density at the barycenter is

$$\mathbf{j}_{\mathrm{c}} = \mathbf{j}(\mathrm{t_c}, \mathbf{r}_{\mathrm{c}}) = \frac{1}{4\mathrm{n}} \sum_{\mathrm{a}=1}^{4\mathrm{n}} \mathbf{j}\left(\mathrm{t_a}, \mathbf{r}_{\mathrm{a}}\right), \tag{9}$$

and the linear gradient of the current density at the barycenter is

$$\nabla_{\nu} \mathbf{j}(\mathrm{t_c}, \mathbf{r}_{\mathrm{c}}) = \mathrm{R}^{-1}_{\nu\mu} \cdot \frac{1}{4\mathrm{n}} \sum_{a=1}^{4\mathrm{n}} \left(x^{\mu}_{(a)} - x^{\mu}_{0} \right) \mathbf{j}\left(\mathrm{t_a}, \mathbf{r}_{\mathrm{a}}\right), \tag{10}$$

of which the component form is

$$\nabla_{\nu}\, j_k(\mathrm{t_c}, \mathbf{r}_{\mathrm{c}}) = \mathrm{R}^{-1}_{\nu\mu} \cdot \frac{1}{4\mathrm{n}} \sum_{a=1}^{4\mathrm{n}} \left(x^{\mu}_{(a)} - x^{\mu}_{0} \right) j_k\left(\mathrm{t_a}, \mathbf{r}_{\mathrm{a}}\right). \tag{10'}$$

Generally, the electron and ion measurements have different time resolutions. So that the electron and ion current densities and their linear gradients at the barycenter can be first calculated separately with Equations (9) and (10), and finally added to obtain the total current density and its linear gradient at the barycenter.

(ii) The second order time derivative of the magnetic field and the first order time derivative of the magnetic gradient

With the time series of magnetic field $\mathbf{B}(\mathrm{t_c}, \mathbf{r}_{\mathrm{c}})$ and its first order time derivative $\partial_{\mathrm{t}} \mathbf{B}(\mathrm{t_c}, \mathbf{r}_{\mathrm{c}})$ at the barycenter obtained in **(i)**, it is easy to get the second order time derivative of magnetic field $\partial_{\mathrm{t}} \partial_{\mathrm{t}} \mathbf{B}(\mathrm{t_c}, \mathbf{r}_{\mathrm{c}})$ at the barycenter, where $\partial_{\mathrm{t}} \equiv \partial / \partial \mathrm{t}$.

The gradient of the time derivative of the magnetic field is equivalent to the time derivative of the magnetic gradient, i.e.,

$$\nabla_{\mathrm{j}} \partial_{\mathrm{t}} \mathrm{B_i}\left(\mathrm{t}, \mathbf{r}\right) = \partial_{\mathrm{t}} \left[\nabla_{\mathrm{j}} \mathrm{B_i}\left(\mathrm{t}, \mathbf{r}\right) \right]. \tag{11}$$

Therefore, at the central point $(\mathrm{t_c}, \mathbf{r}_{\mathrm{c}})$,

$$\nabla_j \partial_t B_i(t_c, \mathbf{r}_c) = \partial_t \nabla_j B_i(t_c, \mathbf{r}_c) = \frac{\partial}{\partial t_c}\left[\nabla_j B_i(t_c, \mathbf{r}_c)\right]. \tag{12}$$

(iii) The transformations between the temporal and spatial gradients of the magnetic field in different reference frames

This approach will make use of the proper reference frame of the magnetic structure so as to determine the second order gradient in the direction of the apparent motion of the magnetic structure, i.e., the longitudinal quadratic gradient of the magnetic field. To do this, we need to find the apparent velocity $\mathbf{V}$ of the magnetic structure relative to the spacecraft constellation. For space plasmas, this relative velocity is much less than the speed of the light in vacuum, i.e., $V << c$. Shi et al. (2006) have first obtained the velocity of the magnetic structure relative to the spacecraft with the temporal and spatial variation rates of the magnetic field under the assumption of stationarity. Hamrin et al. (2008) have obtained the apparent velocity of the magnetic structure using a proper reference frame. Here we give a concise discussion on the transformations between the temporal and spatial gradients of the magnetic field in different reference frames.

The time and space coordinates (t, $\mathbf{r}$) in the S/C constellation reference frame and the corresponding time and space coordinates (t', $\mathbf{r}'$) in the proper reference frame of the magnetic structure obey the Galilean transformations, i.e., $t'=t$, $\mathbf{r}'=\mathbf{r}$-$\mathbf{V}t$ (see also Figure 1). (The Eulerian description is applied in each reference frame.) The magnetic fields observed in the S/C constellation frame and the proper frame of the magnetic structure are $\mathbf{B}(t,\mathbf{r})$ and $\mathbf{B}'(t',\mathbf{r}')$, respectively. As $V << c$,

$\mathbf{B}(\mathrm{t},\mathbf{r})=\mathbf{B}'(\mathrm{t}',\mathbf{r}')$. It is obvious that the magnetic gradient in these two reference frames are also identical, i.e.,

$$\nabla\mathbf{B}(\mathrm{t},\mathbf{r})=\nabla'\mathbf{B}'(\mathrm{t}',\mathbf{r}'). \tag{13}$$

The relationship between the time derivative of the magnetic field in the S/C constellation, $\frac{\partial\mathbf{B}(\mathrm{t},\mathbf{r})}{\partial\mathrm{t}}$, and time derivative of the magnetic field in the proper reference frame of the magnetic structure, $\frac{\partial\mathbf{B}'(\mathrm{t}',\mathbf{r}')}{\partial\mathrm{t}'}$, is

$$\frac{\partial\mathbf{B}(\mathrm{t},\mathbf{r})}{\partial\mathrm{t}}=\frac{\partial\mathbf{B}'(\mathrm{t}',\mathbf{r}')}{\partial\mathrm{t}}=\frac{\partial\mathrm{t}'}{\partial\mathrm{t}}\frac{\partial\mathbf{B}'(\mathrm{t}',\mathbf{r}')}{\partial\mathrm{t}'}+\frac{\partial\mathbf{r}'}{\partial\mathrm{t}}\cdot\nabla'\mathbf{B}'(\mathrm{t}',\mathbf{r}'),$$

or

$$\frac{\partial\mathbf{B}(\mathrm{t},\mathbf{r})}{\partial\mathrm{t}}=\frac{\partial\mathbf{B}'(\mathrm{t}',\mathbf{r}')}{\partial\mathrm{t}'}-\mathbf{V}\cdot\nabla\mathbf{B}(\mathrm{t},\mathbf{r}). \tag{14}$$

Which is the same formula as given by Song and Russell (1999) and Shi et al. (2006).

In the proper reference frame of the magnetic structure, $\frac{\partial\mathbf{B}'(\mathrm{t}',\mathbf{r}')}{\partial\mathrm{t}'}=0$, thus

$$\frac{\partial\mathbf{B}(\mathrm{t},\mathbf{r})}{\partial\mathrm{t}}=-\mathbf{V}(\mathrm{t},\mathbf{r})\cdot\nabla\mathbf{B}(\mathrm{t},\mathbf{r}). \tag{15}$$

At the barycenter of the S/C constellation,

$$\frac{\partial\mathbf{B}(\mathrm{t},\mathbf{r}_c)}{\partial\mathrm{t}}=-\mathbf{V}(\mathrm{t},\mathbf{r}_c)\cdot\nabla\mathbf{B}(\mathrm{t},\mathbf{r}_c)\quad. \tag{16}$$

The component form of the above formula is

$$\frac{\partial\mathrm{B}_j(\mathrm{t},\mathbf{r}_c)}{\partial\mathrm{t}}=-\mathrm{V}_i(\mathrm{t},\mathbf{r}_c)\cdot\nabla_i\mathrm{B}_j(\mathrm{t},\mathbf{r}_c)\quad. \tag{16'}$$

The above equation has a unique solution of the apparent velocity and a proper reference frame can be found only if $\left|\nabla\mathbf{B}(\mathrm{t},\mathbf{r})\right| \neq 0$. Thus the apparent velocity of the magnetic structure relative to the S/C constellation is (Shi et al., 2006; Hamrin et al., 2008)

$$\mathrm{V}_{\mathrm{i}}(\mathrm{t},\mathbf{r}_{\mathrm{c}}) = -\mathrm{V}_{\mathrm{i}}'(\mathrm{t},\mathbf{r}_{\mathrm{c}}) = -\partial_{\mathrm{t}}\mathrm{B}_{\mathrm{j}}(\mathrm{t},\mathbf{r}_{\mathrm{c}})\cdot(\nabla\mathbf{B})^{-1}_{\mathrm{ji}}(\mathrm{t},\mathbf{r}_{\mathrm{c}}). \quad (17)$$

It is noted that the apparent velocity of the magnetic structure can vary with time. The formula (17) is applicable for magnetic structures with $\mathrm{V} << \mathrm{c}$, whether steady or unsteady. $\mathbf{V}/\mathrm{V}$ is a characteristic, directional vector, so that we can define $-\mathbf{V}/\mathrm{V}$ as the directional vector of the x_3 axis in the S/C constellation reference frame, i.e., $\hat{\mathbf{x}}_3 = -\mathbf{V}/\mathrm{V}$.

We can further investigate the transformation between the time derivatives of the magnetic gradients in the two different reference frames. Similarly to the linear magnetic gradients in the formula (13), the quadratic magnetic gradients in the S/C constellation frame and the proper frame of the magnetic structure are identical, i.e.,

$$\nabla\nabla\mathbf{B}(\mathrm{t},\mathbf{r}) = \nabla'\nabla'\mathbf{B}'(\mathrm{t}',\mathbf{r}'). \quad (18)$$

The relationship between the time derivative of the magnetic gradient in the S/C constellation frame, $\partial_{\mathrm{t}}\nabla\mathbf{B}(\mathrm{t},\mathbf{r})$, and the time derivative of the magnetic gradient in the proper frame of the magnetic structure, $\partial_{\mathrm{t}'}\nabla'\mathbf{B}'(\mathrm{t}',\mathbf{r}')$, satisfies

$$\begin{aligned}\frac{\partial}{\partial \mathrm{t}}\nabla\mathbf{B}(\mathrm{t},\mathbf{r}) &= \frac{\partial}{\partial \mathrm{t}}\nabla'\mathbf{B}'(\mathrm{t}',\mathbf{r}') \\ &= \frac{\partial \mathrm{t}'}{\partial \mathrm{t}}\frac{\partial}{\partial \mathrm{t}'}\nabla'\mathbf{B}'(\mathrm{t}',\mathbf{r}') + \frac{\partial \mathbf{r}'}{\partial \mathrm{t}}\cdot\nabla'\nabla'\mathbf{B}'(\mathrm{t}',\mathbf{r}') \\ &= \nabla'\frac{\partial}{\partial \mathrm{t}'}\mathbf{B}'(\mathrm{t}',\mathbf{r}') - \mathbf{V}\cdot\nabla'\nabla'\mathbf{B}'(\mathrm{t}',\mathbf{r}'). \quad (19)\end{aligned}$$

Considering $\dfrac{\partial\mathbf{B}'(\mathrm{t}',\mathbf{r}')}{\partial \mathrm{t}'} = 0$ in the proper reference frame and the equation (18), this reduces to

$$\frac{\partial}{\partial \mathrm{t}} \nabla \mathbf{B}(\mathrm{t}, \mathbf{r}) = -\mathbf{V} \cdot \nabla \nabla \mathbf{B}(\mathrm{t}, \mathbf{r}), \tag{20}$$

which is the formula relating the time derivative of the linear magnetic gradient to the quadratic magnetic gradient in the S/C constellation reference frame. With this general formula the gradient of the linear magnetic gradient in the direction of apparent velocity is readily obtained as shown below in **(iv)**.

(iv) The longitudinal gradient of $\nabla \mathbf{B}(\mathrm{t}, \mathbf{r}_{\mathrm{c}})$

Based on Equation (20), the gradient of the linear magnetic gradient along the x_3 direction at the barycenter $\mathbf{r}_{\mathrm{c}}$ satisfies

$$\mathrm{V} \frac{\partial}{\partial x^3} \nabla \mathbf{B}(\mathrm{t}, \mathbf{r}_{\mathrm{c}}) = \partial_{\mathrm{t}} \nabla \mathbf{B}(\mathrm{t}, \mathbf{r}_{\mathrm{c}}), \tag{21}$$

or

$$\partial_3 \partial_{\mathrm{k}} \mathrm{B}_{\mathrm{m}}(\mathrm{t}, \mathbf{r}_{\mathrm{c}}) = \frac{1}{\mathrm{V}} \partial_{\mathrm{t}} \partial_{\mathrm{k}} \mathrm{B}_{\mathrm{m}}(\mathrm{t}, \mathbf{r}_{\mathrm{c}}). \tag{22}$$

The right hand side of the above equation can be obtained from Equation (12), so that 9 components of the quadratic magnetic gradient can be obtained. Formula (22) is applicable for both steady and unsteady magnetic structures.

Furthermore, due to the symmetry of the quadratic gradient,

$$\nabla_{\mathrm{p}} \nabla_3 \mathrm{B}_{\mathrm{l}} = \nabla_3 \nabla_{\mathrm{p}} \mathrm{B}_{\mathrm{l}}, \tag{23}$$

of which the right hand side is given by Equation (20), so that 6 more components of the quadratic magnetic gradient can be obtained. Now only $\nabla_{\mathrm{p}} \nabla_{\mathrm{q}} \mathrm{B}_{\mathrm{l}} (\mathrm{p}, \mathrm{q} = 1, 2,\ \mathrm{l} = 1, 2, 3)$ are to be found, which involve $4 \times 3 = 12$ components. Considering the symmetry of the quadratic magnetic gradient, $\nabla_{\mathrm{p}} \nabla_{\mathrm{q}} \mathrm{B}_{\mathrm{l}} = \nabla_{\mathrm{q}} \nabla_{\mathrm{p}} \mathrm{B}_{\mathrm{l}}$, only $3 \times 3 = 9$ of these components are independent.

The gradient of the current density will be needed for the estimation of the remaining components of the quadratic magnetic gradient.

(v) Three components and two constraints for the quadratic magnetic gradient using the gradient of current density

From Ampere's law, we get the constraints that

$$\nabla\left(\nabla\times\mathbf{B}\right)=\nabla\mathbf{j},$$

with which we can obtain some components of the quadratic magnetic gradient if $\nabla\mathbf{j}$ is known (for simplicity, we replace $\mu_0\mathbf{j}$ by $\mathbf{j}$.). If the electromagnetic fields are strongly varying, $\mathbf{j}=\nabla\times\mathbf{B}-c^{-2}\partial\mathbf{E}/\partial t$, with the electric displacement current included. However, in this investigation we only consider the slow-varying electromagnetic fields with the limitation $\left|\nabla\times\mathbf{B}\right|>>c^{-2}\left|\partial\mathbf{E}/\partial t\right|$, which is commonly satisfied in large scale space plasmas. The component equation $\partial_3\left(\nabla\times\mathbf{B}\right)=\partial_3\mathbf{j}$ is not an independent constraint due to Eq. (22). It is a surplus condition, which we have not used because Eq. (22) can yield the longitudinal gradient directly already. Furthermore, $\nabla\cdot\mathbf{j}=\nabla\cdot\left(\nabla\times\mathbf{B}\right)=0$, so that the gradient of the current density only provides 9-3-1=5 independent constraints.

The transverse quadratic gradient of the longitudinal magnetic field, i.e., the quadratic gradient of the magnetic component B_3 in the plane orthogonal to the direction of motion (or x_3 direction) satisfies

$$\partial_p\partial_q B_3=\partial_p\left(\partial_{[q}B_{3]}+\partial_3 B_q\right)=\partial_p\left(\varepsilon_{lq3}j_l+\partial_3 B_q\right), \tag{24}$$

Where again Ampere's law $\nabla \times \mathbf{B} = \mathbf{j}$ has been used. Thus, Equation (24) leads to

$$\partial_p \partial_q B_3 (t, \mathbf{r}_c) = \varepsilon_{lq3} \partial_p j_l (t, \mathbf{r}_c) + \partial_3 \partial_p B_q (t, \mathbf{r}_c), \tag{25}$$

where $\partial_p j_q$ is used. The above formula yields the transverse quadratic magnetic gradient of the longitudinal magnetic field and contains 3 independent components of the quadratic magnetic gradient at the barycenter.

There are still 6 components of the quadratic magnetic gradient remaining to be determined, i.e., $\partial_p \partial_q B_s (t, \mathbf{r}_c)$, which are the transverse quadratic gradients of the transverse magnetic field.

Two additional constraints can be obtained from

$\partial_p j_3 = \partial_p (\partial_1 B_2 - \partial_2 B_1)$, $(p, q = 1, 2)$, i.e.,

$$\begin{cases} \partial_1 \partial_1 B_2 - \partial_1 \partial_2 B_1 = \partial_1 j_3 & (26) \\ \partial_2 \partial_1 B_2 - \partial_2 \partial_2 B_1 = \partial_2 j_3 & (27) \end{cases}$$

which is at the barycenter.

Based on Ampere's law, therefore, 3 more components of the quadratic magnetic gradient and 2 constraints on it can be obtained with the gradient of current density as shown in the formulas (25), (26) and (27).

Now 4 constraints are to be found for the complete determination of the quadratic magnetic gradient.

(xi) The last four constraints

The magnetic field is divergence-free, i.e., $\nabla \cdot \mathbf{B} = 0$. Therefore

$$\partial_j \partial_k B_k = 0. \tag{28}$$

It is noted that the sum over k is made in the above formula. Because $\partial_3\partial_k B_k = 0$ is a dependent constraint in Equation (22), there are only two independent constraints, i.e., $\partial_p\partial_k B_k = 0, (p, q = 1, 2)$. So that

$$\partial_1\partial_1 B_1 + \partial_1\partial_2 B_2 = -\partial_1\partial_3 B_3, \qquad (29)$$

$$\partial_2\partial_1 B_1 + \partial_2\partial_2 B_2 = -\partial_2\partial_3 B_3, \qquad (30)$$

where $\partial_p\partial_3 B_3 = \partial_3\partial_p B_3 = \frac{1}{V}\partial_p\partial_t B_3$ according to Eq. (22).

There are therefore only two constraints left to be found.

Using magnetic rotation analysis (MRA) [Shen et al., 2007, see also Appendix B], the remaining two constraints can be obtained from the properties of the magnetic field. As shown in Appendix B, based on MRA, the magnetic rotation tensor has three characteristic directions ($\hat{\mathbf{X}}_1$, $\hat{\mathbf{X}}_2$, $\hat{\mathbf{X}}_3$), as illustrated here in Figure 2. The coordinate line X_3 is along $\hat{\mathbf{X}}_3$. In the third characteristic direction $\hat{\mathbf{X}}_3$, the magnetic unit vector $\hat{\mathbf{b}} = \mathbf{B}/B$ has no rotation, and the square of the magnetic rotation rate is

$$\frac{\partial\hat{\mathbf{b}}}{\partial X_3}\cdot\frac{\partial\hat{\mathbf{b}}}{\partial X_3} = 0 \quad . \qquad (31)$$

So that

$$\frac{\partial\hat{\mathbf{b}}}{\partial X_3} = 0 \quad . \qquad (32)$$

Since $\frac{\partial\hat{\mathbf{b}}}{\partial X_3} = 0$ at each point of the coordinate line X_3 (as indicated in Figure 2), we have

$$\frac{\partial}{\partial X_3}\frac{\partial\hat{\mathbf{b}}}{\partial X_3} = 0. \qquad (33)$$

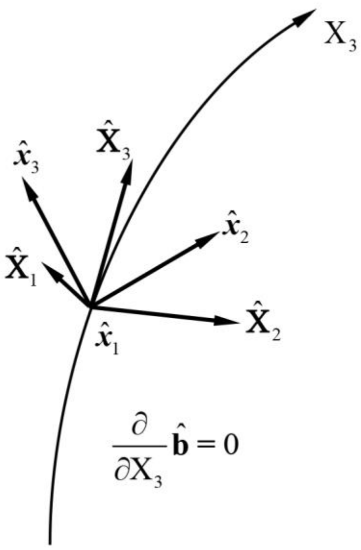

Figure 2. Illustration of the characteristic direction at which the magnetic rotation minimizes.

Since the magnetic unit vector $\hat{\mathbf{b}}$ obeys $\hat{\mathbf{b}} \cdot \hat{\mathbf{b}} = 1$, the above constraint contains only two independent component equations, which can be chosen as

$$\frac{\partial}{\partial \mathrm{X}_3}\frac{\partial}{\partial \mathrm{X}_3}\frac{\mathrm{B}_\mathrm{p}}{\mathrm{B}} = 0,\ \mathrm{p}=1,\ 2\,. \qquad (34)$$

The three characteristic directions ($\hat{\mathbf{X}}_1$, $\hat{\mathbf{X}}_2$, $\hat{\mathbf{X}}_3$) have a relationship with the base vectors（$\hat{\mathbf{x}}_1$, $\hat{\mathbf{x}}_2$, $\hat{\mathbf{x}}_3$） of the S/C coordinates (x_1, x_2, x_3), as follows:

$$\hat{\mathbf{X}}_\mathrm{i} = a_\mathrm{ij}\hat{\mathbf{x}}_\mathrm{j}\,, \qquad (35)$$

where the coefficients $a_\mathrm{ij} = \hat{\mathbf{X}}_\mathrm{i} \cdot \hat{\mathbf{x}}_\mathrm{j} = \cos\left[\angle\left(\hat{\mathbf{X}}_\mathrm{i}, \hat{\mathbf{x}}_\mathrm{j}\right)\right]$. If we assume a vector $\mathbf{X} = x_\mathrm{i}\hat{\mathbf{x}}_\mathrm{i} = \mathrm{X}_\mathrm{j}\hat{\mathbf{X}}_\mathrm{j}$, then $x_\mathrm{i} = \mathrm{X}_\mathrm{j}\hat{\mathbf{X}}_\mathrm{j} \cdot \hat{\mathbf{x}}_\mathrm{i} = a_\mathrm{ji}\mathrm{X}_\mathrm{j}$.

The first order partial derivative obeys:

$$\frac{\partial}{\partial \mathrm{X}_3} = \frac{\partial}{\partial x_\mathrm{k}} \cdot \frac{\partial x_\mathrm{k}}{\partial \mathrm{X}_3} = a_{3\mathrm{k}}\frac{\partial}{\partial x_\mathrm{k}} \quad ,$$

and he second order partial derivative obeys:

$$\frac{\partial}{\partial \mathrm{X}_3}\frac{\partial}{\partial \mathrm{X}_3}=a_{3\mathrm{k}}\frac{\partial}{\partial x_\mathrm{k}}\left(a_{3\mathrm{j}}\frac{\partial}{\partial x_\mathrm{j}}\right)=a_{3\mathrm{k}}a_{3\mathrm{j}}\frac{\partial}{\partial x_\mathrm{k}}\frac{\partial}{\partial x_\mathrm{j}}\,.$$

Generally, $\hat{\mathbf{X}}_3$ is varying slowly in space and $\frac{\partial}{\partial x_\mathrm{k}}a_{3\mathrm{j}}$ is a small quantity, thus $\frac{\partial}{\partial x_\mathrm{k}}a_{3\mathrm{j}}$ is omitted in the above equations. Therefore, Equation (34) reduces to

$$a_{3\mathrm{k}}a_{3\mathrm{j}}\frac{\partial}{\partial x^\mathrm{k}}\frac{\partial}{\partial x^\mathrm{j}}\left(\frac{\mathrm{B_p}}{\mathrm{B}}\right)=0,\ \mathrm{p}=1,\,2\,. \tag{36}$$

Finally, we show below that we can find $\partial_\mathrm{p}\partial_\mathrm{q}\mathrm{B_s}\left(\mathrm{t},\mathbf{r}_\mathrm{c}\right)$ by combining the equations (26), (27), (29), (30) and (36).

We also can investigate the formula (36) in more detail. For simplicity, we can adjust the coordinates $\left(x_1,\ x_2,\ x_3\right)$. We keep the x_3 axis unchanged with its basis $\hat{\mathbf{x}}_3=\text{-}\mathbf{V}/\mathrm{V}$, and rotate x_1 and x_2 axes around the x_3 axis such that the coordinate base vector $\hat{\mathbf{x}}_1$ is orthogonal to both $\hat{\mathbf{x}}_3$ and $\hat{\mathbf{X}}_3$, i.e.,

$$\hat{\mathbf{x}}_1=\frac{\hat{\mathbf{X}}_3\times\hat{\mathbf{x}}_3}{\left|\hat{\mathbf{X}}_3\times\hat{\mathbf{x}}_3\right|}, \tag{37}$$

(and as illustrated in Figure 2). Thus

$$a_{31}=\hat{\mathbf{X}}_3\cdot\hat{\mathbf{x}}_1=0\,.$$

Then the formula (36) becomes

$$a_{32}^2\frac{\partial^2}{\partial x_2^2}\left(\frac{\mathrm{B_p}}{\mathrm{B}}\right)=-a_{33}^2\frac{\partial^2}{\partial x_3^2}\left(\frac{\mathrm{B_p}}{\mathrm{B}}\right)-2a_{33}a_{32}\frac{\partial}{\partial x_3}\frac{\partial}{\partial x_2}\left(\frac{\mathrm{B_p}}{\mathrm{B}}\right). \tag{38}$$

All the terms in the right hand side of the above equation are known. With the formula (59) developed in the next section, we can express the second order gradients of the components of the magnetic unit vector on the two sides of Eq. (38) in terms of the magnetic gradients. With the formula (59), we get

$$\frac{\partial}{\partial x_2}\frac{\partial}{\partial x_2}\left(\frac{\mathrm{B_p}}{\mathrm{B}}\right)=\mathrm{B}^{-1}\partial_2\partial_2\mathrm{B_p}-\mathrm{B}^{-3}\mathrm{B_p}\mathrm{B_i}\partial_2\partial_2\mathrm{B_i}\text{-}2\mathrm{B}^{-2}\partial_2\mathrm{B_p}\partial_2\mathrm{B}+3\mathrm{B}^{-3}\mathrm{B_p}\partial_2\mathrm{B}\partial_2\mathrm{B}-\mathrm{B}^{-3}\mathrm{B_p}\partial_2\mathrm{B_i}\partial_2\mathrm{B_i}$$

$$, \qquad (39)$$

or

$$\begin{aligned}\partial_2\partial_2\left(\frac{\mathrm{B_p}}{\mathrm{B}}\right)&=\left(\mathrm{B}^{-1}\partial_2\partial_2\mathrm{B_p}-\mathrm{B}^{-3}\mathrm{B_p}\mathrm{B_s}\partial_2\partial_2\mathrm{B_s}\right)\\&+\left(-\mathrm{B}^{-3}\mathrm{B_p}\mathrm{B_3}\partial_2\partial_2\mathrm{B_3}\text{-}2\mathrm{B}^{-2}\partial_2\mathrm{B_p}\partial_2\mathrm{B}+3\mathrm{B}^{-3}\mathrm{B_p}\partial_2\mathrm{B}\partial_2\mathrm{B}-\mathrm{B}^{-3}\mathrm{B_p}\partial_2\mathrm{B_i}\partial_2\mathrm{B_i}\right)\end{aligned} \quad . \qquad (39')$$

The second expression on the right hand side is known already. Substituting (39') into (38), we get

$$\begin{aligned}\mathrm{B}^{-1}\partial_2\partial_2\mathrm{B_p}-\sum_{s=1}^{2}\mathrm{B}^{-3}\mathrm{B_p}\mathrm{B_s}\partial_2\partial_2\mathrm{B_s}&=-\frac{a_{33}^2}{a_{32}^2}\frac{\partial^2}{\partial x_3^2}\left(\frac{\mathrm{B_p}}{\mathrm{B}}\right)-\frac{2a_{33}}{a_{32}}\partial_3\partial_2\frac{\mathrm{B_p}}{\mathrm{B}}\\&-\left[-\mathrm{B}^{-3}\mathrm{B_p}\mathrm{B_3}\partial_2\partial_2\mathrm{B_3}\text{-}2\mathrm{B}^{-2}\partial_2\mathrm{B_p}\partial_2\mathrm{B}+3\mathrm{B}^{-3}\mathrm{B_p}\partial_2\mathrm{B}\partial_2\mathrm{B}-\mathrm{B}^{-3}\mathrm{B_p}\partial_2\mathrm{B_i}\partial_2\mathrm{B_i}\right]\end{aligned}$$

$$(40)$$

where p=1, 2. All the terms in the right hand side of the above equation can be determined with (59), (8), (22), (23) and (24).

Therefore, combining equations (26), (27), (29), (30) and (40), we can determine $\partial_\mathrm{p}\partial_\mathrm{q}\mathrm{B_s}\left(\mathrm{t},\mathbf{r}_\mathrm{c}\right)$.

Actually, with the two equations in the formula (40), we can completely find the solution $\partial_2\partial_2\mathrm{B_s}\left(\mathrm{t},\mathbf{r}_\mathrm{c}\right)$,（s=1, 2）.

Furthermore, with the formulas (30) and (27), we can get $\partial_1\partial_2\mathrm{B_s}\left(\mathrm{t},\mathbf{r}_\mathrm{c}\right)$,（s=1, 2）,

i.e.,

$$\partial_1\partial_2\mathrm{B_1}=\partial_2\partial_1\mathrm{B_1}=-\partial_2\partial_2\mathrm{B_2}-\partial_2\partial_3\mathrm{B_3} \quad , \qquad (41)$$

and

$$\partial_1\partial_2 B_2 = \partial_2\partial_1 B_2 = \partial_2\partial_2 B_1 + \partial_2 j_3 . \qquad (42)$$

The above two equations are valid at the barycenter.

In addition, from the equation (29) and (26), we can obtain $\partial_1\partial_1 B_s\left(t, \mathbf{r}_c\right)$,（s=1, 2）, i.e.,

$$\partial_1\partial_1 B_1 = -\partial_1\partial_2 B_2 - \partial_1\partial_3 B_3 , \qquad (43)$$

and

$$\partial_1\partial_1 B_2 = \partial_1\partial_2 B_1 + \partial_1 j_3 . \qquad (44)$$

The above two equations are also valid at the barycenter.

So far, we have obtained all the components of the quadratic gradient $\left(\nabla\nabla\mathbf{B}\right)_c$ at the barycenter. The accuracy of the quadratic gradient is to first order, just as that for the magnetic gradient.

(vii) Recalculating the magnetic gradients by iteration

In order to enhance the accuracy of the magnetic quantities, we can correct the estimate of the field and its linear gradient at the barycenter with the quadratic magnetic gradient obtained above (based on the formulae (A8) and (A13) in Appendix A). Subsequently, we can further go through the above steps（ii）-（vi）to get the corrected quadratic magnetic gradient with better accuracy.

The procedure is as follows:

The magnetic field measured by the four spacecraft is

$$B_i(t_a, \mathbf{r}_a) = B_i(t_c, \mathbf{r}_c) + \Delta x_a^{\nu} \nabla_{\nu} B_i(t_c, \mathbf{r}_c) + \frac{1}{2} \Delta x_a^{\nu} \Delta x_a^{\lambda} \nabla_{\nu} \nabla_{\lambda} B_i(t_c, \mathbf{r}_c) . \qquad (45)$$

Based on the formula (A8) in Appendix A, we obtain the magnetic field at the barycenter, corrected by the quadratic magnetic gradient, as:

$$\mathrm{B_i}(\mathrm{t_c},\mathbf{r}_\mathrm{c}) = \frac{1}{4\mathrm{n}}\sum_{\mathrm{a}=1}^{4\mathrm{n}}\mathrm{B_i}\left(\mathrm{t_a},\mathbf{r}_\mathrm{a}\right) - \frac{1}{2}\mathrm{R}^{\nu\lambda}\nabla_\nu\nabla_\lambda\mathrm{B_i}(\mathrm{t_c},\mathbf{r}_\mathrm{c}), \tag{46}$$

where, the general volume tensor $\mathrm{R}^{\nu\lambda}$ is as defined in (A9).

From the formula (A13) in Appendix A, we get the first order magnetic gradient at the barycenter corrected from the quadratic magnetic gradient as

$$\nabla_\nu B_i(\mathrm{t_c},\mathbf{r}_\mathrm{c}) = \left(\mathbf{R}^{-1}\right)_{\nu\mu}\cdot\frac{1}{\mathrm{N}}\sum_{a}^{\mathrm{N}}\left(x^\mu_{(a)} - x^\mu_\mathrm{c}\right)B_i\left(\mathrm{t_a},\mathbf{r}_\mathrm{a}\right) - \frac{1}{2}\left(\mathbf{R}^{-1}\right)_{\nu\mu}\mathrm{R}^{\mu\sigma\lambda}\nabla_\sigma\nabla_\lambda\mathrm{B_i}(\mathrm{t_c},\mathbf{r}_\mathrm{c}).$$

(47)

Furthermore, we can perform the above steps（ii）-（vi）to obtain the corrected quadratic magnetic gradient using these updated estimates. The quadratic magnetic gradient obtained in this iterative sense has a higher accuracy, while errors in the magnetic field, its linear gradient and the apparent velocity of the magnetic structure at the barycenter, are of second order in L/D, where L is the size of the S/C constellation and D is the characteristic scale of the magnetic structure.

To summarise this algorithm, we proceed as follows

(a) Estimate the magnetic field $\mathbf{B}_\mathrm{c}$; the first order magnetic gradient $\left(\nabla\mathbf{B}\right)_\mathrm{c}$, and the time variation rate $\left(\frac{\partial\mathbf{B}}{\partial \mathrm{t}}\right)_\mathrm{c}$ of the magnetic field, at the barycenter and under the linear approximation; as in Eqs. (7) and (8).

Estimate the gradient of the current density at the barycenter $\nabla\mathbf{j}\left(\mathrm{t},\mathbf{r}_\mathrm{c}\right)$, as in Eq. (10).

(b) Determine the apparent velocity $\mathbf{V}$ using the time variation rate $\left(\frac{\partial \mathbf{B}}{\partial \mathrm{t}}\right)_{\mathrm{c}}$ of the magnetic field and the first order magnetic gradient $(\nabla \mathbf{B})_{\mathrm{c}}$ and define the x_3 coordinate with $\hat{\mathbf{x}}_3 = -\mathbf{V}/\mathrm{V}$; determine the three characteristic directions ($\hat{\mathbf{X}}_1$, $\hat{\mathbf{X}}_2$, $\hat{\mathbf{X}}_3$) using MRA, and define the coordinate base vector $\hat{\mathbf{x}}_1 = \frac{\hat{\mathbf{X}}_3 \times \hat{\mathbf{x}}_3}{\left|\hat{\mathbf{X}}_3 \times \hat{\mathbf{x}}_3\right|}$, such as to fix the Cartesian coordinates (x_1, x_2, x_3) in the spacecraft constellation reference frame.

(c) Calculate the time variation rate $\frac{\partial}{\partial \mathrm{t}}(\nabla \mathbf{B})_{\mathrm{c}}$ of the linear magnetic gradient at the barycenter, so as to obtain the components of the quadratic magnetic gradient $(\nabla_3 \nabla \mathbf{B})_{\mathrm{c}}$ and $(\nabla \nabla_3 \mathbf{B})_{\mathrm{c}}$, as in Eqs. (22) and (23).

(d) Combine Ampere's law and the first order gradient of the current density $\nabla \mathbf{j}(\mathrm{t}, \mathbf{r}_{\mathrm{c}})$ to calculate the transverse quadratic magnetic gradient of B_3, i.e. $\nabla_{\mathrm{p}} \nabla_{\mathrm{q}} \mathrm{B}_3 (\mathrm{p}, \mathrm{q} = 1, 2)$, as in Eq. (25).

(e) Solve the equations $\frac{\partial}{\partial \mathrm{X}_3} \frac{\partial}{\partial \mathrm{X}_3} \hat{\mathbf{b}} = 0$, derived by MRA, so as to obtain the components: $\partial_2 \partial_2 \mathrm{B}_{\mathrm{p}} (\mathrm{p} = 1, 2)$.

(f) Determine the remaining four components of the quadratic magnetic gradient, $\left(\partial_1 \partial_2 \mathrm{B}_{\mathrm{p}}\right)_{\mathrm{c}} = \left(\partial_2 \partial_1 \mathrm{B}_{\mathrm{p}}\right)_{\mathrm{c}}$ and $\left(\partial_1 \partial_1 \mathrm{B}_{\mathrm{p}}\right)_{\mathrm{c}}, (\mathrm{p} = 1, 2)$, using the equation $\nabla(\nabla \cdot \mathbf{B}) = 0$ derived from the divergence free condition of the magnetic field and the equation $\nabla(\nabla \times \mathbf{B}) = \nabla \mathbf{j}$ from Ampere's law, as in Eqs. (41) - (44).

(g) Revise the magnetic field $\mathbf{B}_{\mathrm{c}}$ and the first order magnetic gradient $(\nabla \mathbf{B})_{\mathrm{c}}$ with the quadratic magnetic gradient $\mathrm{G}^{(2)} = (\nabla \nabla \mathbf{B})_{\mathrm{c}}$ obtained initially, as in the formulas (46) and (47), and perform the above steps (b) - (f) once again, so as to get the corrected quadratic magnetic gradient $(\nabla\nabla\mathbf{B})_c$, as well as the corrected apparent velocity $\mathbf{V}$ of the magnetic structure.

It should be noted that, the magnetic field, the linear magnetic gradient and the quadratic magnetic gradient are all identical in different reference frames. We will test all these estimators in detail in Section 4.

Given the magnetic field $\mathbf{B}_c$, the first order magnetic gradient $(\nabla\mathbf{B})_c$ and the quadratic magnetic gradient $(\nabla\nabla\mathbf{B})_c$, the complete geometry of the magnetic field lines of the magnetic structure can be determined. We will find the estimators for the geometrical parameters of the MFLs in the next section.

3. Determining the complete geometry of magnetic field lines based on multiple S/C measurements

The geometry of the MFLs plays a critical role in the evolution of the space plasmas. In this section, we will extract the estimators for the complete geometry of the MFLs, from the linear and quadratic gradients of the magnetic field estimated in Section 2.

3.1 The natural coordinates and curvature of the MFLs

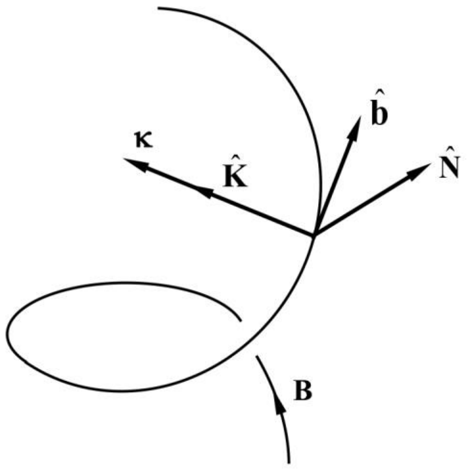

Figure 3. Demonstration on the geometry of the magnetic field lines. $\hat{\mathbf{b}} = \mathbf{B}/B$ is the magnetic unit vector; $\boldsymbol{\kappa}$ is the curvature vector of the magnetic field line, $\hat{\mathbf{K}}$ and $\hat{\mathbf{N}}$ are the principal normal and binormal, respectively. The magnetic field line is also twisting with torsion.

The directional magnetic unit vector is $\hat{\mathbf{b}} = \mathbf{B}/B$, which is also the tangential vector of the MFLs. The MFLs are usually turning, and the bending of MFLs is characterized by the curvature vector, i.e.,

$$\boldsymbol{\kappa} = \frac{\mathrm{d}\hat{\mathbf{b}}}{\mathrm{ds}} = \left(\hat{\mathbf{b}} \cdot \nabla\right)\hat{\mathbf{b}}, \tag{48}$$

where ‘s’ is the arc length along the MFLs.

Shen et al., (2003， 2011) first presented the estimator of the curvature of MFLs, which has found many applications in multi-point data analysis. Here a brief description of it is given and we will then investigate further the complete geometry of the MFLs as well as the explicit estimators.

The gradient of the magnetic field $(\nabla \mathbf{B})_c$ at the barycenter from multi-spacecraft measurements has already been expressed in Section 2.

The gradient of the magnetic strength B=|**B**| is

$$\nabla_i B = \frac{1}{2B} \nabla_i B^2 = \frac{1}{B} B_j \nabla_i B_j, \tag{49}$$

while at the barycenter of the S/C constellation,

$$(\nabla_i B)_c = B_c^{-1} B_{cj} (\nabla_i B_j)_c . \tag{50}$$

Similarly, the gradient of the unit magnetic vector $\hat{\mathbf{b}}$ is

$$\nabla_i b_j = \nabla_i \frac{B_j}{B} = B^{-1} \nabla_i B_j - B^{-2} B_j \nabla_i B. \tag{51}$$

With Eq (49), the above formula (51) becomes

$$\nabla_i b_j = B^{-1} \nabla_i B_j - B^{-1} b_j b_m \nabla_i B_m . \tag{52}$$

Hence, the gradient of the unit magnetic vector $\hat{\mathbf{b}}$ at the barycenter is

$$(\nabla_i b_j)_c = B^{-1} (\nabla_i B_j)_c - B^{-1} b_j b_m (\nabla_i B_m)_c . \tag{53}$$

All the coefficients on the right hand side of the above formula involve values at the barycenter (Shen, et al., 2003): $(B_i)_c = \frac{1}{N} \sum_{\alpha=1}^{N} B_{\alpha i}$, $(b_i)_c = B_{ci} / |\mathbf{B}_c|$. The formula (53) obeys the condition that: $b_j (\nabla_i b_j)_c = 0$, which is required by the constraint $\hat{\mathbf{b}} \cdot \hat{\mathbf{b}} = 1$.

The curvature of the MFLs at the barycenter is therefore

$$\kappa_{cj} = b_i (\nabla_i b_j)_c = B^{-1} b_i (\nabla_i B_j)_c - B^{-1} b_i b_j b_m (\nabla_i B_m)_c . \tag{54}$$

All the coefficients on the right hand side of the above formula involve values at the barycenter. The formula (54) is the estimator of the curvature of the MFLs based on the multi-S/C magnetic measurements. It is noted that there can be no field line crossing through the point where B=0; thus, there is no need to calculate the curvature from formula (54). It is noted that formula (54) satisfies $\hat{\mathbf{b}}_c \cdot \boldsymbol{\kappa}_c = b_{cj}\kappa_{cj} = 0$, indicating that the obtained curvature vector is orthogonal to the magnetic field.

The radius of the curvature of the MFLs is

$$R_c = 1/\kappa_c \,. \tag{55}$$

The principal normal vector of the MFLs is

$$\hat{\mathbf{K}} = \boldsymbol{\kappa}_c / |\boldsymbol{\kappa}_c| \,. \tag{56}$$

The binormal vector of the MFLs is

$$\hat{\mathbf{N}} = \hat{\mathbf{b}} \times \hat{\mathbf{K}} = \frac{\hat{\mathbf{b}} \times \boldsymbol{\kappa}_c}{\kappa_c} \,, \tag{57}$$

The above expressions collectively describe the estimators of the magnetic curvature analysis approach [Shen et al., 2003; 2011], where $\{\hat{\mathbf{b}}, \hat{\mathbf{K}}, \hat{\mathbf{N}}\}$ constitute the natural coordinates, or the Frenet frame (trihedron). The unit magnetic vector $\hat{\mathbf{b}}$, principal normal $\hat{\mathbf{K}}$ and binormal $\hat{\mathbf{N}}$ are orthogonal to each other.

Usually, the MFLs not only bend, but also twist, such as the helical MFLs manifested in a flux rope. The twist of the MFLs can be described quantitatively by the torsion. In order to get the complete geometry of the MFLs, therefore, the torsion should be known. The torsion of the MFLs is defined as

$$\tau \equiv \frac{1}{\kappa} \frac{d^2\hat{\mathbf{b}}}{ds^2} \cdot \hat{\mathbf{N}} = \frac{1}{\kappa} \frac{d\boldsymbol{\kappa}}{ds} \cdot \hat{\mathbf{N}} = -\frac{1}{\kappa} \boldsymbol{\kappa} \cdot \frac{d\hat{\mathbf{N}}}{ds} \,. \tag{58}$$

Therefore, the quadratic gradient of the magnetic field $\nabla\nabla\mathbf{B}$ is essential for the calculation of the torsion of the MFLs.

We now investigate the relationship between the torsion of the MFLs and the quadratic gradient of the unit magnetic vector $\nabla\nabla\hat{\mathbf{b}}$; as well as with the quadratic magnetic gradient $\nabla\nabla\mathbf{B}$.

To do this, we need to first deduce the expression of the quadratic gradient of the unit magnetic vector in terms of the linear and quadratic magnetic gradients.

The quadratic gradient of the unit magnetic vector $\hat{\mathbf{b}}$ is

$$\begin{aligned}
\nabla_k\nabla_i b_j &= \nabla_k\left(B^{-1}\nabla_i B_j - B^{-1}b_j b_l \nabla_i B_l\right)\\
&= \nabla_k B^{-1}\cdot\nabla_i B_j + B^{-1}\nabla_k\nabla_i B_j - \nabla_k\left(B^{-1}b_j b_l\right)\cdot\nabla_i B_l - B^{-1}b_j b_l \nabla_k\nabla_i B_l\\
&= -B^{-2}\nabla_k B\cdot\nabla_i B_j + B^{-1}\nabla_k\nabla_i B_j + B^{-2}\nabla_k B\cdot b_j b_l \nabla_i B_l\\
&\quad - B^{-1}b_l\nabla_k b_j\cdot\nabla_i B_l - B^{-1}b_j\nabla_k b_l\cdot\nabla_i B_l - B^{-1}b_j b_l\nabla_k\nabla_i B_l\\
&= -B^{-2}\nabla_k B\cdot\nabla_i B_j + B^{-1}\nabla_k\nabla_i B_j + 3B^{-2}b_j b_l\nabla_k B\nabla_i B_l\\
&\quad - B^{-2}b_l\nabla_k B_j\nabla_i B_l - B^{-2}b_j\nabla_k B_l\cdot\nabla_i B_l - B^{-1}b_j b_l\nabla_k\nabla_i B_l .
\end{aligned} \tag{59}$$

Thus the estimator of the quadratic gradient of $\hat{\mathbf{b}}$ at the barycenter is expressed as

$$\begin{aligned}
\left(\nabla_k\nabla_i b_j\right)_c &= -B^{-2}\left(\nabla_k B\right)_c\left(\nabla_i B_j\right)_c + 3B^{-2}b_j b_m\left(\nabla_k B\right)_c\left(\nabla_i B_m\right)_c - B^{-2}b_m\left(\nabla_k B_j\right)_c\left(\nabla_i B_m\right)_c\\
&\quad - B^{-2}b_j\left(\nabla_k B_m\right)_c\cdot\left(\nabla_i B_m\right)_c + B^{-1}\left(\nabla_k\nabla_i B_j\right)_c - B^{-1}b_j b_m\left(\nabla_k\nabla_i B_m\right)_c .
\end{aligned} \tag{60}$$

Based on this definition, the torsion of the MFLs is

$$\begin{aligned}
\tau &= \frac{1}{\kappa}\frac{d\boldsymbol{\kappa}}{ds}\cdot\hat{\mathbf{N}} = \frac{1}{\kappa}b_j\partial_j\left(b_k\partial_k b_i\right)N_i\\
&= \frac{1}{\kappa}\left(b_j\partial_j b_k\cdot\partial_k b_i + b_j b_k\partial_j\partial_k b_i\right)N_i .
\end{aligned} \tag{61}$$

So that the torsion of the MFLs at the barycenter of the S/C constellation is

$$\tau_c = \kappa^{-1}N_i\cdot\left[b_j\left(\partial_j b_k\right)_c\cdot\left(\partial_k b_i\right)_c + b_j b_k\left(\partial_j\partial_k b_i\right)_c\right] . \tag{62}$$

The above formula is one of the estimators of the torsion of the MFLs that is dependent on the linear and quadratic gradients of the unit magnetic vector $\hat{\mathbf{b}}$.

By substituting Eqs (52) and (59) into Eq (61), the torsion of the MFLs is obtained as

$$\tau = \kappa^{-1} B^{-3} N_j B_i \partial_i B_k \partial_k B_j + \kappa^{-1} B^{-3} N_j B_k B_i \partial_k \partial_i B_j , \qquad (63)$$

where the condition $b_j N_j = 0$ has been used. Appendix C presents another verification of the expression (63) for clarity. It seems that the formula (63) is invalid as B=0 or $\kappa = 0$. However, there is no field line as B=0, while for $\kappa = 0$, the field line is a straight line and its torsion has no fixed value, and thus is meaningless.

Therefore, the torsion of the MFLs at the barycenter can be written as

$$\tau_c = \kappa^{-1} B^{-3} N_j B_i \left(\partial_i B_k\right)_c \left(\partial_k B_j\right)_c + \kappa^{-1} B^{-3} N_j B_k B_i \left(\partial_k \partial_i B_j\right)_c . \qquad (64)$$

All the coefficients on the right hand side of the above formula involve values at the barycenter. Formula (64) is another estimator of the torsion of the MFLs, expressed in terms of the linear and quadratic gradients of the magnetic field. The two different estimators of the torsion of the MFLs (62) and (64) are obviously equivalent.

4. Tests

In this section, the estimators put forward in Sections 2 and 3 will be tested for model current sheets and flux ropes, which can occur in the magnetosphere, in order to verify the validity and accuracy of this approach. A one-dimensional Harris current sheet model (Harris, 1962) and a Lundquist-Lepping cylindrical force-free flux rope model (Lundquist, 1950) are used for these two typical structures, respectively. Appendices D and E present, analytically, the geometrical features of these two kinds of magnetic structures. The tests below have shown that the estimators of the quadratic magnetic gradients and the complete geometry of the MFLs are obtained with good accuracy compared to the models, so we expect they can find wide applications in investigating the magnetic structures and configurations in space plasmas with multi-S/C measurements.

4.1 The steps needed for this comparison

The operative calculating steps can be summarized as follows:

(a) Deriving the first-order gradients of **B** and **J**.

With four-point measurements, the temporal and spatial gradients of **the** magnetic field ($\nabla\mathbf{B}, \frac{\partial\mathbf{B}}{\partial t}$)and the current density ($\nabla\mathbf{J}, \frac{\partial\mathbf{J}}{\partial t}$) are readily deduced by the least-squares gradient calculation as outlined in Appendix A. The temporal variation $\frac{\partial\nabla\mathbf{B}}{\partial t}$ can also be inferred by differential calculations.

(b) Determining the velocity of the magnetic structures relative to the SCs.

Once the time series of $\nabla\mathbf{B}, \frac{\partial\mathbf{B}}{\partial t}$ are obtained, the velocity of the magnetic structures relative to the S/C constellation can be derived by Equation (15), $\frac{\partial\mathbf{B}}{\partial t} + \mathbf{V}\cdot\nabla\mathbf{B} = 0$. Therefore, the velocity of the spacecraft is $\mathbf{V}' = -\mathbf{V}$.

(c) Constructing the local coordinates $\{\hat{\mathbf{e}}_1, \hat{\mathbf{e}}_2, \hat{\mathbf{e}}_3\}$.

According to above statements, $\hat{\mathbf{e}}_3$ is defined as the direction of the relative velocity of the spacecraft to the magnetic structure, i.e., $\hat{\mathbf{e}}_3 = \mathbf{V}/|\mathbf{V}|$. We can then apply MRA analysis to derive the minimum rotation direction of the magnetic field ($\hat{\mathbf{X}}_3$) and the $\hat{\mathbf{e}}_1$ can be set as $\hat{\mathbf{e}}_1 = \hat{\mathbf{X}}_3 \times \hat{\mathbf{e}}_3$. Finally, $\hat{\mathbf{e}}_2$ completes the right-handed system.

(d) Deriving $\nabla\nabla\mathbf{B}$ and $\nabla\nabla\hat{\mathbf{b}}$ and calculating the torsion of MFLs.

After expressing these parameters ($\mathbf{B}$, $\nabla\mathbf{B}$, $\nabla\mathbf{J}$, $\frac{\partial\nabla\mathbf{B}}{\partial t}$ and $\mathbf{V}$) in the local coordinates, we then can derive the quadratic gradient of magnetic field and the magnetic unit vector, $\nabla\nabla\mathbf{B}$ and $\nabla\nabla\hat{\mathbf{b}}$ by following the steps stated in Section 2. Furthermore, the torsion of magnetic field line can be obtained by Equation (62) or (64).

(e) Performing iterative operations to obtain more accurate results.

The estimates of the magnetic field and the first-order gradient of magnetic field at the barycenter of the four S/C can be modified by Equation (45) and (47), in order to repeat the same procedure as in steps (a)-(d) above.

4.2 One-dimensional Harris Current Sheet

For the one-dimensional Harris current sheet, the magnetic field can be formulated as Equation (D1) in Appendix D. In this test, the parameters of the current sheet are B_0=50nT, B_y=10nT, B_z=20nT, h=R_E. As shown in Figure 4a, we set an arbitrary S/C constellation trajectory from (2, 2, 2) $\mathrm{R_E}$ to (-2, -2, -2) $\mathrm{R_E}$ during 100 seconds. The S/C constellation is assumed to be a regular tetrahedron with a separation of L=100 km. The analytic values of the magnetic field and the current density at the barycenter of the four S/Cs are shown in panels (b) and (c) in Figure 4, respectively.

In this test, we have set n=10, and make N=4n=40 points to calculate the spatial and temporal gradient of the magnetic field at the barycenter of the S/C constellation with the method in Appendix A. Therefore, we can get the spatial gradient of the vector field within the interval 5-95s. Furthermore, the temporal and spatial scale corresponds to the time resolution of the field sampling (i.e. T=1s) and the characteristic size of tetrahedron (L=100 km). The magnetic field and the non-zero component $\frac{\partial B_x}{\partial z}$ of the linear magnetic gradient at the barycenter are derived with the formulas (5) and (6) and shown in Figure 4b and 4d, respectively, which are in good agreement with their analytic values as given by Appendix A (the circles represent the results derived by the method, while the black solid line denotes the analytic results derived by theoretical formula). The current density at the barycenter can also be derived with $\frac{\partial B_x}{\partial z}$ by Ampere's law ($\mathbf{j} = \nabla \times \mathbf{B}$) and is shown in Figure 4c. Those values are again consistent with the analytic values. The apparent velocity of the current sheet relative to the S/C constellation can be derived by formula (15). As shown in Figure 4e, the velocity Vz of S/C relative to the current sheet is within the range 252~260 km/s (0.0408~0.0398 Re/s), while the actual velocity is 257 km/s (0.0404 Re/s). Thus, the maximum relative error of the deduced velocity is $\frac{0.0006}{0.0404} \approx 1.5\%$, which is approximately the order of L/h(~0.016).

With the derived linear magnetic gradient and current density gradient, the quadratic magnetic gradient of this current sheet model can be readily obtained. It should be noted that, among the components of the quadratic magnetic gradient, only $\frac{\partial^2 B_x}{\partial z^2}$ is non-zero, while $\frac{\partial^2 b_x}{\partial z^2}, \frac{\partial^2 b_y}{\partial z^2}, \frac{\partial^2 b_z}{\partial z^2}$ are non-zero among the components of the quadratic gradient of magnetic unit vectors. The test is therefore focused on these components. Evidently, from Figure 4(g-j), there is extremely good agreement between the results obtained by the technique and the analytic values. As illustrated in Figure 4 , $\frac{\partial^2 B_x}{\partial z^2}$ (Figure 4f) and $\frac{\partial^2 b_x}{\partial z^2}$ (Figure 4g) have bipolar signatures around the center of current sheet and are equal to zero at the center, while $\frac{\partial^2 b_y}{\partial z^2}$ (Figure 4h) and $\frac{\partial^2 b_z}{\partial z^2}$ (Figure 4i) show left-right symmetry around the current sheet center and reach a minimum at the center. These results are reasonable and in good agreement with the analytic results.

We have further obtained the geometry of the current sheet deduced by the method. The deduced curvature and torsion of the MFLs in the Harris current sheet are shown in Figure 4j and 4k. The magnetic curvature reaches a maximum at the center of current sheet, which indicates that the MFLs of the Harris current sheet bend most at the center. The torsion of the magnetic field line stays almost at zero, implying the MFLs in the Harris current sheet is planar (this agrees with the theoretical calculations in Appendix D). The order of the absolute error in the torsion is very small and less than 10^{-11} $R_E{}^{-1}$. This check is a very good validation of the new method.

After completing the above steps, iterative operation and error analysis are necessary and we will discuss these later.

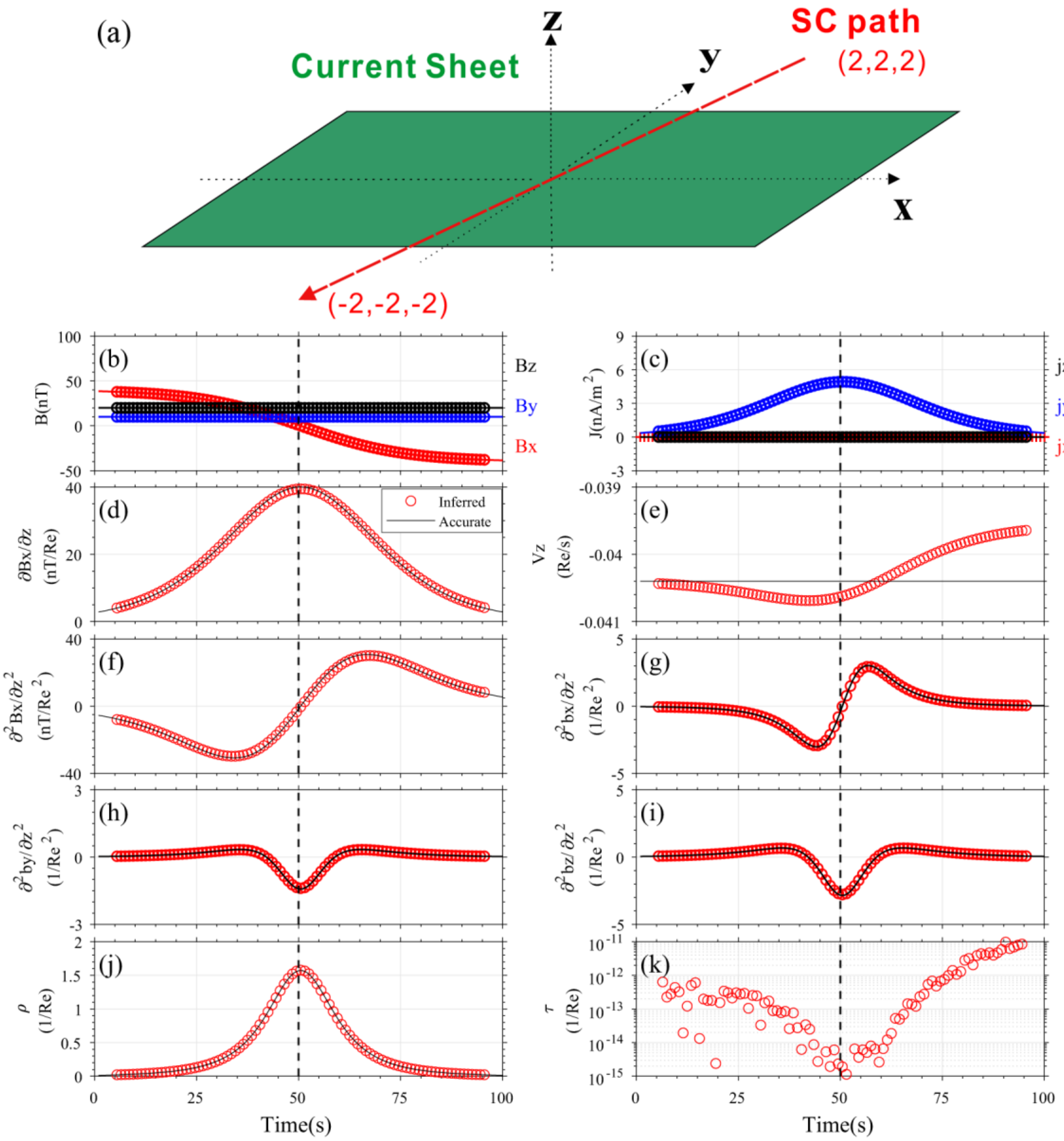

Figure 4: The comparison between the properties of 1-D Harris current sheet deduced form the estimators and those from the analytic calculations based on Appendix D. Panel (a) shows the current sheet configuration and the S/C trajectory in the current sheet reference frame; Panel (b), (c) show the variation of magnetic field and current density, respectively; Panel (d) is the time series of the gradient of magnetic field; Panel (e) denotes the relative velocity of S/Cs to the current sheet; Panel (f) represents the quadratic gradient of magnetic field; Panel (g), (h), (i) denote the time series of the quadratic gradient of unit magnetic vector bx, by, bz, respectively. The magnetic field

line curvature and torsion are displayed in Panel (j), (k), respectively. The vertical black dashed line in each panel represents the center of current sheet. The black solid lines in each panel are the accurate or theoretical results. The circles are the results obtained by the new method.

4.3 Two-dimensional Force-free Flux Ropes

In this section, we attempt to investigate the complete geometry of magnetic field lines for a classic force-free flux rope model. In this model, the three components of the magnetic vector in cylindrical coordinates can be expressed (Lundquist, 1950) as:

$$B_r = 0, B_\varphi = B_0 J_1(\alpha r), B_z = B_0 J_0(\alpha r), \tag{65}$$

where r is the distance from the central axis, α is the characteristic scale of the flux rope, and J is the Bessel function. In this test, we adopt $B_0 = 60\,\mathrm{nT}$, $\alpha = 1/\mathrm{R}_E$, The trajectory of the SC is set to be from (-2, 0, 0) $\mathrm{R_E}$ to (2, 0, 0) $\mathrm{R_E}$ during 100 seconds and is shown in Figure 5a. The average magnetic field measured by four S/C is illustrated in Figure 5b, the bipolar signature of By and the enhancement of Bz around the flux rope's center is apparent.

By repeating the same procedures as in Section 4.2, the quadratic magnetic gradient can be readily acquired (Figure 5c, 5d, 5e, 5f, 5g). One can find that the results derived by the method are in good agreement with the analytic results obtained in Appendix E. The variations of curvature and torsion of the MFLs confirm that the magnetic topological structure is different from those of the current sheet (Figure 5h, 5i). It can also be seen from Figure 5h and 5i that the curvature of the MFLs contains a minimum, and the torsion of the MFLs contains a maximum, at the center. This indicates that the straighter and more twisted the MFLs, the nearer to the center of flux rope, implying the non-planar and helical structure of the flux rope. This test shows that the results obtained by the approach are in good agreement with the analytical results, indicating that the estimators obtained in Sections 2 and 3 are reliable and applicable.

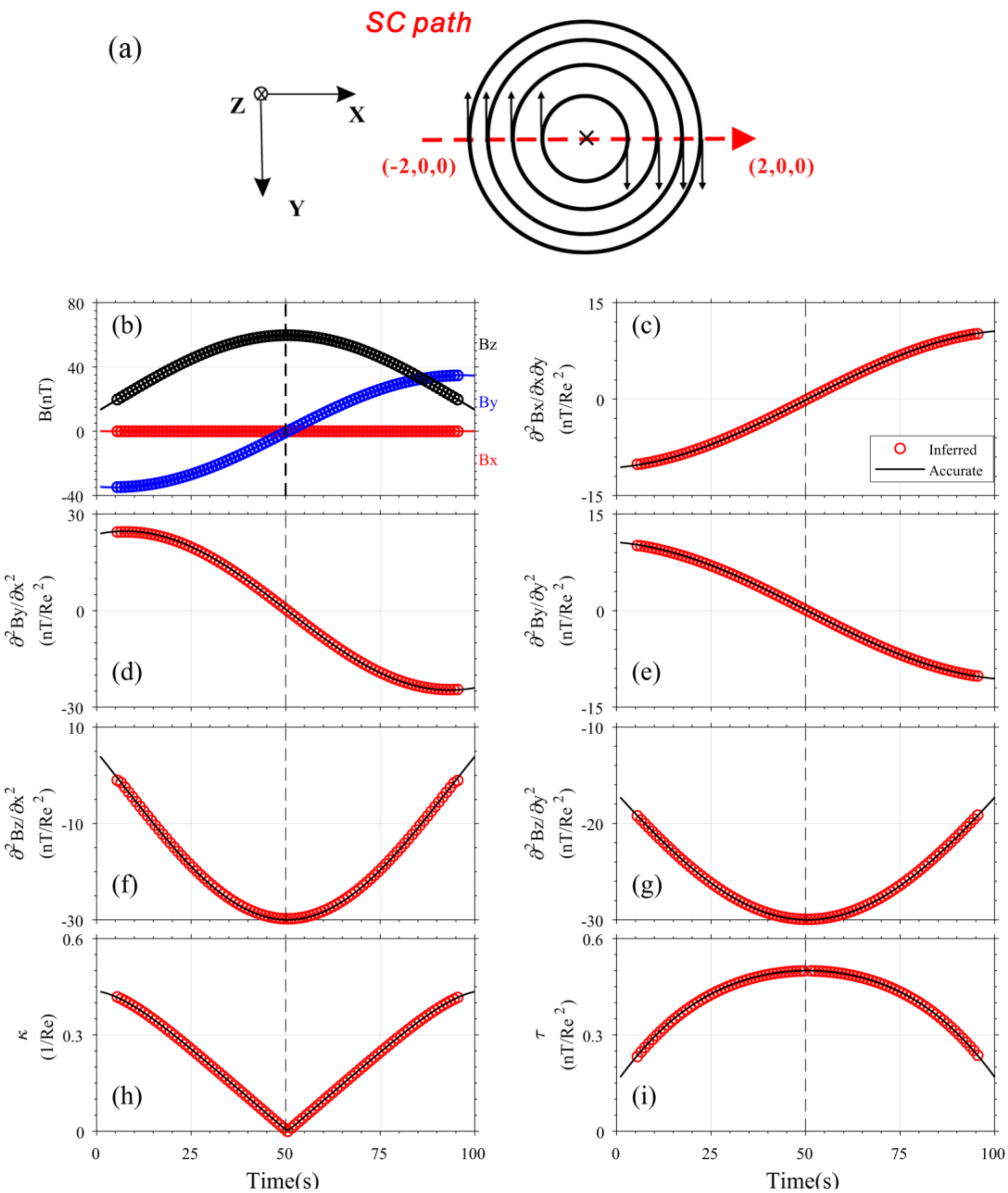

Figure 5: The properties of MFLs of 2-D flux rope. The relative path of S/Cs to the magnetic structure is sketched in Panel (a). Panel (b) shows the variation of the magnetic field; Panel (c), (d), (e), (f), (g) denote the time series of the quadratic gradient of magnetic field. The magnetic field line curvature and torsion are displayed in Panel (h) and (i). The vertical black dashed line in each panel represents the center

of flux rope. The circles and black solid lines represent the results inferred by our method and the accurate results, respectively.

4.4 Error Analysis

The errors of the estimators put forward in this study may arise from two types of sources: the underlying measurement errors and the truncation errors. The key measurement errors include the error in the measured magnetic field $\mathbf{B}$ and that of the current density $\mathbf{j}$ derived from the plasma moment data (which will be seen in the application in Section 5). The truncation errors arise from terms beyond the differential order considered here and represent neglected behaviour of the magnetic structure and plasmas.

The spatial truncation errors can be approximately measured by L/D, where D is the typical spatial size of magnetic structure and L is the size of tetrahedron of four SC. When L/D is very small, the truncation errors are generally small. However, as L/D grows large, the truncation errors may become significant. The iterative operation allows us to attempt to get more accurate and reliable results.

Figure 6 compares the results of the calculations made with no iteration; with the first and second iterations, and theoretical calculation with L/D=0.3. It can be seen that the iterations yield more accurate results. However, the second iteration in these examples did not produce better results than the first iteration.

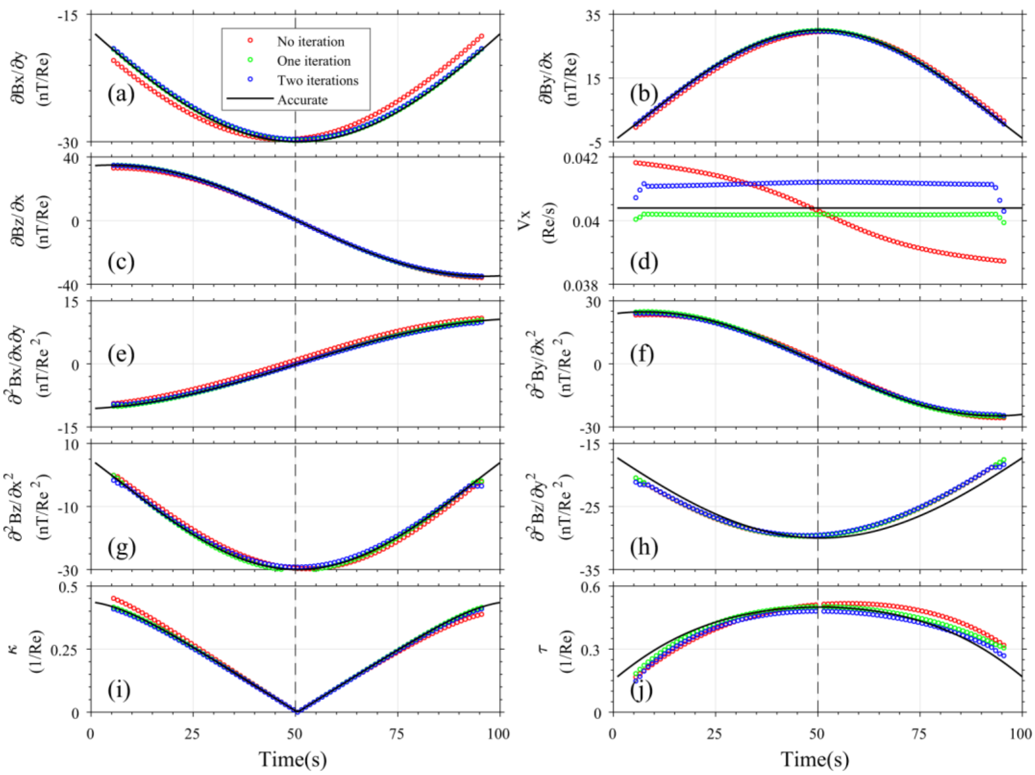

Figure 6: The comparison of those results with no iteration, first iteration and second iteration. The format of this figure is just the same as that of Figure 5. The red circles in each panel denote the result of no iteration, while the green and blue circles mark the result from the first iteration and second iteration, respectively. The black solid lines represent analytic results.

Figure 7 displays the variations of the relative errors of the results with L/D. The relative error is defined as $<|\frac{X_{method} - X_{real}}{X_{real}}|>$, where X_{method} represents the results obtained with our method and X_{real} denotes the analytical results from the model. It is seen from Figure 7(a), (b), (c), (d), (e) that the relative errors of the linear magnetic gradient, apparent velocity and curvature of the MFLs are of first order in L/D for no iteration calculations, but they are of second order in L/D after the first and second iterations. Nevertheless, the relative errors of the components of the quadratic magnetic gradient and the torsion of MFLs are all of first order in L/D (Figure 7f, g, h, I, j), although after the first or second iterations they are improved.

Through the above analysis, one can conclude that the most accurate results are those derived by at least one iteration, especially when L/D is larger than 0.5. Thus, it is necessary to perform the first iteration when L/D is larger than 0.5.

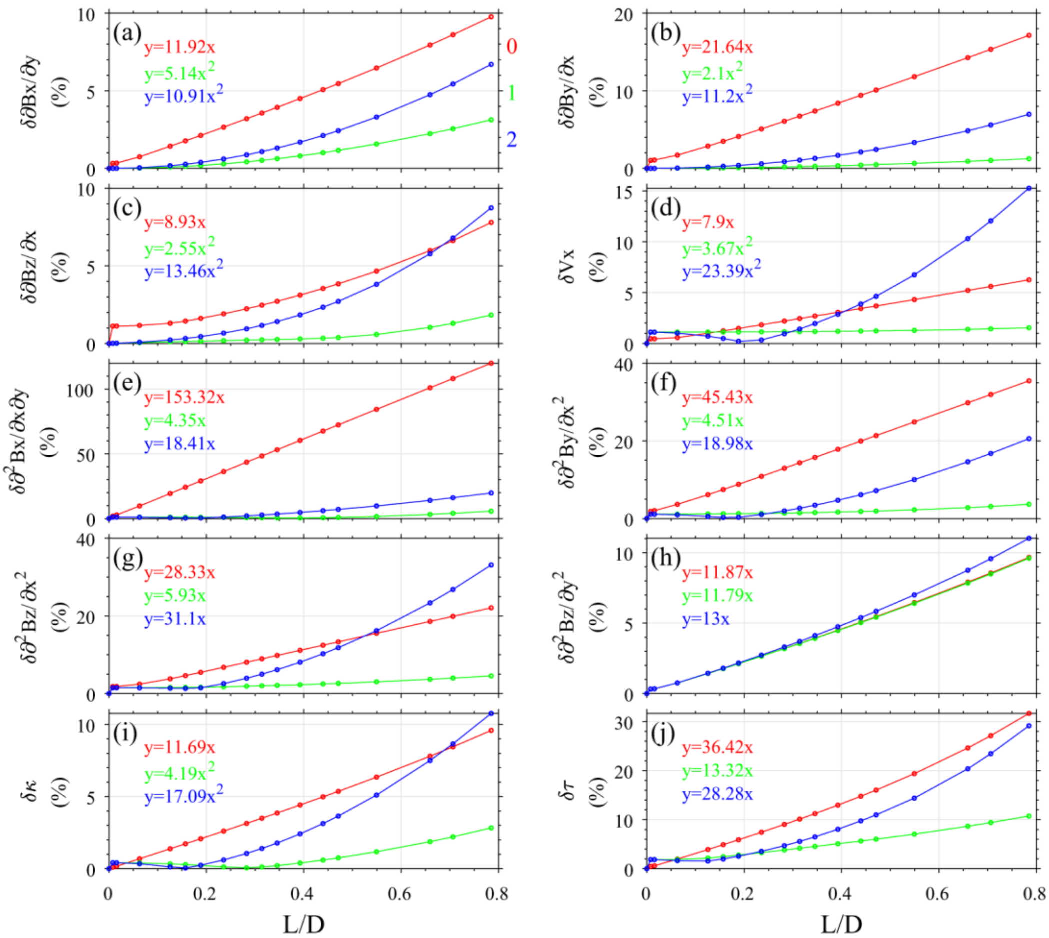

Figure 7: The relative errors (y) of the various calculated parameters of the flux rope for different L/D (x). The red solid lines in each panel are the calculation results with no iteration, while the green, blue lines represent the calculation results with the first

and second iterations, respectively. The format of this figure is the same as that of Figure 5.

5. Application: Magnetic Flux Rope

In this section, we have applied the approach developed in Sections 2 and 3 to investigate the magnetic structure and geometry of a magnetic flux rope at magnetopause, observed by MMS during 2015-10-16 13:04:33-13:04:35, which is the second of two sequential flux ropes reported by Eastwood et al., (2016), and has been analyzed by many researchers (e.g., Zhang et al., 2020). Here, we have used the high-resolution magnetic field data measured by the fluxgate magnetometer, operating at 128 vectors per second in burst-mode (Russell et al. 2014; Burch et al. 2015), and the plasma data provided by FPI (Fast Plasma Investigation, measuring electrons at cadence of 30ms and ions at cadence of 150 ms) (Torbert, et al. 2015; Pollock et al. 2016). To calculate the quadratic magnetic gradient, the plasma moments are interpolated to obtain a 1/128 s time resolution to match that of the magnetic field data and to derive the current density. Note that the MMS constellation is often nearly a regular tetrahedron with its separation scale of $L \approx 20$ km during this time interval.

Typically, there are many waves affecting the magnetic field at various frequencies in space plasmas. If we calculated the time variation rates of the magnetic field and the linear and quadratic magnetic gradients directly, the errors caused by these waves would be so large that we would miss the underlying global features of the magnetic structure. To get rid of the influence of the waves, the magnetic field (Figure 8a) and current density (Figure 8b-8d) data have been filtered by a low-pass filter to eliminate disturbances with frequencies higher than 1Hz from the data. In order to apply the method in Appendix A to calculate the temporal and spatial gradients of the magnetic field and current density, we have adopted n=10 time points on each spacecraft to form a set of data. Thus, there are in total N=4n=40 points in a group of data. With this approach, the calculated temporal and spatial gradients of the magnetic field and current density have rather high accuracy.

We have derived the magnetic rotation features of the flux rope by using the MRA method illustrated in Appendix B (Shen et al., 2007). Figure 8e shows the time series of the magnetic minimum rotation direction $\hat{\mathbf{X}}_3$, which is approximately stable and nearly parallel to GSE +Y direction. Assuming the flux rope is cylindrically symmetric, $\hat{\mathbf{X}}_3$ could be approximately regarded as the orientation $\hat{\mathbf{n}}$ of the flux rope axis, i.e., $\hat{\mathbf{n}} = \hat{\mathbf{X}}_3$. The helical angle of the MFLs can be defined as $\beta = asin(\hat{\mathbf{b}} \cdot \hat{\mathbf{n}})$. As shown in Figure 8f, the helical angle β reaches its maximum value (~89°) at the time ~34.1s, implying that the MFLs lie basically along the axis orientation in the central part of the flux rope. The apparent velocity of the flux rope can be calculated by formula (17), and is illustrated in Figure 8g. One can find that, the apparent velocity at the leading edge of flux rope is larger than that at the trailing edge, suggesting that the flux rope is decelerating and not stable during this interval. Assuming that the flux rope is steady and has a force-free magnetic field, Eastwood et al., (2016) have derived the parameters of this flux rope, and estimate that the velocity is [-206.976, -19.8, -162.88] km/s in GSE, as derived by timing analysis, the axis orientation is [-0.012, 0.989, -0.149] in GSE and the radius is ~550km. From our analysis, it is shown that the mean velocity is ~ [-141.408, -47.58, -96] km/s and the axis orientation is [-0.0889, 0.9367, -0.3386] in GSE during the interval (13:04:33.5-13:04:35), when the flux rope is nearly steady. Considering the complicated motion and structure of flux rope and the different data processing approaches applied, the small discrepancy among the results is not surprising.

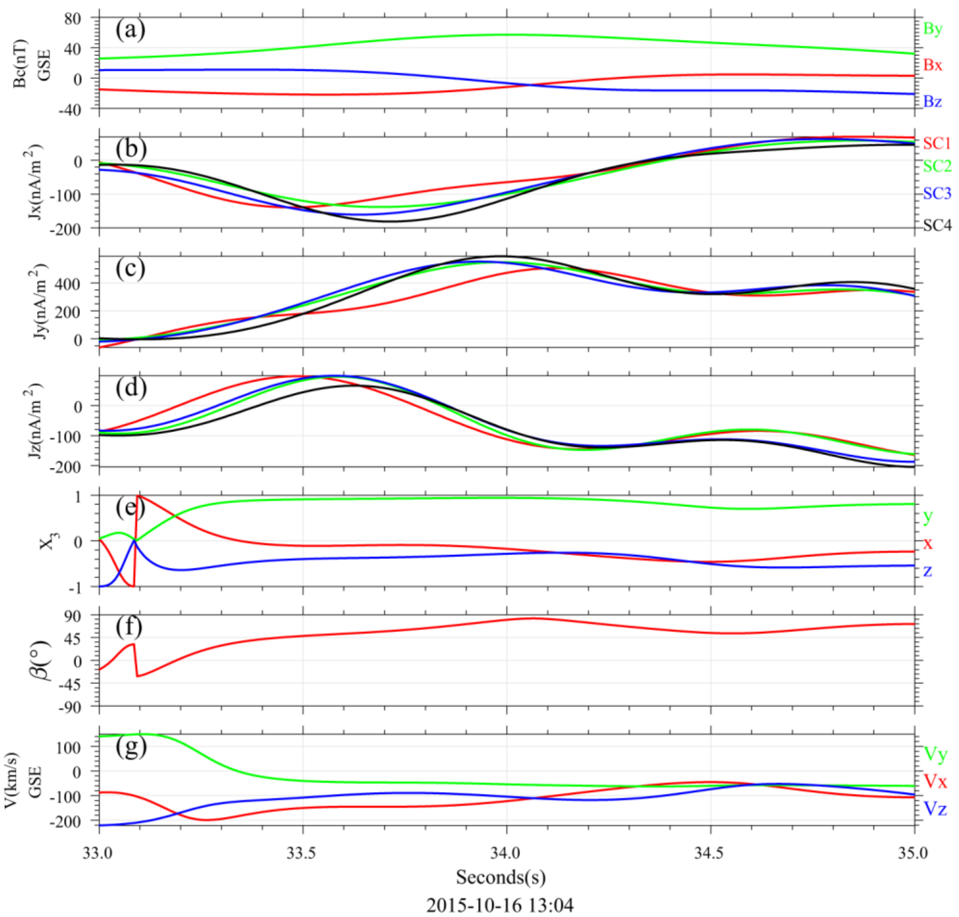

Figure 8: The parameters of the flux rope observed by MMS3 on 16 Oct. 2015. Panel (a) shows the magnetic field at the barycenter of tetrahedron; Panel (b), (c) and (d) display the components of the current density at the four S/C derived by plasma data;

Panel (e) denotes the minimum rotation direction of the MFLs, which is approximately the axis direction of the flux rope; Panel (f) represents the variation of the helical angle; Panel (g) shows the apparent velocity of the flux rope relative to the MMS constellation.

By using the estimators in Sections 2 and 3, the magnetic gradients and geometry of the flux rope can be obtained and these are demonstrated in Figure 9. The total 27 components of the quadratic gradient of magnetic field have been obtained with the estimators in Section 2, which are illustrated in panels (a)-(i) of Figure 9. It can be found that the order of the quadratic gradient of the magnetic field is generally less than 10^{-2} nT/km^2, while that of the first-order magnetic gradient is ~10^{-1} nT/km. The complete geometry of the MFLs in the flux rope can be derived by the estimators in Section 3, which is illustrated in Figure 9j-l. It can be seen that the curvature of MFLs reaches its minimum value of ~$0.80*10^{-3}$/km (Figure 9j) and the torsion reaches its maximum value of ~0.012/km^2 (Figure 9l) at ~34.1sec, when the helical angle is the largest (Figure 8f). These features indicate that this flux rope is a typical one and is consistent with the 2-D flux rope model in Appendix E. The maximum curvature of the MFLs is about ~$3.0*10^{-3}$/km, while accordingly the minimum radius of the curvature of the MFLs is~330km. We can choose this as the characteristic scale of the flux rope, i.e., D=330km. Furthermore, assuming the flux rope has a cylindrical helical structure, the torsion of MFLs can also be obtained directly from the curvature and helical angle from formula E9 in Appendix E. From Figure 9l, it can be seen that the results obtained by both techniques show good agreement with each other. Obviously, the magnetic field lines in this flux rope are right-hand spirals generally. These results verify the effectiveness and applicability of the estimators given in Sections 2 and 3. Since $L/D \approx 20/330 \approx 0.06$, we do not need to perform the iteration in this case because the accuracy of the linear results with no iteration is already very high.

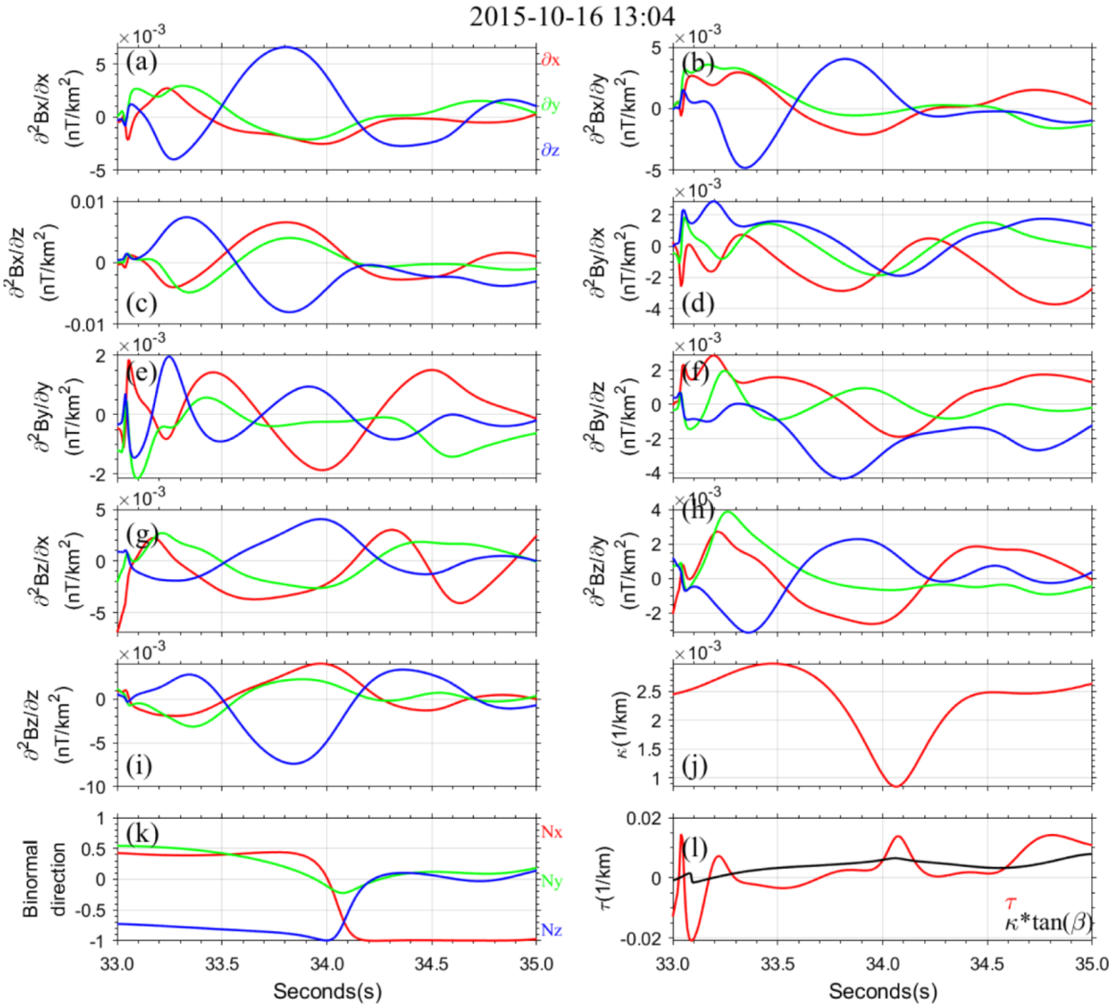

Figure 9: The magnetic structure of the flux rope on 16 Oct. 2015. Panel (a)-(i) show all the 27 components of the quadratic gradient of magnetic field, where the red, green and blue lines represent the partial derivative $\partial x, \partial y, \partial z$, respectively; Panel (j) gives

the time series of the curvature of the MFLs; Panel (k) represents the binormal direction of the MFLs; Panel (l) shows the torsion of the MFLs, with its value calculated by the magnetic gradients represented by the red line, and that drawn from the cylindrical symmetry approximation denoted by the black line.

6. Summary and Discussions

The quadratic magnetic gradient is a key parameter of the magnetic field, with which the fine structure of a magnetic structure can be revealed; as well as the twisting property of the magnetic field. However, up to now, the quadratic magnetic gradient from multi-S/C constellation measurements has not been explicitly calculated. Chanteur (1998) showed that in order to get the quadratic magnetic gradient from multi-point magnetic observations, in general, the number of S/C in the constellation has to be equal to or larger than 10, which is difficult to realize in present space exploration. Fortunately, the MMS constellation can not only provide rather accurate 4-point magnetic field, but can also produce very good 4-point current density estimates from particle measurements, such as to allow the quadratic magnetic gradient problem to be solved in the manner discussed here.

This paper provides a method to obtain the linear and quadratic magnetic gradients as well as the apparent velocity of the magnetic structure based on the 4 point magnetic field and current density observations and give their explicit estimators. Furthermore, the complete geometry of the magnetic field lines is revealed on the bases of these linear and quadratic magnetic gradients, and the estimator for the torsion of the MFLs is given. Simple, but relevant, tests on this novel algorithm have been made for a Harris current sheet and a force-free flux rope model, and the effectiveness and accuracy of these estimators have been verified.

In this approach, the physical quantities to be determined are as follows: the magnetic field $\mathbf{B}_c$ (3 parameters); the linear magnetic gradient $\left(\nabla\mathbf{B}\right)_c$ (9 parameters); quadratic magnetic gradient $\left(\nabla\nabla\mathbf{B}\right)_c$ (6×3=18 parameters), and the apparent velocity of the magnetic structure $\mathbf{V}$ (3 parameters); resulting in a total of 3+9+18+3=33 undetermined parameters.

On the other hand, the input conditions for this algorithm are: the time series of magnetic field $\mathbf{B}_\alpha\left(t\right)$ at 4 points (3×4=12 parameters); the transformation relationships $\frac{\partial\mathbf{B}}{\partial t}=-\mathbf{V}\cdot\nabla\mathbf{B}$ (3 independent constraint equations) and $\frac{\partial}{\partial t}\nabla\mathbf{B}=-\mathbf{V}\cdot\nabla\nabla\mathbf{B}$ (3×3=9 independent constraint equations); the formula $\nabla\left(\nabla\times\mathbf{B}\right)=\nabla\mathbf{j}$, derived from Ampere’s law (2×3-1=5 independent constraints); the equation $\nabla\left(\nabla\cdot\mathbf{B}\right)=0$, from the solenoidal condition of the magnetic field (3-1=2 independent constraints), and finally the constraint equations $\frac{\partial}{\partial X_3}\frac{\partial}{\partial X_3}b_p=0$, as deduced from MRA (2 independent constraints); resulting in a total of 12+3+9+5+2+2=33 independent parameters or constraints.

We note that the contribution of the current density measurements in this approach is the first order gradient of the current density, which is related to the quadratic magnetic gradient by Ampere’s law. Considering the conservation of the current density $\nabla \cdot \mathbf{j} = 0$ and $\partial_3 \nabla \mathbf{B}$ already obtained from the constraint equation $\frac{\partial}{\partial \mathrm{t}} \nabla \mathbf{B} = -\mathbf{V} \cdot \nabla\nabla\mathbf{B}$, the constraint equation $\nabla(\nabla \times \mathbf{B}) = \nabla \mathbf{j}$ yields only $2 \times 3\text{-}1 = 5$ independent constraints（$\partial_3 (\nabla \times \mathbf{B}) = \partial_3 \mathbf{j}$ is not independent）. Similarly, $\nabla(\nabla \cdot \mathbf{B}) = 0$ provides only 3-1=2 independent constraints. Therefore, the linear and quadratic magnetic gradients, and the apparent velocity of the magnetic structure, can be completely determined based on the 4-point magnetic field and current density measured by the MMS constellation.

The calculations have been expressed as being carried out in the S/C constellation frame. The algorithm proceeds as follows. Firstly, under the linear approximation, the temporal and spatial gradients of the magnetic field ($\nabla \mathbf{B}, \frac{\partial \mathbf{B}}{\partial t}$) and of the current density ($\nabla \mathbf{J}, \frac{\partial \mathbf{J}}{\partial t}$) at the barycenter of the S/C constellation can be obtained by the least-squares gradient calculations as demonstrated in Appendix A. The time rate of change of the linear magnetic gradient, $\frac{\partial}{\partial \mathrm{t}} (\nabla \mathbf{B})_{\mathrm{c}}$, and the second order time derivative of the magnetic field can also be obtained. The apparent velocity of the magnetic structure relative to the S/C frame system can then be readily obtained with the formula $\frac{\partial \mathbf{B}}{\partial \mathrm{t}} = -\mathbf{V} \cdot \nabla \mathbf{B}$, and also the gradient of the linear magnetic gradient along the direction of motion, $(\nabla_3 \nabla \mathbf{B})_{\mathrm{c}}$. With the constraint equation $\nabla(\nabla \times \mathbf{B}) = \nabla \mathbf{j}$, the transverse quadratic magnetic gradient of the longitudinal magnetic field B_3, $\nabla_{\mathrm{p}} \nabla_{\mathrm{q}} \mathrm{B}_3 (\mathrm{p}, \mathrm{q} = 1, 2)$, can be found. Finally, the transverse quadratic magnetic gradients of the transverse magnetic field, $\partial_{\mathrm{p}} \partial_{\mathrm{q}} \mathrm{B}_{\mathrm{s}} (\mathrm{t}, \mathbf{r}_{\mathrm{c}})$, can be obtained by using the constraint equations $\nabla(\nabla \cdot \mathbf{B}) = 0$, $\nabla(\nabla \times \mathbf{B}) = \nabla \mathbf{j}$, and magnetic rotation feature

$\frac{\partial}{\partial X_3}\frac{\partial}{\partial X_3}b_p = 0$. Therefore, all the 18 independent components of the quadratic magnetic gradient can be calculated.

The quadratic magnetic gradient, obtained with no iteration, has a truncation error of the first order in L/D because the linear approximation has been made. To find a more accurate quadratic magnetic gradient, an iterative procedure can be performed. In this procedure, the magnetic field, the linear magnetic gradient, and the time derivative of the linear magnetic gradient are corrected by using the quadratic magnetic gradient calculated initially and the above steps are then repeated so as to achieve the components of the corrected quadratic magnetic gradient. After this first iteration, the magnetic field, linear magnetic gradient, the apparent velocity of the magnetic structure at the barycenter of the S/C tetrahedron all have their accuracies improved significantly and have truncation errors in the second order of L/D, while the accuracy of the quadratic magnetic gradient obtained is also enhanced.

This algorithm is valid for both steady and unsteady structures, whether the magnetic structures are moving at a constant velocities or accelerating /decelerating. It is noted that the magnetic field, linear and quadratic magnetic gradients are identical for different inertial frames of reference.

With the magnetic field, linear and quadratic magnetic gradients found, the complete geometry of the MFLs can be determined, including the natural coordinates or Frenet coordinates (tangential unit vector, principal normal and binormal), curvature and torsion. The corresponding estimators for the geometrical features have been given.

The algorithm for estimating the quadratic magnetic gradient and the geometry of the MFLs have been tested with the Harris current sheet and cylindrical flux rope, and its correctness has been verified. It is found that, the errors of the linear quadratic magnetic gradients, apparent velocity of the magnetic structure, and the geometrical parameters are of first order in L/D when no iteration is made. If one iteration is performed, the accuracies of the linear magnetic gradient, apparent velocity of the magnetic structure, curvature of the MFLs are improved significantly and their errors appear at the second order in L/D, while the accuracies of the quadratic magnetic gradient and the torsion of the MFLs are also enhanced. To determine the first order magnetic gradient and apparent relative velocity of the magnetic structure, this algorithm is more accurate than the previous approaches based on the linearity approximation (Harvey, 1998; Chanteur, 1998; Shi et al., 2006).

We have also applied the algorithm developed in this research to investigate the magnetic structure of one flux rope measured by MMS (Eastwood et al., 2016), showing good results. The applicability of this approach is therefore verified.

If the magnetic gradients with orders higher than two are neglected the magnetic field can be expressed as

$$\mathbf{B}(\mathrm{t},\mathbf{r})=\mathbf{B}(\mathrm{t},\mathbf{r}_c)+(\mathbf{r}\text{-}\mathbf{r}_c)\cdot\nabla\mathbf{B}(\mathrm{t},\mathbf{r}_c)+\frac{1}{2}(\mathbf{r}\text{-}\mathbf{r}_c)\,(\mathbf{r}\text{-}\mathbf{r}_c)\cdot\nabla\nabla\mathbf{B}(\mathrm{t},\mathbf{r}_c)\,. \qquad (65)$$

With the MMS magnetic field and current density measurements, the linear and quadratic magnetic gradients at the barycenter are obtained, such that the local spatial distribution of the magnetic field, as well as the MFLs, can be obtained.

Acknowledgments. This work was supported by National Natural Science Foundation (NSFC) of China Grant (No. 41874190, 41922031 and 41774188). M. W. Dunlop is partly supported by Science & Technology Facilities Council (STFC) research grant ST/M001083/1, the NSFC grants 41574155 and 41431071, and the Natural Environment Research Council (NERC) grant NE/P016863/1. The authors are also thankful to the entire MMS team for providing the MMS data (https://cdaweb.gsfc.nasa.gov).

Appendix A: The explicit estimators for the linear gradients of field in space and time

De Keyser, et al.（2007）has put forward an algorithm for calculating the gradients in space and time of a field, which they called Least-Squares Gradient Calculation (LSGC). Here we will find the explicit estimator of the 4 dimensional linear gradients of a scalar field or one component of the vector field.

Considering the 4 S/C of the constellation obtained time series of measurements on a certain physical quantity investigated, as illustrated in Figure 1 in Section 2. Here the S/C constellation reference frame is used. Assuming each S/C makes observations at n times, in total N=4n measurements are made by the constellation, which form a set of data. (It is supposed that, in this area of space time, the physical quantity concerned is approximately varying linearly, and the linear gradients of field in space and time are about homogeneous [De Keyser, et al., 2007].) In the S/C constellation coordinate system, the position of the observation point is $x_{(a)}^{\mu} = \left(x_a, y_a, z_a; t_a\right)\left(\mu = 1,2,3,4\right)$. It is convenient to use the dimensionless length and time in the investigation. If the characteristic size of the S/C constellation is L and the time resolution of the observations is T, we can make the transformation: $x_a / L \to x_a$, $t_a / T \to t_a$. Obviously, in the S/C constellation reference frame, the four

S/C are nearly motionless and their space coordinates $x^{i}_{(a)} = \left(x_a, y_a, z_a\right)$ do not change with time during typical structure crossing events.

In the S/C constellation reference frame, at the space time $x^{\mu}_{(a)} = \left(x_a, y_a, z_a; t_a\right)\left(\mu = 1,2,3,4\right)$, the physical quantity measured is $f\left(x^{\mu}_{a}\right) = f_{(a)}$, its gradients are $\frac{\partial f}{\partial x^{\mu}} = \nabla_{\mu} f \equiv \left(\frac{\partial f}{\partial x}, \frac{\partial f}{\partial y}, \frac{\partial f}{\partial z}, \frac{\partial f}{\partial t}\right)$. The spacetime coordinates at the central point satisfy

$$\sum_{\mathrm{a}=1}^{\mathrm{N}} \Delta x^{\mu}_{(\mathrm{a})} = \sum_{\mathrm{a}=1}^{\mathrm{N}} \left(x^{\mu}_{(\mathrm{a})} - x^{\mu}_{\mathrm{c}}\right) = 0 . \tag{A1}$$

Thus the spacetime coordinates at the central point are

$$x^{\mu}_{\mathrm{c}} = \frac{1}{\mathrm{N}} \sum_{\mathrm{a}=1}^{\mathrm{N}} x^{\mu}_{(\mathrm{a})} . \tag{A2}$$

Here $x^{\mathrm{i}}_{\mathrm{c}}$ are the space coordinates of the barycenter of the S/C constellation, which have fixed values and can be chosen as $x^{\mathrm{i}}_{\mathrm{c}} = 0$. $x^{4}_{\mathrm{c}} = \mathrm{t}_{\mathrm{c}}$ is the average time of the 4n observations.

The physical quantity $f_{(a)}$ measured at the point $x^{\mu}_{(a)}$ can be expanded around the central point x^{μ}_{c} as (Taylor expansion)

$$f_{(a)} = f_c + \Delta x^{\nu}_{a} \nabla_{\nu} f_c + \frac{1}{2} \Delta x^{\nu}_{a} \Delta x^{\lambda}_{a} \nabla_{\nu} \nabla_{\lambda} f_c \tag{A3}$$

Or

$$f_{(a)} = f_{\mathrm{c}} + \Delta x^{\nu}_{a} \mathrm{G}_{\nu} + \frac{1}{2} \Delta x^{\nu}_{a} \Delta x^{\lambda}_{a} \mathrm{G}_{\nu\lambda} \tag{A3'}$$

Here, the first order gradient $\mathrm{G}_{\nu} = (\nabla_{\nu} f)_c$, and the quadratic gradient $\mathrm{G}_{\nu\lambda} = (\nabla_{\nu} \nabla_{\lambda} f)_c$. there are 5 parameters（$f_{\mathrm{c}}, \mathrm{G}_{\nu} = (\nabla_{\nu} f)_c$）to be determined.

Construct the action

$$S = \frac{1}{\mathrm{N}}\sum_{a}\left[f_{\mathrm{c}} + \Delta x_{(a)}^{\nu}\mathrm{G}_{\nu} + \frac{1}{2}\Delta x_{(a)}^{\nu}\Delta x_{(a)}^{\lambda}\mathrm{G}_{\nu\lambda} - f_{(a)} \right]^2 \tag{A4}$$

To minimize it, let

$$\delta S = 0 \tag{A5}$$

Such as to obtain f_c and $\mathrm{G}_{\nu} = \nabla_{\nu} f_c$ at the central point. The above equation leads to

$$\frac{\partial S}{\partial f_c} = 0,\ \frac{\partial S}{\partial G_{\nu}} = 0,\ \frac{\partial S}{\partial G_{\nu\lambda}} = 0\,. \tag{A6}$$

Since

$$\begin{aligned} \frac{\partial S}{\partial f_{\mathrm{c}}} &= \frac{1}{\mathrm{N}}\sum_{a=1}^{\mathrm{N}} 2\left[f_c + \Delta x_{(a)}^{\nu}\mathrm{G}_{\nu} + \frac{1}{2}\Delta x_{(a)}^{\nu}\Delta x_{(a)}^{\lambda}\mathrm{G}_{\nu\lambda} - f_{(i)} \right] \\ &= 2\cdot\frac{1}{\mathrm{N}}\sum_{a=1}^{\mathrm{N}}\left[f_c - f_{(a)} \right] + 2\cdot\frac{1}{\mathrm{N}}\sum_{a=1}^{\mathrm{N}}\Delta x_{(a)}^{\nu}\mathrm{G}_{\nu} + \frac{1}{\mathrm{N}}\sum_{a=1}^{\mathrm{N}}\Delta x_{(a)}^{\nu}\Delta x_{(a)}^{\lambda}\mathrm{G}_{\nu\lambda} = 0 \end{aligned} \quad . \tag{A7}$$

Considering Equation (A1), it reduces to

$$f_{\mathrm{c}} = \frac{1}{\mathrm{N}}\sum_{a} f_{(a)} - \frac{1}{2N}\sum_{a}^{\mathrm{N}}\Delta \mathrm{x}_{(a)}^{\nu}\Delta \mathrm{x}_{(a)}^{\lambda}G_{\nu\lambda}\,. \tag{A8}$$

or

$$f_c = \frac{1}{\mathrm{N}}\sum_{a} f_{(a)} - \frac{1}{2}\mathrm{R}^{\nu\lambda}G_{\nu\lambda}\,. \tag{A8'}$$

Where the general volume tensor $\mathrm{R}^{\mu\nu}$ is defined as

$$\mathrm{R}^{\mu\nu} \equiv \frac{1}{\mathrm{N}}\sum_{a=1}^{\mathrm{N}}\Delta x_{(a)}^{\mu}\Delta x_{(a)}^{\nu} = \frac{1}{\mathrm{N}}\sum_{a=1}^{\mathrm{N}}\left(x_{(a)}^{\mu} - x_{\mathrm{c}}^{\mu}\right)\left(x_{(a)}^{\nu} - x_{\mathrm{c}}^{\nu}\right). \tag{A9}$$

Furthermore,

$$\begin{aligned} 0 = \frac{\delta \mathrm{S}}{\delta \mathrm{G}_{\mu}} &= \frac{1}{\mathrm{N}}\sum_{a=1}^{\mathrm{N}} 2\left[f_{\mathrm{c}} - f_{(a)} + \Delta x_{(a)}^{\nu}\mathrm{G}_{\nu} + \frac{1}{2}\Delta x_{(a)}^{\nu}\Delta x_{(a)}^{\lambda}\mathrm{G}_{\nu\lambda} \right]\nabla x_{(a)}^{\mu} \\ &= -2\cdot\frac{1}{\mathrm{N}}\sum_{a=1}^{\mathrm{N}} f_{(a)}\Delta x_{(a)}^{\mu} + 2\mathrm{R}^{\mu\nu}\mathrm{G}_{\nu} + \mathrm{R}^{\mu\nu\lambda}\mathrm{G}_{\nu\lambda} \end{aligned} \quad , \tag{A10}$$

where the 3 order tensor $\mathrm{R}^{\mu\nu\lambda}$ is defined as

$$\mathrm{R}^{\mu\nu\lambda} \equiv \frac{1}{\mathrm{N}}\sum_{a=1}^{\mathrm{N}} \Delta x_{(a)}^{\mu} \Delta x_{(a)}^{\nu} \Delta x_{(a)}^{\lambda} . \qquad \text{(A11)}$$

From Equation (A10) we get

$$\mathrm{R}^{\mu\nu} G_{\nu} = \frac{1}{\mathrm{N}}\sum_{a}^{\mathrm{N}} \left(x_{(a)}^{\mu} - x_{c}^{\mu} \right) f_a - \frac{1}{2} \mathrm{R}^{\mu\nu\lambda} G_{\nu\lambda} . \qquad \text{(A12)}$$

Thus the linear gradients at the central point are

$$\mathrm{G}_{\nu} = (\nabla_{\nu} f)_c = \left(\mathrm{R}^{-1}\right)_{\nu\mu} \cdot \frac{1}{\mathrm{N}}\sum_{a}^{\mathrm{N}} \left(x_{(a)}^{\mu} - x_{\mathrm{c}}^{\mu} \right) f_a - \frac{1}{2} \left(\mathrm{R}^{-1}\right)_{\nu\mu} \mathrm{R}^{\mu\sigma\lambda} \mathrm{G}_{\sigma\lambda} . \qquad \text{(A13)}$$

Here R^{-1} satisfies $\left(\mathrm{R}^{-1}\right)_{\nu\sigma} \mathrm{R}^{\sigma\lambda} = \mathrm{R}^{\lambda\sigma} \left(\mathrm{R}^{-1}\right)_{\sigma\nu} = \delta_{\nu}^{\lambda}$. These are the first order gradients of the physical quantity in space and time at the central point.

Under the linear approximation, the quadratic gradient is neglected, i.e., $\mathrm{G}_{\nu\lambda} = 0$.

From the formula (A8'), the physical quantity at the central point is

$$f_0 = \frac{1}{\mathrm{N}} \sum_{a} f_{(a)} . \qquad \text{(A14)}$$

From the formula (A13), the first order gradients of the physical quantity in space and time are

$$\mathrm{G}_{\nu} = (\nabla_{\nu} f)_c = \left(\mathrm{R}^{-1}\right)_{\nu\mu} \cdot \frac{1}{\mathrm{N}}\sum_{a}^{\mathrm{N}} \left(x_{(a)}^{\mu} - x_{c}^{\mu} \right) f_a . \qquad \text{(A15)}$$

Appendix B: Natures of the magnetic rotation tensor

In previous investigations [Shen et al., 2007; Shen et al., 2008a, b], the MRA (magnetic rotation analysis) method has been put forward to study the 3 dimensional rotational properties of the magnetic field. We may construct the magnetic rotational tensor $\mathbf{S}$ based on the gradient of the magnetic unit vector $\hat{\mathbf{b}}$, which is defined as

$S_{ij} \equiv \nabla_i b_l \nabla_j b_l$. Because the tensor $\mathbf{S}$ is symmetrical ($S_{ij} = S_{ji}, i, j = 1, 2, 3$), it has three eigenvectors, $\hat{\mathbf{X}}_1$, $\hat{\mathbf{X}}_2$ and $\hat{\mathbf{X}}_3$, and three corresponding eigenvalues, μ_1, μ_2 and μ_3 with $\mu_1 \geq \mu_2 \geq \mu_3 \geq 0$. Actually, the third eigenvalue μ_3 is zero. Fadanelli, et al. (2019) has presented one verification on this property of the magnetic rotational tensor. To facilitate the understanding, here we can show another verification as the following.

The length of $\hat{\mathbf{b}}$ is 1, and $\hat{\mathbf{b}} \cdot \hat{\mathbf{b}} = 1$, so that

$$\nabla_i (\hat{\mathbf{b}} \cdot \hat{\mathbf{b}}) = (\nabla_i b_j) b_j = 0 . \tag{B1}$$

To ensure the existence of $\hat{\mathbf{b}}$, it is necessary that

$$Det(\nabla_i b_j) = 0 . \tag{B2}$$

Based on its definition, the determinant of the magnetic rotation tensor is

$$Det(S_{ij}) = Det(\nabla_i b_l) \cdot Det(\nabla_j b_l) = 0 . \tag{B3}$$

On the other hand,

$$Det(S_{ij}) = \mu_1 \mu_2 \mu_3 , \quad \mu_1 \geq \mu_2 \geq \mu_3 \geq 0 . \tag{B4}$$

Thus equations (A3) and (A4) reduce to

$$\mu_3 = 0 . \tag{B5}$$

So that the third eigenvalue μ_3 of the magnetic rotation tensor $S_{ij} = \nabla_i b_l \nabla_j b_l$ is null definitely.

Appendix C: Another verification on the formula of torsion of MFLs in terms of magnetic gradients

Based on the definition, the torsion of the MFLs

$$\begin{aligned}
\tau &= \frac{1}{\kappa}\frac{\mathrm{d}\boldsymbol{\kappa}}{\mathrm{ds}}\cdot\hat{\mathbf{N}} \\
&= \frac{1}{\kappa}\frac{\mathrm{d}}{\mathrm{ds}}\left(\frac{\mathrm{d}}{\mathrm{ds}}\frac{\mathbf{B}}{\mathrm{B}}\right)\cdot\hat{\mathbf{N}} \\
&= \frac{1}{\kappa}\frac{\mathrm{d}}{\mathrm{ds}}\left(\frac{1}{\mathrm{B}}\frac{\mathrm{d}\mathbf{B}}{\mathrm{ds}}+\mathbf{B}\frac{\mathrm{d}}{\mathrm{ds}}\frac{1}{\mathrm{B}}\right)\cdot\hat{\mathbf{N}} \\
&= \frac{1}{\kappa}\left(\frac{1}{\mathrm{B}}\frac{\mathrm{d}^2\mathbf{B}}{\mathrm{ds}^2}+2\frac{\mathrm{d}}{\mathrm{ds}}\frac{1}{\mathrm{B}}\cdot\frac{\mathrm{d}\mathbf{B}}{\mathrm{ds}}+\mathbf{B}\frac{\mathrm{d}^2}{\mathrm{ds}^2}\frac{1}{\mathrm{B}}\right)\cdot\hat{\mathbf{N}}.
\end{aligned} \tag{C1}$$

Due to $\mathbf{B}\cdot\hat{\mathbf{N}}=\mathrm{B}\hat{\mathbf{b}}\cdot\hat{\mathbf{N}}=0$, $\frac{\mathrm{d}\mathbf{B}}{\mathrm{ds}}\cdot\hat{\mathbf{N}}=\left(\mathrm{B}\frac{\mathrm{d}\hat{\mathbf{b}}}{\mathrm{ds}}+\frac{\mathrm{dB}}{\mathrm{ds}}\hat{\mathbf{b}}\right)\cdot\hat{\mathbf{N}}=\left(\mathrm{B}\boldsymbol{\kappa}+\frac{\mathrm{dB}}{\mathrm{ds}}\hat{\mathbf{b}}\right)\cdot\hat{\mathbf{N}}=0$, the second and third terms at the left hand of the above formula disappear. Therefore

$$\tau=\frac{1}{\kappa\mathrm{B}}\frac{\mathrm{d}^2\mathbf{B}}{\mathrm{ds}^2}\cdot\hat{\mathbf{N}}. \tag{C2}$$

This gives the relationship between the torsion of the MFLs and the second order derivative of the magnetic field along the MFLs.

Furthermore, the torsion of the MFLs becomes

$$\begin{aligned}
\tau &= \frac{1}{\kappa\mathrm{B}}\hat{\mathbf{N}}\cdot\frac{\mathrm{d}}{\mathrm{ds}}\left(\frac{1}{\mathrm{B}}\mathrm{B_i}\partial_\mathrm{i}\mathbf{B}\right) \\
&= \frac{1}{\kappa\mathrm{B}}\hat{\mathbf{N}}\cdot\left[\left(\frac{\mathrm{d}}{\mathrm{ds}}\frac{1}{\mathrm{B}}\right)\mathrm{B_i}\partial_\mathrm{i}\mathbf{B}+\frac{1}{\mathrm{B}}\left(\frac{\mathrm{d}}{\mathrm{ds}}\mathrm{B_i}\right)\partial_\mathrm{i}\mathbf{B}+\frac{1}{\mathrm{B}}\mathrm{B_i}\frac{\mathrm{d}}{\mathrm{ds}}\partial_\mathrm{i}\mathbf{B}\right].
\end{aligned} \tag{C3}$$

The first term at the left hand of the above formula disappear because

$\hat{\mathbf{N}}\cdot\left(\mathrm{B_i}\partial_\mathrm{i}\mathbf{B}\right)=\mathrm{B}\hat{\mathbf{N}}\cdot\frac{\mathrm{d}}{\mathrm{ds}}\mathbf{B}=-\mathrm{B}\cdot\frac{\mathrm{d}\hat{\mathbf{N}}}{\mathrm{ds}}\cdot\mathbf{B}=-\mathrm{B}\left(-\tau\hat{\mathbf{K}}\right)\cdot\mathbf{B}=0$. So that the torsion is

$$\begin{aligned}
\tau &= \frac{1}{\kappa\mathrm{B}}\hat{\mathbf{N}}\cdot\left[\frac{1}{\mathrm{B}}\left(\frac{\mathrm{d}}{\mathrm{ds}}\mathrm{B_i}\right)\partial_\mathrm{i}\mathbf{B}+\frac{1}{\mathrm{B}}\mathrm{B_i}\frac{\mathrm{d}}{\mathrm{ds}}\partial_\mathrm{i}\mathbf{B}\right] \\
&= \frac{1}{\kappa\mathrm{B}^3}\mathrm{N_m B_n}\partial_\mathrm{n}\mathrm{B_i}\partial_\mathrm{i}\mathrm{B_m}+\frac{1}{\kappa\mathrm{B}^3}\mathrm{N_m B_i B_n}\partial_\mathrm{n}\partial_\mathrm{i}\mathrm{B_m}.
\end{aligned} \tag{C4}$$

Appendix D: Geometry of the MFLs in 1 dimensional current sheets

It is assumed that the magnetic field in the 1 dimensional currents is $\mathbf{B} = B_x\hat{\mathbf{e}}_x + B_y\hat{\mathbf{e}}_y + B_z\hat{\mathbf{e}}_z$. Let the z axis to be along the normal to the 1 dimensional current sheets. The components of the magnetic field in the x and y directions are invariants, i.e., $\partial x = 0,\ \partial y = 0$. Therefore the components of the magnetic field in the Cartesian coordinates are

$$\begin{cases} B_x = B_0\eta(z) \\ B_y = \text{Const.} \\ B_z = \text{Const.} \end{cases} . \qquad \text{(D1)}$$

We may choose that $B_z \geq 0$, $B_0 > 0$, $\partial_z B_x = B_0\eta'(z) > 0$. As for the Harris current sheets [Harris, 1962], $\eta(z) = \tanh(z/h)$, where h is the half width of the current sheets. The total magnetic strength is $B = \left(B_x^2 + B_y^2 + B_z^2\right)^{1/2}$.

The curvature of the MFLs is

$$\begin{aligned} \boldsymbol{\kappa} &= \hat{\mathbf{b}}\cdot\nabla\hat{\mathbf{b}} \\ &= B^{-2}(\mathbf{B}\cdot\nabla)\mathbf{B} - \frac{1}{2}B^{-4}(\mathbf{B}\cdot\nabla)B^2\cdot\mathbf{B} \\ &= B^{-2}B_z\partial_z\mathbf{B} - \frac{1}{2}B^{-4}B_z\partial_z B_x^2\cdot\mathbf{B} \\ &= B^{-2}B_z\partial_z B_x\hat{\mathbf{e}}_x - B^{-4}B_zB_x\partial_z B_x\cdot\mathbf{B} \\ &= B^{-4}B_z\partial_z B_x\cdot\left(B^2\hat{\mathbf{e}}_x - B_x\mathbf{B}\right) \\ &= B^{-4}B_z\partial_z B_x\left[\left(B_y^2 + B_z^2\right)\hat{\mathbf{e}}_x - B_xB_y\hat{\mathbf{e}}_y - B_xB_z\hat{\mathbf{e}}_z\right] \end{aligned}$$

(D2)

The value of the curvature is

$$\kappa = \mathrm{B}^{-4}\mathrm{B}_z\partial_z\mathrm{B}_x \cdot \mathrm{B}\left(\mathrm{B}_y^2+\mathrm{B}_z^2\right)^{1/2} = \mathrm{B}^{-3}\mathrm{B}_z\left(\mathrm{B}_y^2+\mathrm{B}_z^2\right)^{1/2}\partial_z\mathrm{B}_x \quad . \tag{D3}$$

The radius of the curvature is $\mathrm{R_c} = 1/\kappa$.

The principal normal vector is

$$\hat{\mathbf{K}} = \boldsymbol{\kappa}/\kappa = \mathrm{B}^{-1}\left(\mathrm{B}_y^2+\mathrm{B}_z^2\right)^{1/2}\left[\left(\mathrm{B}_y^2+\mathrm{B}_z^2\right)\hat{\mathbf{e}}_x - \mathrm{B}_x\mathrm{B}_y\hat{\mathbf{e}}_y - \mathrm{B}_x\mathrm{B}_z\hat{\mathbf{e}}_z\right] \quad . \tag{D4}$$

The binormal vector is

$$\begin{aligned}
\hat{\mathbf{N}} &= \hat{\mathbf{b}}\times\hat{\mathbf{K}} \\
&= \mathrm{B}^{-1}\mathbf{B}\times\hat{\mathbf{K}} \\
&= \mathrm{B}^{-2}\left(\mathrm{B}_y^2+\mathrm{B}_z^2\right)^{1/2}\left(\mathrm{B}_x\hat{\mathbf{e}}_x+\mathrm{B}_y\hat{\mathbf{e}}_y+\mathrm{B}_z\hat{\mathbf{e}}_z\right)\times\left[\left(\mathrm{B}_y^2+\mathrm{B}_z^2\right)\hat{\mathbf{e}}_x - \mathrm{B}_x\mathrm{B}_y\hat{\mathbf{e}}_y - \mathrm{B}_x\mathrm{B}_z\hat{\mathbf{e}}_z\right] \\
&= \mathrm{B}^{-2}\left(\mathrm{B}_y^2+\mathrm{B}_z^2\right)^{1/2}\left(\hat{\mathbf{e}}_y\mathrm{B}_z\mathrm{B}^2 - \hat{\mathbf{e}}_z\mathrm{B}_y\mathrm{B}^2\right) \\
&= \left(\mathrm{B}_y^2+\mathrm{B}_z^2\right)^{1/2}\left(\mathrm{B}_z\hat{\mathbf{e}}_y - \mathrm{B}_y\hat{\mathbf{e}}_z\right)
\end{aligned}$$

. (D5)

Therefore, the binormal of the MFLs is constant. Then, based on the definition (58), the torsion of MFLs is

$$\tau = -\frac{1}{\kappa}\boldsymbol{\kappa}\cdot\frac{\mathrm{d}\hat{\mathbf{N}}}{\mathrm{ds}} = 0\,. \tag{D6}$$

So that, the MFLs in the current sheets as formulated by (D1) are plane curves. For the asymmetric current sheet, $\eta(z) = \alpha + \tanh(\mathrm{z/h})$, $1 > \alpha > 0$. As for the shock fronts, $\mathrm{B_y} = 0$, and $\eta(\mathrm{z}) = \alpha + \tanh(\mathrm{z/h})$, $\alpha > 1$. For these cases, the MFLs are plane curves with zero torsion.

However, as shown in actual observations, the component $\mathrm{B_y}$ is not constant, which maximises at the center of neutral sheets and is decreasing away from the center of the current sheets [Rong, et al., 2012]. The MFLs in the magnetotail current sheets often have a shape of helix in the neutral sheets (Shen, et al., 2008a).

Appendix E: Geometry of Cylindrical helical MFLs in magnetic flux ropes with axial symmetry

Cylindrical spiral MFLs are common in space plasmas, as seen in FTEs [Russell and Elphic, 1979; Lee et al., 1985; Liu and Hu, 1988; Lockwood and Hapgood, 1998; Wang et al., 2007; Liu et al., 2018] or flux ropes caused by local magnetic reconnection processes [Sibeck, et al., 1984; Slavin et al., 1989; Kivelson et al., 1995; Slavin et al., 2003; Zong et al., 2004; Pu et al., 2005; Zhang et al., 2007], fast tailward escaping plamoids [Slavin et al., 1989; Slavin et al., 1995], etc.

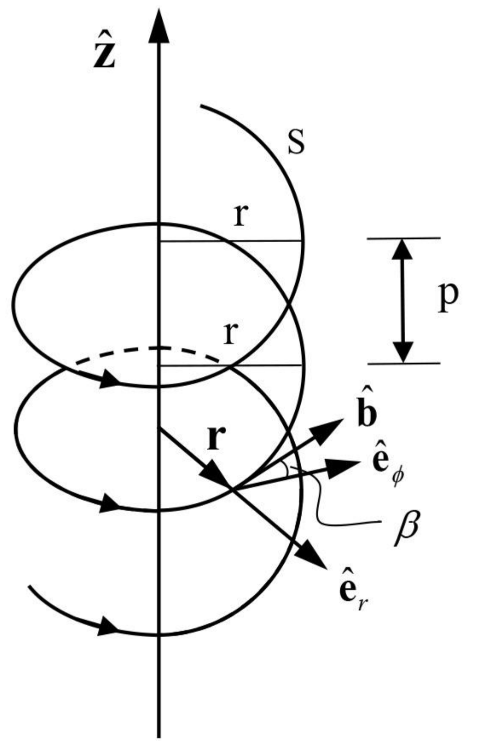

Figure E1 Demonstration on the cylindrical spiral MFLs.

As shown in Figure E1, polar coordinates are used. The central axis is along the z axis, the arc length is s, the distance from the central axis is r, and the azimuthal angle is ϕ.The radial unit vector is $\hat{\mathbf{e}}_{\mathrm{r}}$, and the azimuthal unit vector is $\hat{\mathbf{e}}_{\phi}$. The tangent vector of the MFLs is

$$\hat{\mathbf{b}} = \mathbf{B} / \mathrm{B} = \cos\beta \hat{\mathbf{e}}_{\phi} + \sin\beta \hat{\mathbf{e}}_{\mathrm{z}}, \tag{E1}$$

where β is the helix angle of the MFLs. The helical pitch is $\mathrm{p} = 2\pi \mathrm{r} \tan\beta$. Define the rotation frequency $\omega \equiv \mathrm{d}\phi / \mathrm{ds}$. Then $\omega = \phi / \mathrm{s} = 2\pi / (\mathrm{p} / \sin\beta) = \cos\beta / \mathrm{r}$ .Thus,

$$\frac{\mathrm{ds}}{\mathrm{d}\phi} = \frac{1}{\omega} = \frac{\mathrm{r}}{\cos\beta}. \tag{E2}$$

The curvature of the MFLs is

$$\boldsymbol{\kappa} = \frac{\mathrm{d}\hat{\mathbf{b}}}{\mathrm{ds}} = \frac{\mathrm{d}\phi}{\mathrm{ds}} \frac{\mathrm{d}\hat{\mathbf{b}}}{\mathrm{d}\phi} = \omega \cos\beta \frac{\mathrm{d}\hat{\mathbf{e}}_{\phi}}{\mathrm{d}\phi} = -\omega \cos\beta \hat{\mathbf{e}}_{\mathrm{r}}. \tag{E3}$$

Where, $\frac{\mathrm{d}}{\mathrm{d}\phi} \hat{\mathbf{e}}_{\phi} = -\hat{\mathbf{e}}_{\mathrm{r}}$ is used. So that the curvature is

$$\boldsymbol{\kappa} = -\omega \cos\beta \hat{\mathbf{e}}_{\mathrm{r}}. \tag{E3$'$}$$

The value of the curvature is

$$\kappa = \omega \cos\beta = \mathrm{r}\omega^2 = \mathrm{r}^{-1} \cos^2\beta. \tag{E4}$$

The radius of curvature is

$$\mathrm{R_c} = \mathrm{r}(\cos\beta)^{-2}. \tag{E5}$$

The principal vector of the helical MFLs is $\hat{\mathbf{K}} = \boldsymbol{\kappa} / \kappa = -\hat{\mathbf{e}}_{\mathrm{r}}$, that is along the radial direction. The binormal $\hat{\mathbf{N}}$ is

$$\hat{\mathbf{N}} = \hat{\mathbf{b}} \times \hat{\mathbf{K}} = \left(\cos\beta \hat{\mathbf{e}}_{\phi} + \sin\beta \hat{\mathbf{e}}_{\mathrm{z}}\right) \times \left(-\hat{\mathbf{e}}_{\mathrm{r}}\right) = \cos\beta \cdot \hat{\mathbf{e}}_{\mathrm{z}} - \sin\beta \cdot \hat{\mathbf{e}}_{\phi}. \tag{E6}$$

The variation rate of the binormal $\hat{\mathbf{N}}$ along the MFLs is

$$\frac{\mathrm{d}\hat{\mathbf{N}}}{\mathrm{ds}} = \frac{\mathrm{d}\phi}{\mathrm{ds}} \cdot \frac{\mathrm{d}\hat{\mathbf{N}}}{\mathrm{d}\phi} = \omega\left(-\sin\beta\right)\frac{\mathrm{d}\hat{\mathbf{e}}_{\phi}}{\mathrm{d}\phi} = \omega\sin\beta \cdot \hat{\mathbf{e}}_{\mathrm{r}} . \tag{E7}$$

So that the torsion of the helical MFLs is

$$\tau = -\hat{\mathbf{K}} \cdot \frac{\mathrm{d}\hat{\mathbf{N}}}{\mathrm{ds}} = \hat{\mathbf{e}}_{\mathrm{r}} \cdot \omega\sin\beta\,\hat{\mathbf{e}}_{\mathrm{r}} = \omega\sin\beta = \mathrm{r}^{-1}\sin\beta\cos\beta = 2\pi\mathrm{p}^{-1}\sin^{2}\beta \tag{E8}$$

.

On the contrary, if the curvature κ and torsion τ of the cylindrical spiral MFLs have been measured, the helix angle, the distance from the central axis， the spiral pitch and the rotation frequency can be expressed as

$$\tan\beta = \frac{\tau}{\kappa} = \tau\mathrm{R}_{\mathrm{c}} , \tag{E9}$$

$$\mathrm{r} = \kappa^{-1}\cos^{2}\beta = \frac{\kappa}{\tau^{2}+\kappa^{2}} , \tag{E10}$$

$$\mathrm{p} = 2\pi\mathrm{r}\tan\beta = \frac{2\pi\tau}{\tau^{2}+\kappa^{2}} , \tag{E11}$$

$$\omega = \frac{\cos\beta}{\mathrm{r}} = \sqrt{\tau^{2}+\kappa^{2}} . \tag{E12}$$

Any arbitrary magnetic field line can locally be fitted by a cylindrical spiral arc with the same curvature and torsion. The curvatures of the magnetic field lines are always non-negative. However, the torsion of one MFL can be either positive or negative. When $\tau > 0$, the helix angle $\beta > 0$, the magnetic field line is locally a right-hand cylindrical spiral; while $\tau < 0$, $\beta < 0$, it is a left-hand one.

References

Angelopoulos, V. (2008). The THEMIS mission. Space Science Reviews, 141(1‐4), 5‐34. https://doi.org/10.1007/s11214‐008‐9336‐1.

Balogh, A., et al. (2001), The Cluster magnetic field investigation: overview of inflight performance and initial results, Ann. Geophys., 19, 1207.

Burch, J. L., Moore, T. E., Torbert, R. B., & Giles, B. L. (2016). Magnetospheric Multiscale overview and science objectives. Space Science Reviews, 199(1‐4), 5‐21. https://doi.org/10.1007/s11214‐015‐0164‐9.

Chanteur, G. (1998), Spatial Interpolation for four spacecraft: Theory, in *Analysis Methods for Multi-Spacecraft Data*, edited by G. Paschmann and P. W.Daly, p. 349, ESA Publ. Div., Noordwijk, Netherlands.

De Keyser, J., Dunlop, M. W., Darrouzet, F., and D´ecr´eau, P. M. E.: Least-squares gradient calculation from multi-point observations of scalar and vector fields: Methodology and applications with Cluster in the plasmasphere, Ann. Geophys., 25, 971–987, 2007, http://www.ann-geophys.net/25/971/2007/.

Dunlop, M. W., and T. I. Woodward (1998), Multi-spacecraft discontinuity analysis: Orientation and motion, in *Analysis Methods for Multi-Spacecraft Data*, edited by G. Paschmann and P. W. Daly, p. 271, ESA Publications Division, Noordwijk, The Netherlands.

Dunlop, M. W., D. J. Southwood, K.-H. Glassmeier, and F. M. Neubauer, Analysis of multipoint magnetometer data, Adv. Space Res., 8, 273, 1988.

Dunlop, M. W., Y.-Y. Yang, J-Y. Yang, H. Luhr, C. Shen, N. Olsen, Q. -H. Zhang, Y.V. Bogdanova, J.-B. Cao, P. Ritter, K. Kauristie, A. Masson and R. Haagmans (2015), Multi-spacecraft current estimates at Swarm, *J. Geophys. Res.*, 120, doi:10.1002/2015JA021707.

Dunlop, M W, Haaland, S., Escoubet, P. And X-C Dong (2016), Commentary on accessing 3-D currents in space: Experiences from Cluster, J. Geophys. Res., 121, doi:10.1002/2016JA022668.

Dunlop, M. W., S. Haaland, X-C. Dong, H. Middleton, P. Escoubet, Y-Y. Yang, Q-H Zhang, J-K. Shi and C.T. Russell (2018), Multi-point analysis of current structures and applications: Curlometer technique, in Electric Currents in Geospace and Beyond (eds A. Keiling, O. Marghitu, and M. Wheatland), John Wiley & Sons, Inc, Hoboken, N.J., AGU books, doi: 10.1002/9781119324522.ch4

Dunlop, M. W. J.-Y. Yang, Y-Y. Yang, H. Lühr and J.-B. Cao (2020), Multi-spacecraft current estimates at Swarm, in Multi-satellite data analysis, edited by M W Dunlop and H Luehr, *ISSI scientific reports volume 17, Springer*, DOI:10.1007/978-3-030-26732-2_5.

Eastwood, J. P., T. D. Phan, P. A. Cassak et al. (2016), Ion-scale secondary flux ropes generated by magnetopause reconnection as resolved by MMS, Geophys. Res. Lett., 43, 4716–4724, doi:10.1002/2016GL068747.

Escoubet, C. P., Fehringer, M., & Goldstein, M. (2001), Introduction: The Cluster mission, Annales Geophysicae, 19, 1197-1200, https://doi.org/10.5194/angeo-19-197-2001.

Fadanelli, S., B. Lavraud, F. Califano, et al. (2019). Four‐spacecraft measurements of the shape and dimensionality of magnetic structures in the near‐Earth plasma environment. Journal of Geophysical Research: Space Physics, 124. https://doi.org/10.1029/ 2019JA026747

Friis-Christensen, E., H. Lühr, and G. Hulot (2006), Swarm: A constellation to study the Earth's magnetic field, Earth Planets Space, 58, 351–358.

Hamrin, M. , K. Rönnmark, N. Börlin, J. Vedin, and A. Vaivads (2008), Gals - gradient analysis by least squares, *Annales Geophysicae*, *26*(11), 3491-3499.

Harris, E. G. (1962), On a plasma sheath separating regions of oppositely directed magnetic field, Nuovo Cimento XXIII, 115.

Harvey, C. C. (1998), Spatial gradients and the volumetric tensor, in *Analysis Methods for Multi-Spacecraft Data*, edited by G. Paschmann and P. W. Daly, p. 307, ESA Publications Division, Noordwijk, The Netherlands.

Kivelson, M. G., K. K. Khurana, R. J. W alker, L. Kepko, and D. Xu (1995), Flux ropes, interhemispheric conjugacy, and magnetospheric current closure, J. Geophys. Res., 10(A12), 27,341–27,350, doi:10.1029/96JA02220.

Lavraud, B., Zhang, Y. C., Vernisse, Y., Gershman, D. J., Dorelli, J., Cassak, P. A., et al. (2016). Currents and associated electron scattering and bouncing near the diffusion region at Earth's magnetopause. Geophysical Research Letters, 43, 6036–6043. https://doi.org/10.1002/ 2016GL068359.

Lee, L. C., Z. F. Fu, and S.-I. Akasofu (1985), A simulation study of forced reconnection processes and magnetospheric storms and substorms, J. Geophys. Res., 90(A11), 896–910, doi:10.1029/JA090iA11p10896.

Liu, Y. Y., et al. (2019), SOTE: A nonlinear method for magnetic topology reconstruction in space plasmas, *The Astrophysical Journal Supplement Series* 244.31.

Liu, Z.-X., C. P. Escoubet, Z. Pu, H. Laakso, J. Q. Shi, C. Shen, M. Hapgood, (2005), The Double Star Mission, Ann Geophysicae, 23, 2707-2712, doi: 10.5194/angeo-23-2707-2005.

Liu, Z. X., and Y. D. Hu (1988), Local magnetic reconnection caused by vortices in the flow field, *Geophys. Res. Lett.*, **12**, 752.

Liu, Y., Z. Y. Pu, et al. (2018), Ion-scale structures in flux ropes observed by MMS at the magnetopause (in Chinese), Chin. J. Space Sci., 38(2), 147-168. DOI:10.11728/cjss2018.02.147.

Lockwood, M., and M. A. Hapgood (1998), On the cause of a magnetospheric flux transfer event, J. Geophys. Res., 103(A11), 26,453–26,478, doi:10.1029/98JA02244.

McComas, C., T. Russell, R. C. Elphic, and S. J. Bame, The near-Earth cross-tail current sheet: Detailed ISEE 1 and 2 case studies, J. Geophys. Res., 91, 4287, 1986.

Ogilvie, K. W., T. Von Rosenvinge, and A. C. Durney (1977), International Sun-Earth explorer: A three-spacecraft program, Science, 198, 131–138.

Pu, Z.Y., Q.-G. Zong, T.A. Fritz, C.J. Xiao, Z.Y. Huang, S.Y. Fu, Q.Q. Shi, M.W. Dunlop, K.-H. Glassmeier, A. Balogh, P. Daly, H. Reme, J. Dandouras, J.B. Cao, Z.X. Liu, C. Shen, and J.K. Shi (2005), Multiple flux rope events at the high-latitude magnetopause: cluster/rapid observation on 26 January, 2001, Surv. Geophys. **26**(1–3), 193–214, https://doi.org/10.1007/s10712-005-1878-0

Rong, Z. J., W. X. Wan, C. Shen, X. Li, M. W. Dunlop, A. A. Petrukovich, T. L.

Zhang, and E. Lucek (2011), Statistical survey on the magnetic structure in magnetotail current sheets, J. Geophys. Res., 116, A09218, doi:10.1029/2011JA016489.

Rong, Z. J., W. X. Wan, C. Shen, X. Li, M. W. Dunlop, A. A.Petrukovich, L.-N. Hau, E. Lucek, H. Rème (2012), Profile of strong magnetic field By component in magnetotail current sheets, J. Geophys. Res., 117, A06216, doi:10.1029/2011JA017402.

Russell, C. T., Anderson, B. J., Baumjohann, W., Bromund, K. R., Dearborn, D., Fischer, D., et al. (2016), The MagnetosphericMultiscale magnetometers,*Space Science Reviews, 199*(1-4), 189-256, https://doi.org/10.1007/s11214-014-0057-3.

Russell, C. T., and R. C. Elphic (1979), ISEE observations of flux transfer events at the dayside magnetopause, Geophys. Res. Lett., 6(1), 33–36, doi:10.1029/GL006i001p00033.

Shen, C., X. Li, M. Dunlop, Z. X. Liu, A. Balogh, D. N. Baker, M. Hapgood, and X. Wang (2003), Analyses on the geometrical structure of magnetic field in the current sheet based on cluster measurements, *J. Geophys. Res.*, *108*(A5), 1168, doi:10.1029/2002JA009612.

Shen, C., and Z. -X. Liu (2005), Double Star Project Master Science Operations Plan, Ann. Geophysicae, 23, 2851-2859, doi: 10.5194/angeo-23-2851-2005.Shen, C., X. Li, M. Dunlop, Q. Q. Shi, Z. X. Liu, E. Lucek, and Z. Q. Chen (2007), Magnetic field rotation analysis and the applications, J. Geophys. Res., 112, A06211, doi:10.1029/2005JA011584.

Shen, C., Z. Liu, X. Li, M. W. Dunlop, E. A. Lucek, Z. Rong, Z. Chen, C. P. Escoubet, H. V. Malova, A. T. Y. Lui, A. N. Fazakerley, A. P. Walsh, and C. Mouikis (2008a), Flattened Current Sheet and its Evolution in Substorms, J. Geophys. Res., 113, A07S21,doi:10.1029/2007JA012812.

Shen, C., Z. J. Rong, X. Li, Z. X. Liu, M. Dunlop, E. Lucek, H.V. Malova (2008b), Magnetic Configurations of Tail Tilted Current Sheets, *Ann. Geophys.*, 26, 3525–3543.

Shen, C., et al. (2011), The magnetic configuration of the high-latitude cusp and dayside magnetopause under strongmagnetic shears, *J. Geophys. Res., 116*, A09228, doi:10.1029/2011JA016501.

Shen, C., et al. (2012a), Spatial gradients from irregular, multiple-point spacecraft configurations, J. Geophys. Res., 117, A11207, doi:10.1029/2012JA018075.

Shen, C., Z. J. Rong, and M. Dunlop (2012b), Determining the full magnetic field gradient from two spacecraft measurements under special constraints, J. Geophys. Res., 117, A10217, doi:10.1029/2012JA018063.

Shen, C., et al. (2014), Direct calculation of the ring current distribution and magnetic structure seen by Cluster during geomagnetic storms, J. Geophys. Res. SpacePhysics, 119, doi:10.1002/2013JA019460.

Shi, Q. Q., Shen, C., Dunlop, M. W., Pu, Z. Y., Zong, Q.-G., Liu, Z. X., Lucek, E., and Balogh, A., 2006, Motion of observed structures calculated from multi-point magnetic field measurements: Application to Cluster, Geophys. Res. Lett., 33, L08109, doi:10.1029/2005GL025073.

Sibeck, D. G., G. L. Siscoe, J. A. Slavin, E. J. Smith, S. J. Bame, and F. L. Scarf (1984), Magnetotail flux ropes, Geophys. Res. Lett., 11(10), 1090–1093, doi:10.1029/GL011i010p01090.

Slavin, J. A., et al. (1989), CDAW 8 observations of plasmoid signatures in the geomagnetic tail: An assessment, J. Geophys. Res., 94(A11), 15,153–15,175, doi:10.1029/JA094iA11p15153.

Slavin, J. A., C. J. Owen, and M. M. Kuznetsova (1995), ISEE3 observations of plasmoids with flux rope magnetic topologies, Geophys. Res. Lett., 22(15), 2061–2064, doi:10.1029/95GL01977.

Slavin, J. A., et al. (2003), Cluster electric current density measurements within a magnetic flux rope in the plasma sheet, Geophys. Res. Lett., 30(7), 1362, doi:10.1029/2002GL016411.

Song, P., and C. T. Russell (1999), Time series data analyses in space physics, *Space ence Reviews, 87*(3-4), 387-463.

Torbert, R. B., Vaith, H., Granoff, M., Widholm, M., Gaidos, J. A., Briggs, B. H., et al. (2015). The electron drift instrument for MMS. Space Science Reviews, 199(1‐4), 283‐305. https://doi.org/10.1007/s11214‐015‐0182‐7

Torbert, R. B., Dors, I., Argall, M. R., Genestreti, K. J., Burch, J. L., Farrugia, C. J., et al. (2020). A new method of 3‐D magnetic field reconstruction. Geophysical Research Letters, 47, e2019GL085542. https://doi.org/ 10.1029/2019GL085542.

Vogt, J., G. Paschmann, and G. Chanteur (2008), Reciprocal Vectors, in Multi-Spacecraft Analysis Methods Revisited, ISSI Sci. Rep., SR-008, edited by G. Paschmann and P. W. Daly, pp. 33–46, Kluwer Academic Pub., Dordrecht, Netherlands.

Vogt, J., A. Albert, and O. Marghitu (2009), Analysis of three-spacecraft data using planar reciprocal vectors: Methodological framework and spatial gradient estimation, Ann. Geophys., 27, 3249–3273, doi:10.5194/angeo-27-3249-2009.

Wang J., M. W. Dunlop, Z.Y. Pu, et al. (2007), TC1 and Cluster observation of an FTE on 4 January 2005: A close conjunction, Geophys. Res. Lett., 34, L03106, doi:10.1029/2006GL028241.

Xiao, C., W. Liu, C. Shen, H. Zhang, & Z. Rong (2018). Study on the curvature and gradient of the magnetic field in Earth's cusp region based on the magnetic curvature analysis method. Journal of Geophysical Research: Space Physics, 123, 3794–3805. https://doi.org/10.1029/2017JA025028

Zhang, C., Rong, Z. J., Shen, C., Klinger. L., Gao. J. W., Slavin. J. A., Zhang, Y. C., Cui. J., Wei. Y., (2020). Examining the magnetic geometry of magnetic flux ropes from the view of single-point analysis. *The Astrophysical Journal*., doi: 10.3847/1538-4357/abba16

Zhang, Y. C., Z. X. Liu, C. Shen, A. Fazakerley, M. Dunlop, H. Reme, E. Lucek, A. P. Walsh, and L. Yao (2007). The magnetic structure of an earthward-moving flux rope observed by Cluster in the near-tail, *Ann. Geophys.*, 25, 1471-1476.

Zong, Q. G., et al. (2004), Cluster observations of earthward flowing plasmoid in the tail, Geophys. Res. Lett., 31, L18803, doi:10.1029/ 2004GL020692.